DISSERTATION

submitted to the
Combined Faculties for the Natural Sciences and Mathematics
of the Ruperto-Carola University of Heidelberg, Germany
for the degree of

doctor rerum naturalium

presented by

Matthias Ulrich Mozer, M.S.

born in Hannover, Germany

Oral examination: July 24$^{\text{th}}$ 2006

Measurement and QCD Analysis of Diffractive Jet Cross Sections in Deep-Inelastic Scattering at HERA

Referees: Prof. Dr. Franz Eisele

Prof. Dr. Otto Nachtmann

Abstract

Differential cross sections for the production of two jets in diffractive deep inelastic scattering (DIS) at HERA are presented. The process studied is of the type $ep \to eXY$, where the central hadronic system X contains at least two jets and is separated from the system Y by a gap in rapidity. The forward system Y consists of an elastically scattered proton or a low mass dissociation system.
The data were taken with the H1 detector during the years of 1999 and 2000 and correspond to an integrated luminosity of 51.5 pb^{-1}.
The measured cross sections are compared to fixed order NLO QCD predictions, that use diffractive parton densities which have previously been determined by a NLO QCD analysis of inclusive diffractive DIS at H1. The prediction and the data show significant differences. However, the dijet cross section is dominated by the diffractive gluon density, which can be extracted by the above mentioned analysis only with considerable uncertainty. Hence a combined QCD analysis of the previously published inclusive diffractive data and the dijet data is performed. This combined fit analysis allows the determination of diffractive quark and gluon densities with comparable precision. The common description of inclusive diffractive data and the dijet data confirms QCD factorization.

Kurzfassung

Die Messung differentieller Wirkungsquerschnitte von Zwei-Jet Produktion in diffraktiver tief inelastischer Streuung am HERA Beschleuniger wird präsentiert. Der untersuchte Prozeß ist vom Typ $ep \to eXY$, wobei das zentrale hadronische System X mindestens zwei Jets umfaßt und vom System Y durch eine Lücke in der Rapidität getrennt ist. Das vorwärts liegende System Y besteht aus einem elastisch gestreuten Proton oder einem Dissotiationssystem niedriger Masse.
Die Daten wurden während der Jahre 1999 und 2000 mit dem H1 Detektor aufgenommen und entsprechen einer integrierten Luminosität von 51.5 pb^{-1}.
Die gemessene Wirkungsquerschnitte werden mit NLO QCD Vorhersagen fester Ordnung verglichen. Die Vorhersagen basieren dabei auf diffraktiven Partondichten, die bereits bei H1 durch eine NLO QCD Analyse inklusiver diffraktiver tief inelastischer Streuung bestimmt wurden. Die Vorhersage und die Daten zeigen signifikante Unterschiede. Allerdings wird der Zwei-Jet Wirkungsquerschnitt durch die diffraktive Gluondichte dominiert, die in der oben genannten Analyse nur mit erheblichen Unsicherheiten extrahiert werden konnte. Deshalb wurde eine kombinierte QCD Analyse der bereits publizierten inklusiven diffraktiven Daten und der Zwei-Jet Daten durchgeführt. Die kombinierte Analyse erlaubt die Bestimmung der diffraktiven Quark- und Gluondichte mit vergleichbarer Genauigkeit. Die gleichzeitige Beschreibung inklusiver Diffraktion und der Zwei-Jet Daten bestätigt die QCD-Faktorisierung.

Contents

List of Figures

List of Tables

Chapter 1

Introduction

Interactions of hadronic particles are described to high precision by the theory of quantum chromo dynamics (QCD) which describes all hadrons in term of constituent quarks and gluons and the colour-interaction between them. QCD predicts the phenomena known as confinement and asymptotic freedom [1, 2]. Confinement describes the fact that no free quarks and gluons can be observed at distance scales greater than $\sim$1 fm, above which they are bound in colour neutral hadrons. On scales much smaller than $\sim$1 fm the opposite happens: the strong interaction between quarks and gluons becomes smaller and smaller, so that treating them as free particles becomes viable, thus the term asymptotic freedom. In particular asymptotic freedom allows the application of perturbation theory to QCD provided that the process under study involves a hard scale. Perturbative QCD is the most important way of predicting cross sections for high energy scattering experiments.

However, the hadronic scattering cross section is dominated by elastic scattering with small momentum transfers (often called diffractive scattering). Due to the low scales involved in these processes, perturbative QCD cannot be successfully applied. Historically, phenomenological methods founded in the picture of hadrons as fundamental particles with mesons mediating the interaction have been used successfully [3, 4]. One such approach that has proven particularly successful is called Regge phenomenology after Tullio Regge, who introduced it in the early 1960's. As no colour-charge, spin, or other quantum number is exchanged in the elastic scattering, this process is mediated by an object that carries vacuum quantum numbers, the pomeron. Up to now there has been no conclusive interpretation of the pomeron in terms of the underlying QCD [5, 6].

The HERA accelerator at DESY provides the unique opportunity to study the structure of this pomeron in detail and thus gain a deeper understanding of diffractive scattering. HERA is an electron-proton collider, which opens the possibility to study diffractive physics with the same methods that have proven successful in the study of the proton structure using deep inelastic scattering (DIS). In particular the energy transferred from the electron to the hadronic part of the interaction can serve as a hard scale that makes calculations of perturbative QCD possible.

At HERA copious amounts of events are produced where the proton is scattered elastically, but another hadronic system is produced separated from the proton by a gap devoid of any particles. These diffractive events can be visualized as the proton

emitting a pomeron with vacuum quantum numbers (hence the gap), which interacts with the electron producing the hadronic system in the final state.

Theoretical considerations show that diffractive DIS processes can be factorized into universal diffractive parton densities characteristic for the proton and a hard scattering matrix element [7] analogous to the factorization in ordinary deep inelastic scattering [8, 9]. This approach can be extended to the so called resolved pomeron model [10, 11] which interprets the diffractive parton densities of the proton as the product of a pomeron flux in the proton and parton densities of the pomeron. It is possible to extract the universal diffractive parton densities from measurements of inclusive diffractive DIS, which can be used to predict the cross sections for any final state in diffractive DIS. At the H1 and ZEUS experiments [12–20] diffractive scattering has been analyzed successfully in inclusive diffraction, but also in exclusive final states like dijet- and open charm production. These results generally confirm factorization in diffractive DIS and show that the concept of the pomeron can be transferred to electron proton scattering. A breakdown of factorization has been observed in photoproduction (where the exchanged photon is real and the proof of [7] does not apply), which has been the subject of intense study [13, 21] due to its importance in the understanding of diffraction in hadronic collisions [22].

In this work, the differential cross section of diffractive DIS events containing at least two hard jets (collimated bundles of outgoing particles) is measured similarly to a previous H1 analysis [13] and compared to QCD predictions based on parton densities extracted from inclusive diffraction [12]. This comparison is a powerful test of the underlying assumption that the resolved pomeron model can be applied. This is emphasized by the fact that this study uses $\sim$7 times the number of events of the last similar study of diffractive dijets [13], giving it higher statistical precision and the possibility to extract double differential cross sections.

The agreement between data and prediction turns out to be not satisfactory. However, the prediction of the dijet cross section depends mainly on the gluon density, which was only extracted with considerable systematic uncertainty in the analysis of inclusive diffraction [12]. To alleviate this problem and obtain a more precise gluon density, a combined fit of the parton densities to the dijet data and the data from [12] is performed. The results show that one set of parton densities can consistently describe diffractive dijet production in all studied variables. The combined fit results show simultaneously good agreement with the inclusive diffractive data, confirming the factorization approach mentioned above. Nevertheless small differences between the dijet- and inclusive measurements remain.

Chapter 2

Theory

2.1 Deep Inelastic Scattering

Electron proton scattering can be divided into two main classes: photoproduction and deep inelastic scattering, depending on the squared four-momentum transfer Q^2 between the electron and the proton. The boundary between the two is fluid, but generally a process is called deep inelastic if the squared four-momentum transfer is larger than the proton mass itself, $Q^2 \gtrsim 1$ GeV. A suitable theoretical interpretation of deep inelastic scattering (DIS) can be found in the quark parton model.

2.1.1 The Quark Parton Model

The quark parton model was developed in the late 1960's as an interpretation of ongoing experiments of DIS [8, 9]. It approximates the proton as a collection of independent particles called partons, one of which scatters with the electron while the others continue undisturbed (see Figure 2.1). The partons are assumed not to interact with each other. The measured cross sections of DIS can then be interpreted in terms of momentum distributions of partons in the proton.

Kinematics

Deep inelastic scattering at HERA mainly involves processes of the type $ep \to e'X$, where X can be any hadronic final state. Let k (k') denote the four-momentum of the incoming (outgoing) electron and P the incoming proton momentum. It is useful to describe the scattering in terms of the ep center of mass energy $\sqrt{s}$, the mass of the exchanged virtual photon Q^2 and the Bjørken scaling variable x_{Bj}:

$$s = (k + P)^2 \qquad Q^2 = -q^2 \qquad x_{Bj} = \frac{Q^2}{2P \cdot q}. \tag{2.1}$$

In the quark parton model [8, 9] x_{Bj} is interpreted as the longitudinal momentum fraction that the struck quark takes in the proton. Additionally the inelasticity variable y and the photon-proton center of mass energy W can be introduced as:

$$y = \frac{q \cdot P}{k \cdot P} \approx \frac{Q^2}{x_{Bj} s} \qquad W^2 = (q + P)^2 \approx ys - Q^2, \tag{2.2}$$

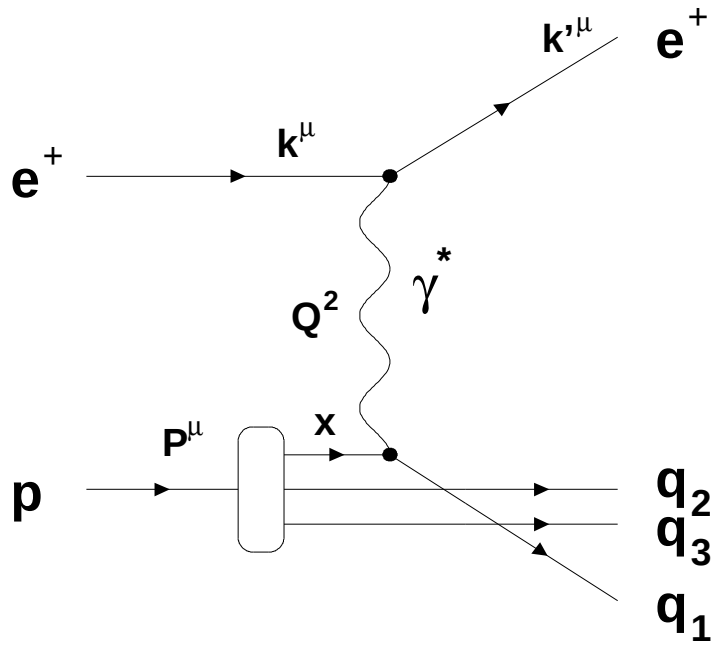

Figure 2.1: Feynman diagram of deep inelastic scattering in the quark parton model.

where particle masses have been neglected in the approximations.

Cross Sections and Parton Densities

In the quark parton model, the cross section for the inclusive DIS process $ep \to e'X$ is the incoherent sum of each individual electron parton reaction $eq \to e'q$ (due to the electromagnetic interaction, only charged partons, i.e. quarks, are considered). Thus, to determine the ep cross section, one needs to calculate the eq cross section depending on the quark momentum and integrate over the probability to find a quark of a given momentum in the proton. The eq cross section is calculated in quantum electrodynamics assuming massless quarks of spin $\frac{1}{2}$ and unpolarized electrons and protons. The resulting cross section is:

$$\frac{\mathrm{d}\sigma(eq \to eq)}{\mathrm{d}Q^2} = \frac{2\pi\alpha_{em}^2 e_q^2}{Q^4}\left(1 + (1-y)^2\right), \tag{2.3}$$

where α_{em} denotes the fine structure constant and e_q the charge of the quark. The quantities Q^2 and y as defined above do not depend on the scattering partner of the electron and their definitions need not be changed for the transition from ep to eq scattering. Introducing the probability to find a quark of momentum fraction x_{Bj} in the proton as $f_q(x_{Bj})$, we obtain the DIS scattering cross section:

$$\frac{\mathrm{d}^2\sigma}{\mathrm{d}x_{Bj}\mathrm{d}Q^2} = \frac{2\pi\alpha_{em}^2}{Q^4 x_{Bj}} Y_+(y) F_2^{QPM}(x_{Bj}), \tag{2.4}$$

$$Y_\pm(y) = 1 \pm (1-y)^2, \tag{2.5}$$

$$F_2^{QPM}(x_{Bj}) = \sum_q e_q^2 x f_q(x_{Bj}). \tag{2.6}$$

The structure function $F_2^{QPM}(x_{Bj})$ is summed over all flavors of quarks. Notably, $F_2^{QPM}(x_{Bj})$ only depends on x_{Bj}, a behavior called Bjørken scaling. In this simplified approach, the possibility of a weak interaction between the electron and the quark (via an exchanged Z^0 boson) has been neglected. Thus deviations from equation 2.4 are expected if $Q^2 \gtrsim m_Z^2$. However such high values of Q^2 are not reached in this study, and corrections due to the weak interaction can be neglected.

Studies of DIS lead to the conclusion that the proton contains three constituent quarks [23, 24]. From this basic form of the quark parton model, little can be learned about the forces that that bind the constituent quarks in the proton. Nevertheless, once interactions among the partons are introduced, it is possible to see its effects in deviations from the idealized predictions. This can be observed most prominently in the so called scaling violations: Contrary to equation 2.4 the DIS cross sections dependence on Q^2 deviates from the simple Q^{-4} behavior where the details of the deviations are governed by the interactions among the partons. Typically the additional Q^2 dependence is absorbed into the parton densities, which then depend on Q^2.

To disentangle the interactions among the partons from the electromagnetic interaction it is necessary to consider the eq cross section to a higher order in α_{em}. In this study, the kinematic effects of these higher order terms are corrected for in the data with the help of a model calculation, so that the remaining kinematic dependences are solely caused by the interactions among the partons.

2.2 Quantum Chromo Dynamics

The partons in the proton and their interactions are generally described in terms of quantum chromo dynamics, which is the underlying field theory of the strong interaction. It is a non-abelian gauge theory based on the SU(3) group. The basic fermions are called quarks, which carry one of three possible charges, called colour-charge. The interaction between the quarks is mediated by gauge-bosons called gluons, which also carry colour-charge. As in other gauge theories, the strength of the interaction (symbolized by the strong coupling constant α_s) depends due to quantum fluctuations on the momentum scales involved in the interaction. Opposite to the effect seen in the electro-weak interaction, α_s rises with decreasing momentum scales, leading to the phenomena of confinement and asymptotic freedom [1, 2]. Asymptotic freedom is especially important for this analysis, as it allows the application of perturbation theory, currently the most advanced method to predict cross sections in high energy scattering experiments.

The rapid acceptance of QCD can be attributed to measurements in deep inelastic scattering. In the quark parton model the quarks do not interact, leading to the prediction of Bjørken scaling: The structure function should only depend on x_{Bj} but not Q^2. Interactions of the quarks lead to a dependence also on Q^2. The details of the dependence are determined by the exact interaction involved (for details see section 2.2.2). QCD has been enormously successful at explaining the data gathered in deep inelastic scattering experiments.

Quantum chromo dynamics modifies the naive quark parton model in two ways. On one hand it causes interactions of the quarks within the proton leading to a dependence of the parton densities on Q^2 in addition to x_{Bj}. On the other hand, the strong interaction

cannot simply be neglected in the calculation of the eq cross section. Figure 2.2 (left) shows the Feynman graph for the simple quark parton model, the two other panels of Figure 2.2 show the two diagrams that correct the cross section to the first order in the strong coupling constant α_s. Inclusion of these (and diagrams of even higher orders) will produce significant corrections to the eq scattering cross section (equation 2.3). Due to the rather complex symmetry structure of QCD, these additional diagrams lead to several complications which will be discussed in the following.

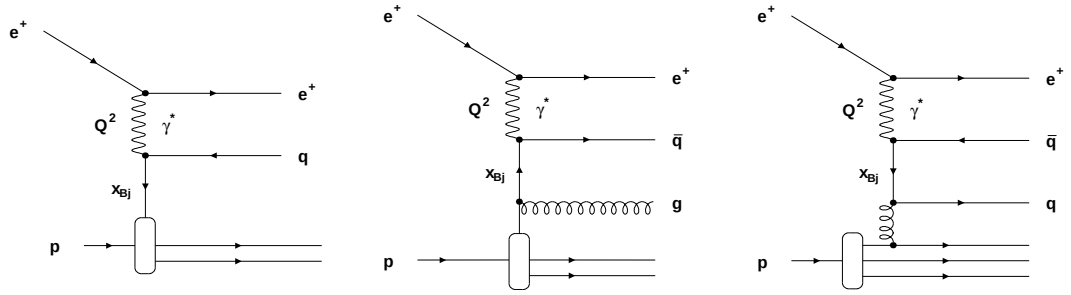

Figure 2.2: Feynman diagrams of deep inelastic scattering in the quark parton model including QCD corrections up to order α_s.

2.2.1 Renormalization

In perturbative QCD the coefficients of the individual terms are integrals over the phase space of real and virtual particles. These will often be divergent. Therefore a regularization scheme is defined to control the divergent parts of the integrals while maintaining the physical significance. There are various possible schemes of regularization, all of which introduce a dimensional constant μ_r, the renormalization scale. Cross sections calculated with this method generally depend on μ_r. This dependence is compensated by defining an effective coupling $\alpha_s(\mu_r)$ in which the divergent contributions are absorbed. The requirement that the physical predictions must not depend on the arbitrarily chosen quantity μ_r leads to the renormalization group equations which determine the functional dependence of α_s on μ_r. This equation has not been solved analytically, however analytically accessible expansions can be made. The solution of the equation up to order $\mathcal{O}(\alpha_s^2)$ is given by [25]:

$$\alpha_s(\mu_r) = \frac{4\pi}{\beta_0 \ln(\mu_r^2/\Lambda^2)} \left[1 - \frac{2\beta_1}{\beta_0^2} \frac{\ln\left[\ln(\mu_r^2/\Lambda^2)\right]}{\ln(\mu_r^2/\Lambda^2)}\right], \tag{2.7}$$

$$\beta_0 = 11 - \frac{2}{3} n_f, \tag{2.8}$$

$$\beta_1 = 51 - \frac{19}{3} n_f, \tag{2.9}$$

where Λ is a free parameter, the QCD-scale, and has to be determined from experiments. The experimental value of α_s is typically cited at the Z^0 mass, the current world average is $\alpha_s(\mu_r = M_Z) = 0.1187 \pm 0.002$ [25].

2.2.2 Factorization and Evolution of Parton Distributions

Just as the strong coupling α_s depends on the renormalization scale μ_r due to the necessary renormalization, a similar scale dependence appears in the parton densities. The scattering matrix elements used to calculate a DIS cross section contain divergences that cannot be regularized by simply absorbing them in α_s alone. These divergences typically derive from partons emitted along the direction of the outgoing proton. This type of divergence can be regularized by so called factorization. In this scheme a momentum factorization scale μ_f is introduced which can be interpreted as the momentum threshold above which partons count toward the actual matrix element, while they are treated as part of the parton densities below this scale. By this treatment the divergences can be absorbed into the parton densities, which then depend on μ_f. However, if the theory is to remain physical, any prediction involving the parton densities (assuming all orders in α_s are included) must not depend on the factorization scale. Thus the parton densities can be further constrained as they must obey a differential equation analogous to the renormalization group equation for α_s. This equation determines the dependence of the parton densities on the factorization scale. To solve this equation it would in principle be necessary to include all terms to all orders in the perturbation series. However, today only approximations are available, each neglecting different terms in the perturbation series. Most important are the DGLAP approximation [26–28] (summing terms proportional to $\log Q^2$ but neglecting terms proportional to $\log 1/x$) and the BFKL approximation [29, 30] (vice versa). As data used in this study tends to be at rather high x_{Bj} (typically larger than 0.1), and high factorization scale (larger than $\gtrsim$30 GeV^2), the DGLAP scheme is the most suitable for this analysis.

The DGLAP Evolution Equations

The DGLAP equations describe the evolution of the parton densities $f_{q/g}(x, Q^2)$ (q denotes a quark density, g the gluon density) from a starting scale $Q^2 = Q_0^2$ to an arbitrary scale Q^2:

$$\frac{\mathrm{d}f_q(x,Q^2)}{\mathrm{d}\log Q^2} = \frac{\alpha_s}{2\pi}\int_x^1 \frac{\mathrm{d}y}{y}\left[P_{qq}\left(\frac{x}{y}\right) f_q(y,Q^2) + P_{qg}\left(\frac{x}{y}\right) f_g(y,Q^2)\right], \tag{2.10}$$

$$\frac{\mathrm{d}f_g(x,Q^2)}{\mathrm{d}\log Q^2} = \frac{\alpha_s}{2\pi}\int_x^1 \frac{\mathrm{d}y}{y}\left[P_{gg}\left(\frac{x}{y}\right) f_g(y,Q^2) + \sum_q P_{gq}\left(\frac{x}{y}\right) f_q(y,Q^2)\right]. \tag{2.11}$$

The splitting functions P give the probability of a parton with relative momentum fraction $(1-z)$ being emitted from the mother parton. In leading order they are defined as follows:

$$P_{qq}(z) = \frac{4}{3}\frac{1+z^2}{1-z}, \qquad P_{qg}(z) = \frac{1}{2}\left(z^2 + (1-z)^2\right), \tag{2.12}$$

$$P_{gg}(z) = 6\left(\frac{z}{1-z} + \frac{1-z}{z} + z(1-z)\right), \qquad P_{gq}(z) = \frac{4}{3}\frac{1+(1-z)^2}{z}. \tag{2.13}$$

The DGLAP evolution equations describe how a parton with a momentum fraction x_{Bj} emerges from a parton with a higher momentum fraction y. Using the DGLAP equations

it is possible to evaluate the parton densities at any scale Q^2 as long as they are known at one particular scale Q_0^2. Thus they are a powerful tool in the determination of parton densities, as they reduce the problem of finding two-dimensional parton-densities $f_i(x, Q^2)$ to the one-dimensional problem of finding appropriate functions $f_i(x, Q_0^2)$. The evolution of the parton distributions can be visualized in form of a ladder digram as shown in Figure 2.3. In the DGLAP approximation the dominant contributions are diagrams that show strong ordering in the transverse momenta of the propagator gluons and simple ordering in their longitudinal momenta:

$$Q^2 \gg \cdots \gg k_{\perp,i+1}^2 \gg k_{\perp,i}^2 \gg \cdots \gg k_{\perp,1}^2, \tag{2.14}$$

$$1 > x_1 > \cdots > x_i > x_{i+1} > \cdots > x. \tag{2.15}$$

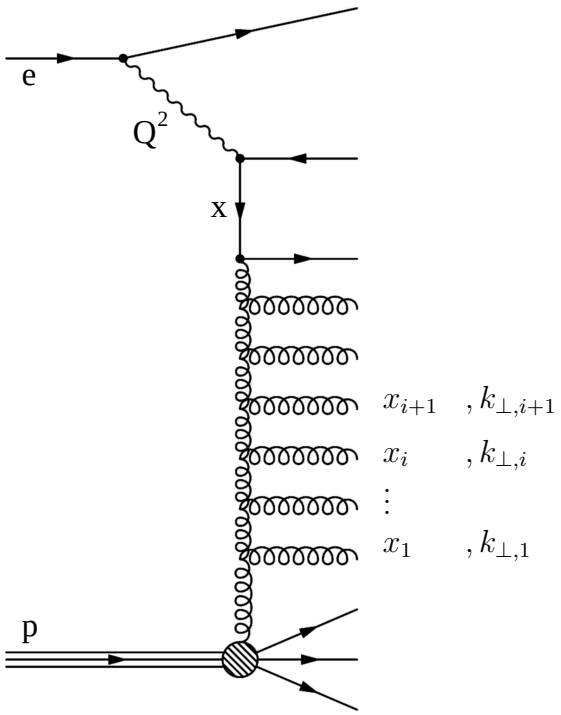

Figure 2.3: Ladder diagram of the QCD parton evolution. The longitudinal and transverse momenta of the emitted gluons are labeled x_i and $k_{\perp,i}$.

2.2.3 Hadronization

All calculations considered here were based on quarks and gluons as basic degrees of freedom. However, due to the phenomenon of confinement, only colour neutral hadrons exist at time- and distance scales that are actually physically observable. After the initial hard interaction described in the quark parton model discussed above, a multitude of much softer interactions between the outgoing particles leads to the formation of hadrons which are finally observed in the detector. Due to the low scales involved this hadronization process is theoretically poorly understood, as perturbative QCD cannot be readily applied. Instead, phenomenological models are used to predict the hadronic final state of the parton interactions. In this study, the Lund string model [31, 32] is

used, others like the cluster fragmentation model [33] exist, but were not used in this work.

2.3 Diffractive Scattering

The term diffractive scattering originates from hadronic interactions where it is used to describe elastic scattering at low momentum transfer. These soft processes dominate the total hadron-hadron scattering cross section while hard scattering events are relatively rare. Due to the strong coupling increasing at lower scales (see 2.2.1), the soft processes are not accessible to perturbative QCD. However, it is possible to describe them in phenomenological models. In particular Regge phenomenology was introduced in the early 1960's [3, 4] before the advent of QCD to interpret soft hadronic interactions in terms of meson exchange. Due to the lack of predictive power of QCD at low scales, Regge phenomenology is still being actively developed for the study of these soft processes.

2.3.1 Regge Phenomenology

In Regge phenomenology the exchanges of different mesons are not treated separately, instead mesons of different angular momentum but otherwise identical quantum numbers are treated together. These so called Regge trajectories can then be used instead of the multitude of individual mesons to calculate the transitional amplitude. In the regime of high energy, small angle scattering (i.e. $s \to \infty$ and $t/s \to 0$) the cross section can then be written as:

$$\frac{\mathrm{d}\sigma}{\mathrm{d}t} \sim (\beta_a(t)\beta_b(t))^2 \left(\frac{s}{s_0}\right)^{2(\alpha(0)+\alpha'\cdot t-1)}, \tag{2.16}$$

where $\beta(t)$ is derived from the form-factor of the scattered hadrons, s_0 defines the hadronic scale (usually $s_0 \simeq 1\ \mathrm{GeV}^2$) and $\alpha(0)$ and α' are related to the masses of the mesons in the trajectory. The functions $\beta(t)$ are often parameterized as exponential functions e^{bt}.

This equation for the scattering cross section can be exploited via the optical theorem to study total cross sections of elastic scattering as mentioned above:

$$\sigma_{tot} = \frac{1}{s}\Im T(s, t=0) \sim \beta_a(0)\beta_b(0)s^{\alpha(0)-1}. \tag{2.17}$$

Thus the rise of the total hadronic scattering cross section, which is observed with rising center of mass energy s, can be interpreted as deriving from a Regge trajectory with $\alpha(0) > 1$. However, all known meson families have $\alpha(0) < 0.6$. For this reason the pomeron trajectory was postulated by Gribov [34] to accommodate the data. As the pomeron mediates elastic scattering it has to have vacuum quantum numbers ($C = P = +1$). The nature of the pomeron in terms of QCD has long been subject of debate. No conclusive interpretation has been found, although there are attempts to explain the pomeron as the trajectory of a family of glue-balls [35].

2.3.2 Diffraction in DIS

The electron proton collider HERA provides an excellent experimental testing ground for the study of the parton contents of the pomeron. Diffractive processes occur if the hadronic final state of the reaction separates into two parts (here called X and Y) clearly separated in rapidity (the rapidity is defined as $\frac{1}{2}\ln\frac{E+p_z}{E-p_z}$), where the Y-system is an elastically scattered proton or low mass excited state (see Figure 2.4). This gap indicates that the exchange between the two systems X and Y is colour neutral, as otherwise products of the hadronization would be expected to fill the gap. The exchange is typically interpreted as a pomeron. The invariant masses of the two systems are called M_Y and M_X. The longitudinal momentum fraction lost by the proton and carried

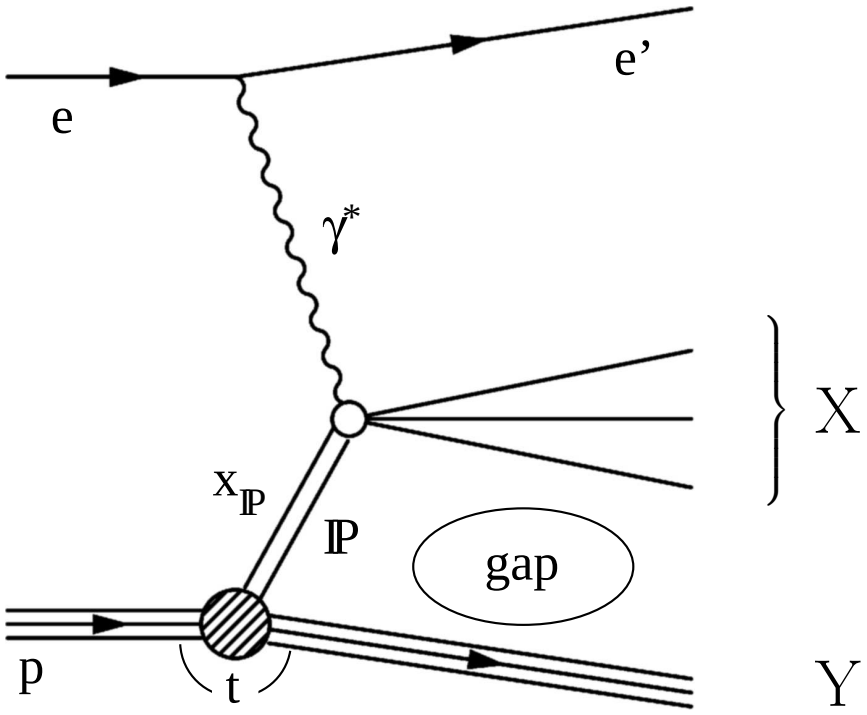

Figure 2.4: Diagram of diffractive scattering in DIS.

by the pomeron $x_{I\!P}$ is defined as:

$$x_{I\!P} = \frac{q \cdot (P - p_Y)}{q \cdot P}. \tag{2.18}$$

With this one can define the quantity β:

$$\beta = \frac{x_{Bj}}{x_{I\!P}} = \frac{Q^2}{2q \cdot (P - p_Y)}. \tag{2.19}$$

β can be interpreted as the longitudinal momentum fraction the struck parton takes in the colourless exchange (see Figure 2.5).

2.3.3 Factorization in Diffractive DIS

Events of this type can then be used to study the pomeron structure similar to studies of the proton structure in the light of the quark parton model. Just as inclusive DIS processes can be described in terms of universal parton densities of the proton and parton-parton scattering matrix elements [8, 9], it can be proven that diffractive DIS processes can be factorized into universal diffractive parton densities f_i^D and matrix elements [7] as well. The cross section is written as the convolution of the parton densities and the matrix elements:

$$d\sigma_{ep\to eXY}(|t|, M_Y, x_{I\!P}, \beta, Q^2) = \sum_i f_i^D(|t|, M_Y, x_{I\!P}, \beta, Q^2) \otimes d\hat{\sigma}^{ei}(Q^2, x_{I\!P} \cdot \beta = x_{Bj}), \tag{2.20}$$

summed over all quark flavors i. The diffractive parton densities f_i^D are a universal (i.e. process independent) property of the proton. The partonic cross sections $d\hat{\sigma}^{ei}$ are identical to the ones known from non-diffractive DIS and calculable in perturbative QCD for many processes. Therefore factorization opens the possibility to extract the universal diffractive parton densities from inclusive diffractive scattering and use those densities to predict the cross sections of other processes (i.e. dijet production in this study).

For inclusive diffractive scattering (i.e. X may be any final state) at leading order, the scattering matrix element is identical to equation 2.3 and a diffractive structure function similar to equation 2.4, $F_2^{D(5)}$, can be introduced:

$$\frac{\mathrm{d}^5\sigma_{ep\to eXY}}{\mathrm{d}x_{I\!P}\mathrm{d}\beta\mathrm{d}Q^2\mathrm{d}M_Y\mathrm{d}t} = \frac{4\pi\alpha_{em}^2}{\beta^2 Q^4}\left(1 - y + \frac{y^2}{2(1 + R^{D(5)})}\right) F_2^{D(5)}. \tag{2.21}$$

The ratio of the longitudinal and transverse photon cross sections is denoted as $R^{D(5)}$. This quantity, however, will be neglected in the following (as it has been in equation 2.4). In the measurement presented here, the outgoing system Y is not directly measured, so that M_Y and $|t|$ can only be constrained to within certain bounds ($M_Y < 1.6$ GeV and $|t| < 1.0$ GeV^2). Integrating over these quantities leaves the following three-fold differential cross section:

$$\frac{\mathrm{d}^3\sigma_{ep\to eXY}}{\mathrm{d}x_{I\!P}\mathrm{d}\beta\mathrm{d}Q^2} = \frac{4\pi\alpha_{em}^2}{\beta^2 Q^4}\left(1 - y + \frac{y^2}{2}\right) F_2^{D(3)}(x_{I\!P}, \beta, Q^2). \tag{2.22}$$

Resolved Pomeron Model

For two reasons the above equation (2.22) is not quite satisfactory. Firstly, a structure function depending on $x_{I\!P}$ cannot easily be interpreted as the partonic structure of a unique pomeron. The second consideration is experimental. A main obstacle for the experimental determination of the diffractive structure function using a fit is the fact that it depends on five (three, if integrated over $|t|$ and M_Y) independent variables (compared to two in the case of ordinary DIS) which can be further reduced by one by imposing the DGLAP equations as constraint.

To further reduce the number of dimensions in the fit, it is possible to make a physically motivated ansatz for the diffractive structure function which also allows a meaningful interpretation of the results in terms of the pomeron [10, 11]. Here one can visualize diffractive DIS as the proton emitting a pomeron, which then undergoes a hard interaction with the electron (see Figure 2.5) resolving the partonic structure of the pomeron. In this case the structure function (and accordingly the parton densities)

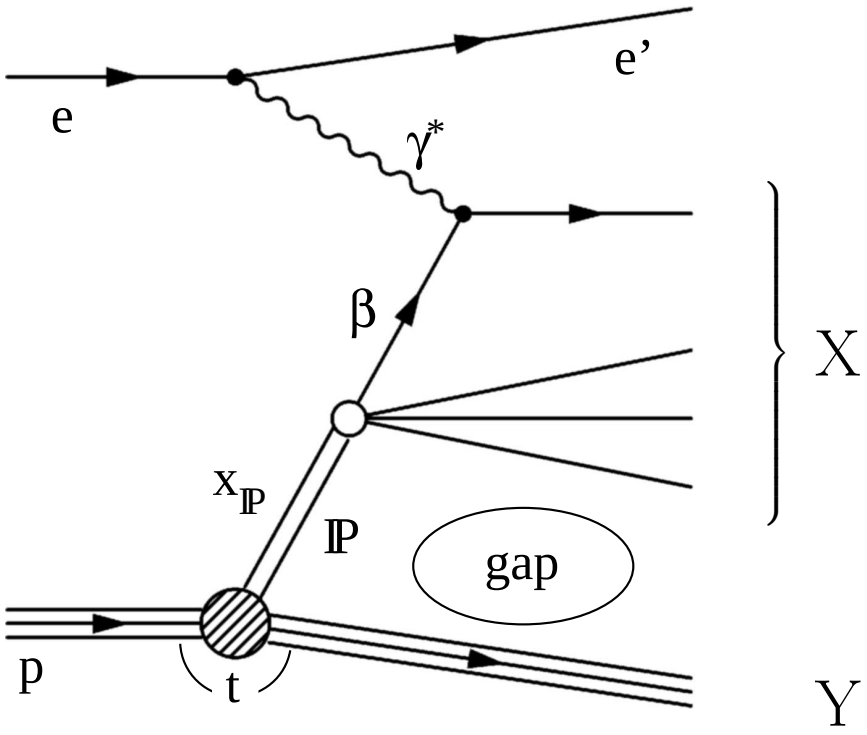

Figure 2.5: Diagram of diffractive scattering in DIS in the resolved pomeron model. The parton densities of the pomeron are probed by the virtual photon.

factorize into a pomeron flux in the proton and the partonic structure of the pomeron:

$$F_2^{D(3)}(x_{I\!P}, \beta, Q^2) = f_{I\!P}(x_{I\!P}) \cdot F_2^{I\!P}(\beta, Q^2). \tag{2.23}$$

The flux factor $f_{I\!P}(x_{I\!P})$ can be interpreted as the probability of finding a pomeron within the proton, while the pomeron structure function $F_2^{I\!P}(\beta, Q^2)$ describes the parton densities of the pomeron $f_i^{I\!P}$:

$$F_2^{I\!P}(\beta, Q^2) = \sum_i e_i^2 \beta f_i^{I\!P}(\beta, Q^2), \tag{2.24}$$

Especially in the region of high $x_{I\!P}$ it is necessary to also consider the effects of the sub-leading Regge trajectory, here called reggeon, which is introduced analogously to the pomeron (neglecting possible interference terms):

$$F_2^{D(3)}(x_{I\!P}, \beta, Q^2) = f_{I\!P}(x_{I\!P}) \cdot F_2^{I\!P}(\beta, Q^2) + f_{I\!R}(x_{I\!P}) \cdot F_2^{I\!R}(\beta, Q^2). \tag{2.25}$$

For the parton densities of the reggeon a parameterization of the pion is used [36]. Both flux factors are parameterized in the Regge inspired form (prior to integration over t):

$$f_{\{I\!P,I\!R\}}(x_{I\!P}, t) = C_{\{I\!P,I\!R\}} \left(\frac{1}{x_{I\!P}}\right)^{2\alpha_{\{I\!P,I\!R\}}(t)-1} e^{b_{\{I\!P,I\!R\}}t}, \tag{2.26}$$

with

$$\alpha_{\{I\!P,I\!R\}}(t) = \alpha_{\{I\!P,I\!R\}}(0) + \alpha'_{\{I\!P,I\!R\}} \cdot t. \tag{2.27}$$

It should be noted that the flux factor as determined from DIS (see for example [37]), significantly differs from the parameters observe in hadronic scattering.

Dijets in Diffractive DIS

The inclusive cross section in diffractive DIS (allowing all final states X) is dominated by the scattering of quarks from the pomeron as shown in Figure 2.5. This allows for the accurate extraction of quark densities from such data as done in [12]. However at high momentum fractions β the gluon density can only be determined with some difficulty and considerable uncertainty, by measuring the Q^2 dependence of the quark density. Other final states are more directly sensitive to the gluon density. In particular dijet production (with at least two jets in the system X) is dominated by the boson gluon fusion process shown in Figure 2.6. Thus this process can be used to check the

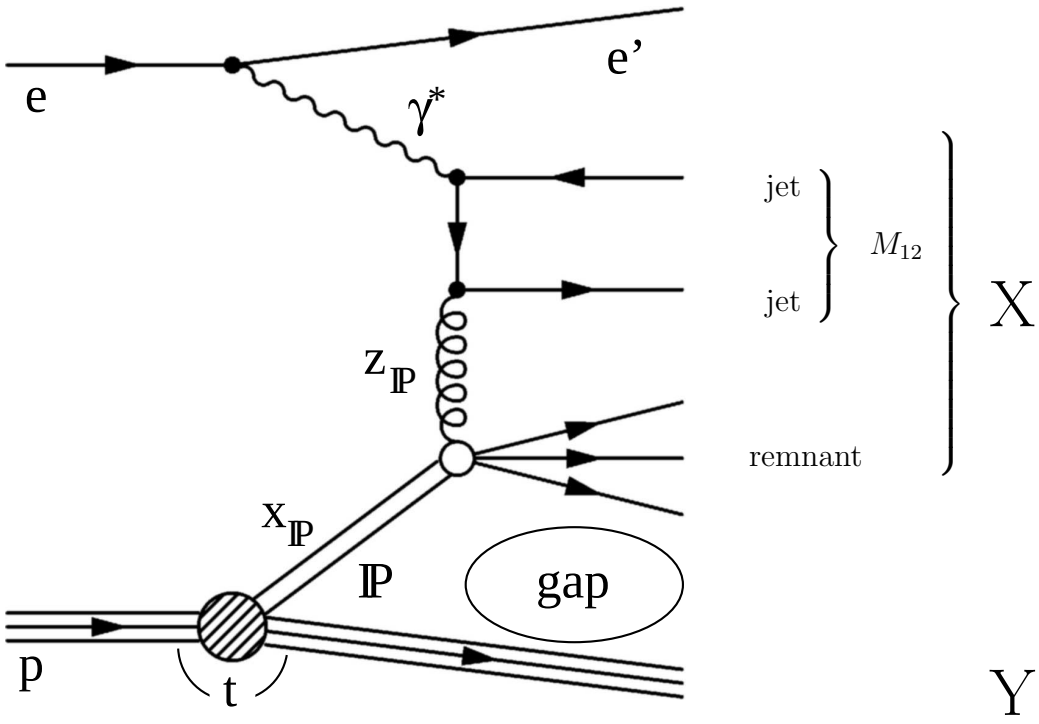

Figure 2.6: Diagram showing diffractive dijet production in the resolved pomeron model.

validity of the gluon distributions derived from measurements of inclusive diffractive DIS as has been done in [13]. In this work the larger data set available with its lower statistical errors is exploited by directly fitting a gluon density to dijet cross sections.

The kinematics of this process is slightly different from the inclusive diffraction described above. In particular the momentum fraction of the parton that enters the hard interaction (called $z_{I\!P}$) is not identical to β (the momentum fraction of the quark interacting with the photon). Assuming the gluon has a four momentum v, $z_{I\!P}$ can be expressed as:

$$z_{I\!P} = \frac{q \cdot v}{q \cdot (P - p_Y)}. \tag{2.28}$$

In the quark parton model the diffractive dijet cross section is then the convolution of the hard scattering matrix elements for the $eq \to e\ jets$ and $eg \to e\ jets$ with the diffractive parton densities $f_i^{I\!P}(z_{I\!P}, \mu_f)$ evaluated at $z_{I\!P}$ and the pomeron flux $f_{I\!P}(x_{I\!P})$. The factorization scale for dijet production is not uniquely determined. In this study the sum of the two available hard scales, $Q^2 + p_\perp^{\star 2}$ was chosen, where $p_\perp^{\star 2}$ denotes the transverse momentum of the hardest jet in the $\gamma^\star$p rest frame. The dependence of the theoretical predictions on the exact choice of the factorization and renormalization scales is the major theoretical uncertainty of these predictions.

Chapter 3

HERA and the H1 Detector

3.1 HERA

The data studied in this thesis was collected at the Hadron Elektron Ring Anlage (HERA), located at the Deutsches Elektronen Synchrotron (DESY) in Hamburg. A schematic view of the site is shown in Figure 3.1. Four experimental areas are located

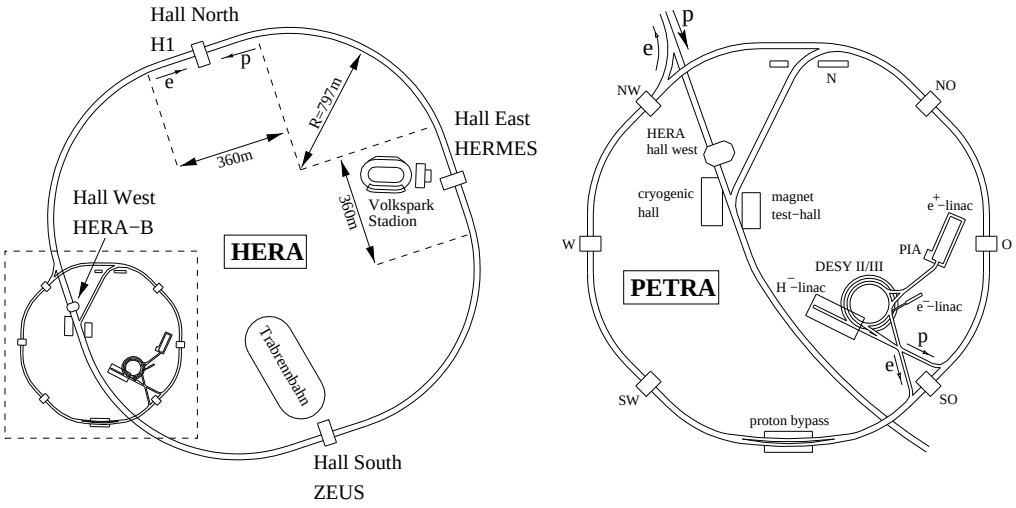

Figure 3.1: The HERA *ep* collider facility and its injection and pre-acceleration systems.

along the main HERA accelerator tunnel, all four of which housed experiments during the data taking. The data used in this study were recorded with the H1 experiment, located in the north experimental hall, during the years 1999 and 2000. In this period HERA was colliding protons with positrons. The energy of the protons and positrons were 920 GeVand 27.5 GeVrespectively, providing a center-of-mass energy of 319 GeV.

The H1 experiment (pictured in Figure 3.2) is a typical large acceptance particle detector, surrounding the nominal point of particle interaction in a shell-like layered structure. Due to the different energies of the positron and the proton, the center of mass system of the collision is boosted in the direction of the proton. Accordingly

the H1 detector was designed asymmetric to ensure the best possible measurement of the asymmetric collisions. In the following only the subsystems of the H1 detector extensively used in this analysis are introduced. A more detailed description of the H1 detector can be found in [38, 39].

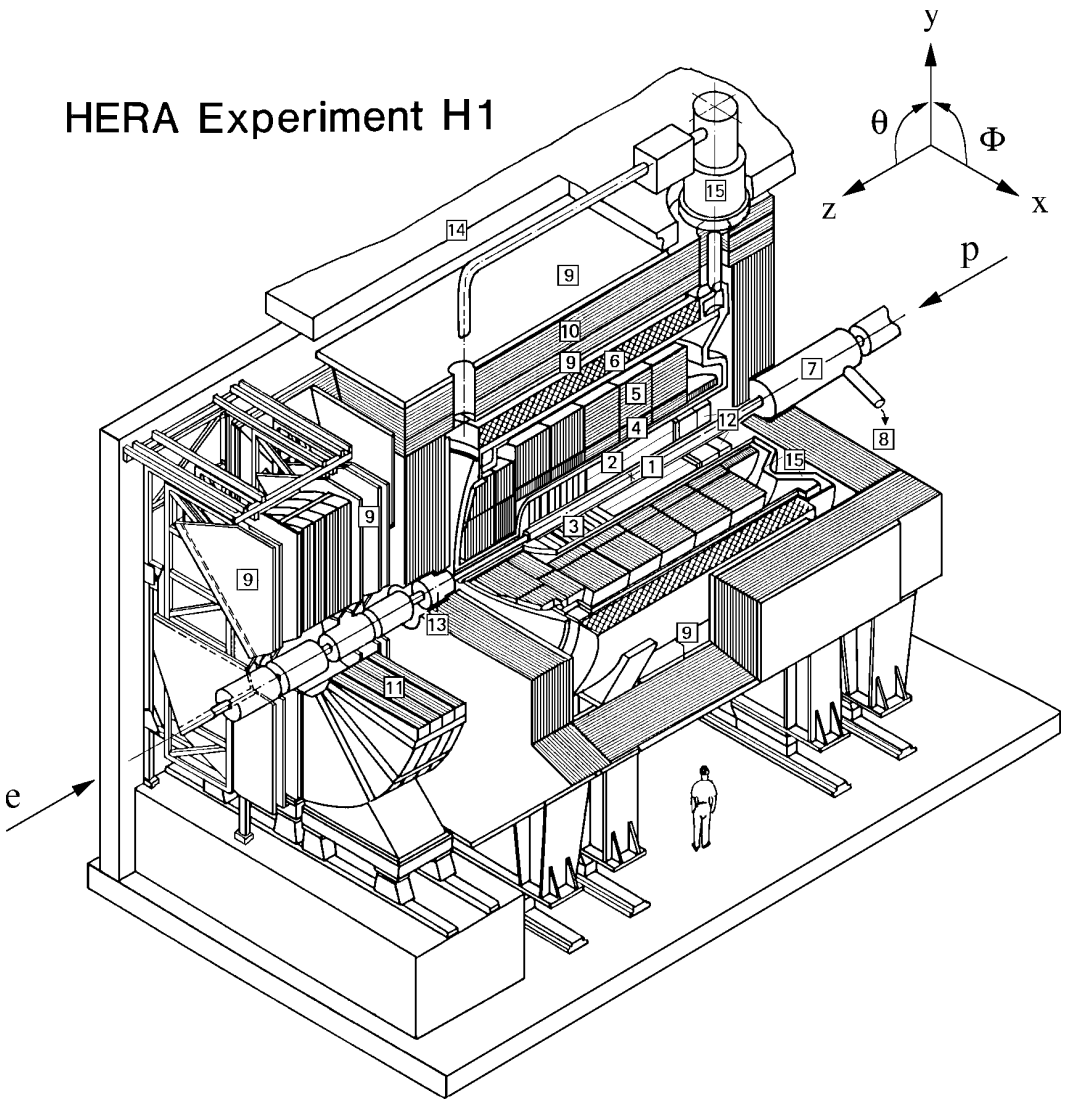

Figure 3.2: The H1 detector.

3.2 Calorimeters

To measure the energy of particles emerging from the interaction the H1 detector contains several calorimeters, each specialized for a different task.

3.2.1 Liquid Argon (LAr) Calorimeter

The main component for energy measurements in the H1 detector is a liquid argon calorimeter (see Figure 3.3 and numbers 4 and 5 in Figure 3.2) which is designed as a sampling calorimeter. It covers the range in pseudo rapidity $3.4 > \eta >$ -1.4. In this analysis the LAr calorimeter is mainly used to measure the energy of the jets emerging from the interaction. The calorimeter is divided into an inner electromagnetic

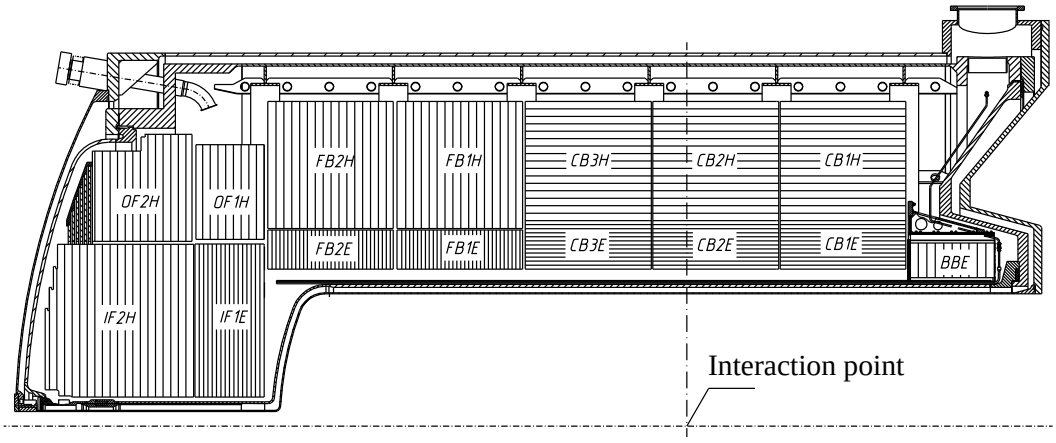

Figure 3.3: Cross section view of the LAr calorimeter along the beam direction. Only the upper half is shown.

and an outer hadronic region. While both regions share liquid argon as the active material, the two parts have different absorber materials, lead for the electromagnetic part and stainless steel for the hadronic part. Overall the material in the electromagnetic calorimeter amounts to 20 to 30 radiation lengths (depending on polar angle). Similarly depending on the polar angle the material in the hadronic part of the LAr calorimeter is 5 to 8 interaction lengths thick. Unfortunately the LAr calorimeter is non-compensating, i.e. the response to electromagnetic and hadronic energy deposition is somewhat different. This causes little problems for electromagnetic particles, however the uncertainty in the energy measurement for hadrons is increased as the particle shower generated by impacting hadrons contains a varying fraction of secondary electromagnetic particles. The energy resolution with this setup is

$$\sigma_E/E = 50\%/\sqrt{E/\mathrm{GeV}} \oplus 2\% \tag{3.1}$$

for the hadronic calorimeter and

$$\sigma_E/E = 12\%/\sqrt{E/\mathrm{GeV}} \oplus 1\% \tag{3.2}$$

for the electromagnetic part.

Diffraction is a phenomenon that mainly occurs at small positron scattering angles, causing the positron to generally impact in the backward calorimeter described in the next section. Thus the performance of the calorimeter for electromagnetic interactions plays only a minor role in this study, while the hadronic performance is of much greater importance due to its use in the measurements of jet momenta.

3.2.2 Backward Lead and Scintillator Calorimeter

The backward region (-1.42 > η > -3.82) of the H1 detector is covered by the so called 'spaghetti calorimeter' SPACAL [40] (number 12 in Figure 3.2). Just like the LAr calorimeter the SPACAL is a sampling calorimeter. However, here the absorber material is lead into which scintillator fibers have been embedded as active material. The calorimeter consists of an electromagnetic part of 28 radiation lengths thickness and a hadronic part, which corresponds to 2 interaction lengths.

In this analysis the SPACAL is mainly used to measure the scattered positron, while the jets are required to lie in the acceptance of the LAr calorimeter. For this reason the electromagnetic part of the SPACAL is of greater importance for the measurements, while the hadronic part plays only a minor role in the suppression of background. The resolution of the electromagnetic part of the SPACAL is

$$\sigma_E/E = 30\%/\sqrt{E/\mathrm{GeV}} \oplus 7\%. \tag{3.3}$$

3.3 Tracking

In order to measure the momenta of charged particles the H1 detector has a solenoidal magnetic field of 1.2 T strength, produced by a superconducting magnet just outside of the LAr calorimeter (see number 6 in Figure 3.2). The curvature of the trajectories, and thus the momentum, of the charged particles in the magnetic field can be measured with appropriate tracking detectors. The accuracy of the momentum measurement grows with increasing curvature, i.e. decreasing momentum. Thus the momentum measurements complement the calorimetric measurements, which achieve highest accuracy at high momenta. The combination of tracking information with the calorimetric energy measurement allows for the reliable reconstruction of jets of lower momentum than calorimetric measurements alone. This greatly helps the accuracy of the measurement presented here, as the transverse momenta of the jets in this analysis are much lower than the ones typically encountered in jet measurements of inclusive (i.e non diffractive) deep inelastic scattering

Figure 3.4 shows cross sections of the central tracking detectors of the H1 experiment along and perpendicular to the beam axis. Clearly visible is the division into forward backward and central parts of the tracking system.

The central part of the tracking system covers a polar angle from 25° to 155°. It consists of several layers of sub-detector concentric around the beam axis, the most important of which are the so called central jet chambers 1 and 2 (see Figure 3.4, right). These are drift chambers with their sense-wires parallel to the beam axis allow for a high precision of measurement in the $r - \phi$ plane. The position in the z direction can only coarsely be determined by charge division along the wire. For an accurate determination of the z position two small drift chambers with sense wires perpendicular to the beam axis lie within each of the main jet chambers.

Additionally two layers of proportional chambers are integrated into the central tracking device (labeled CIP and COP in Figure 3.4). They are not primarily used for the reconstruction of tracks, instead they were optimized for a fast response time at the cost of spatial resolution, so that they can be used to trigger the H1 detector.

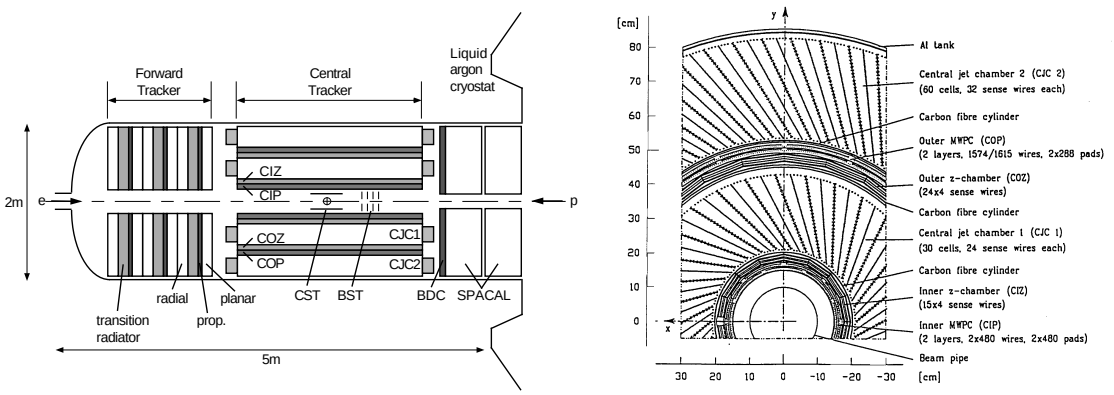

Figure 3.4: The H1 tracking system. Left: Cross section of the tracking system along the beam axis. Right: Cross section of the central tracking detector perpendicular to the beam axis.

The backward drift chamber measures charged particles in the backward region of the H1 detector at a polar angle between 152° and 177°. The position measurement of positron candidates in the BDC can be used to improve the measurement of the polar angle compared to a measurement with the SPACAL alone. The spacial resolution of the BDC perpendicular to the beam line is $\sigma \approx 340\ \mu$m, which corresponds to a polar angle resolution of $\sigma_\theta \approx 0.5$ mrad.

Particles reaching the forward drift chambers need to pass through the readout electronics of the central tracking system, which corresponds to roughly two radiation lengths of material. This leads to a large multiplicity of tracks in the forward tracking system due to secondary interactions and the corresponding problems in track reconstruction and interpretation. For this reason the forward tracking system is not used in this analysis.

The part of the tracking system closest to the interaction point are the central and backward silicon trackers (labeled CST and BST in Figure 3.4). They provide superior spatial resolution close to the event vertex. As their main purpose is the identification of secondary vertices for the identification of heavy quarks, their impact on the measurement of jet momenta is small.

3.4 Forward Tagging

While it would be desirable to detect the elastically scattered proton of diffractive events, the H1 detector had during the data taking period of 1999 and 2000 no component of suitably large acceptance that could perform this measurement. Instead diffractive events are selected by the requirement that no proton dissociation system is detected in the forward (i.e. along the proton direction) parts of the H1 detector. This so called forward tagging or rapidity gap method cannot guarantee that the outgoing Y system was an elastically scattered proton, but it can ensure that the momentum transfer $|t|$ at the proton vertex and the mass of the dissociation system M_Y are reasonably low. In addition to the LAr calorimeter the following detector components were used for

tagging.

3.4.1 Forward Muon Detector

The Forward Muon Detector (FMD) is situated directly forward of the LAr calorimeter (see Figure 3.2 numbers 9 and 11). Its main purpose is the identification and momentum measurement of forward going muons. This is accomplished by two sets of drift chambers of 6 layers each, which are separated by a toroidal magnet. In this study, however, only the first 6 layers covering a pseudorapidity up to 3.4 will be used to identify the proton remnant in proton dissociative events.

3.4.2 Proton Remnant Tagger and Forward Tagging System

At 24 m along the beam-line a tagging-station was installed in 1997 for the specific purpose of tagging the proton remnant in dissociative events. It consists of seven plastic scintillator panels arranged around the beam-pipe. In 1999, after the upgrade of HERA to higher proton beam energy, the system was extended by stations at 9, 16, 53 and 92 m for a total coverage in pseudorapidity of $6 < \eta < 7.5$

During the data taking period of 1999 and 2000 the panels 6 and 7 of the proton remnant tagger showed high level of noise. They were excluded from the analysis. The other scintillator panels showed significant noise in specific runs during the data taking, these runs were also excluded.

The η-range of 3.5 to 5.5 is covered by the PLUG calorimeter. However, this detector component was not used in this analysis, as the small additional tagging power was outweighed by problems due to noise and beam-induced background.

3.5 Trigger System

At HERA, the rate at which positron and proton bunches cross at the interaction region is 10.4 MHz under optimal conditions. However, the rate of collisions producing a measurable signal in the H1 detector is much lower, around 50 kHz, as not every bunch crossing leads to an energetic scattering event. This event rate also includes a number of events that originate from collisions of the beams with gas atoms in the beam pipe and of beam particles that have been lost from the beam colliding with the beam-pipe or other hardware. Additionally the H1 detector measures the signals of particles produced by cosmic rays at a rate of about 700 Hz. Due to hardware and cost limitations the rate at which events can be permanently stored is only about 20 Hz. Thus a trigger system is necessary to select those events that are most promising for future analysis.

At the H1 detector the trigger system consists of four distinct levels (L1-L4), of which L3 was not used while the data for this study was taken. At the first trigger level (L1) the decision, whether an event should be discarded, has to be made within 2.3 μs of the interaction, a time corresponding to 24 further bunch crossings. If the trigger decision is positive, the next trigger level is activated and data-taking is interrupted, i.e. dead time starts to accumulate. Basis for the decision of the first level trigger are 256 so

called trigger elements, which are directly obtained from detector signals. These trigger elements are then logically connected to 128 sub-triggers, each of which is designed to select a particular class of events. Activation of any of these sub-triggers starts the second level readout process.

As some event topologies are very common, the sub-triggers sensitive to these topologies are active at a rate higher than desirable. The rates of these sub-triggers are then reduced with a pre-scale factor. This means that for a pre-scale factor of n only every nth activation of the sub-trigger is routed to the second trigger level. Thus a pre-scale factor of one means no reduction, while for a factor of n only every nth event is passed to level 2.

On the following levels the detector signals are analyzed with increasing sophistication, each time rejecting a fraction of the events, until a rate is reached that can be permanently stored. As the trigger used in this analysis does not make use of the trigger stages L2 and L3, they will not be discussed in detail. At the trigger level L4, all events are reconstructed and classified into several categories. At this point in the trigger pipeline, events that do not correspond to these categories are prescaled again at this level. The event sample of this analysis, contains no events with L4 prescale factors larger than 1.

3.6 Luminosity System

In order to obtain a cross section from the measurement of the event rate knowledge of the (integrated) luminosity $\mathcal{L}$ is indispensable. $\mathcal{L}$ is the integral over the instantaneous luminosity L, which is the factor that connects the cross section σ and event rate dN/dt:

$$\frac{\mathrm{d}N}{\mathrm{d}t} = L \cdot \sigma. \tag{3.4}$$

Integrated over the whole measurement this yields

$$N = \mathcal{L} \cdot \sigma. \tag{3.5}$$

This also shows, how the luminosity can be measured. If the cross section of a process is well known from theory, the event rate of this process can be used to obtain the luminosity.

In the case of H1 this well known reaction is the Bethe-Heitler process ($ep \to ep\gamma$), the cross section of which can be calculated to very high precision in quantum electro dynamics [41]. In the H1 detector there is a dedicated sub-detector for measuring the rate of Bethe-Heitler events (for details see [42]) and thus determine the luminosity. There are two main components, both of them crystal calorimeters, one of which detects the scattered photon, while the other one detects the corresponding photon. Unfortunately this measurement is not entirely free of background. Interactions of the positron beam with remaining gas atoms in the beam pipe of the type $eA \to eA\gamma$ contribute a significant background rate (roughly 10%), as the higher charge of the nuclei dramatically increases the cross section. The rate of this background can be measured separately (and subsequently subtracted) by having some bunches of positrons not collide with a proton bunch. These so called pilot bunches will then only cause

background events at a rate R_0. The luminosity is then calculated from the total rate of Bethe-Heitler events R_{tot} as follows:

$$L = \frac{R_{tot} - (I_{tot}/I_0)R_0}{\sigma}, \tag{3.6}$$

where I_0 denotes the current in the pilot bunches alone, while I_{tot} represents the total positron current. σ is here the Bethe-Heitler cross section corrected for all acceptances and efficiencies.

Chapter 4

Monte Carlo Models and Fixed Order QCD Predictions

Monte Carlo models serve several purposes in a cross section measurement like the one presented here. On the one hand the primary detector signals needs to be translated into a measurement of the underlying scattering process at the hadron level. For this, events are generated with a suitable Monte Carlo model and used as input for a complete simulation of the H1 detector. The resulting simulation is subjected to the same analysis chain as the data. From the resulting sample correction factors for detector acceptance and resolution can be extracted. The important point in this step is the accurate description of the detector response.

On the other side, the predictions of QCD have to be calculated to compare them to the data. For this, the most accurate possible calculation (i.e. the highest possible order in α_s) should be used. In the case of two jet events in diffraction, calculations in next to leading order (NLO) are available. The known dependence of the QCD predictions on the parton densities can then be used to extract these densities.

4.1 Monte Carlo Models

To convert the measured event rate into a cross section, it needs to be corrected for a multitude of physical effects, that are not directly observed like the detector acceptance. For this purpose Monte Carlo Models are used, in which these effects can be studied in detail and appropriate correction factors can be extracted.

4.1.1 Signal Monte Carlo Models

The measured spectra correspond only imperfectly to the actual cross section of stable hadrons due to the finite resolution, acceptance and efficiency of the detector. In this analysis these effects corrected statistically by applying a correction factor separately for each bin of a histogram. The correction factor is derived from the signal Monte Carlo simulation by dividing the spectra of the simulation at hadron level and at detector level. This method is sensitive to migrations and can be only applied if the shapes of the data and simulation are in good agreement.

Signal Samples

The RAPGAP 3.1 program [43] was used in diffractive mode to generate the main signal simulation used for most of the corrections. RAPGAP computes the diffractive dijet cross section to leading order in α_s, assuming the resolved pomeron model. Higher order QCD effects are modeled using initial and final state parton showers in the leading $\log Q^2$ approximation. QED radiation effects are included via the HERACLES module [44]. The model calculation is restricted to the diffractive phase space of $x_{I\!P} < 0.2 \ \wedge \ M_Y = m_p$. The models used to cover the remaining phase space are discussed below. A preliminary version of the diffractive parton densities in [12] was used as input.

The signal Monte Carlo sample consists of four sub-samples listed in table 4.1, each describing a different process. In three of these, a pomeron exchange is modeled. However, they differ in the QCD matrix element and interaction with the virtual photon. In the most important sub-sample, the virtual photon interacts directly with the pomeron to produce massless outgoing quarks. The case of massive charm quarks produced by direct interaction with the photon is handled in the second sub-sample. It is also possible, that the virtual photon does not interact with the proton directly but via a fluctuation into a hadronic state. This process is suppressed with rising Q^2 and contributes only a small fraction of the events in this analysis. Because of its small contribution this process is included only for massless quarks. The hadronic structure of the photon in this case is described by the leading order SaS parton distribution functions [45]. The last process considered is the exchange of a reggeon instead of a pomeron. The luminosity of the signal simulation is roughly eight times as large as the data luminosity. The sum of the four samples listed in table 4.1 will be referred to as signal simulation.

Table 4.1: Summary of the signal Monte Carlo simulation

process	**events**	**luminosity** $[\boldsymbol{pb^{-1}}]$
light quark pomeron, direct	750,000	406.2
charm pomeron, direct	500,000	637.3
light quark pomeron, resolved	100,000	203.0
light quark reggeon, direct	690,000	203.9

Detector Effects

The finite resolution, acceptance and efficiency of the H1 detector needs to be considered in the calculation of the cross section. For this purpose the detector response for the hadron level sample generated by RAPGAP is simulated. If the correction factors between detector level and stable hadron level is to be meaningful, there should be a reasonable correlation between quantities measured at the two different levels.

However, there are noticeable differences in quantities determined at hadron and at detector level. The losses due to detector inefficiency are not perfectly modeled by the simulation. Thus M_X needs to be scaled by -4% to reduce migrations between

hadron- and detector level. For similar reasons the jet momentum needs to be scaled by -5%, as well as all dependent quantities (in particular M_{12} which enters into the computation of $z_{I\!P}$). This scaling does not affect the final cross sections as it is equally applied to the data and the Monte Carlo sample used for correcting detector effects. Figure 4.1 shows the correlation and resolution between hadron and detector level for

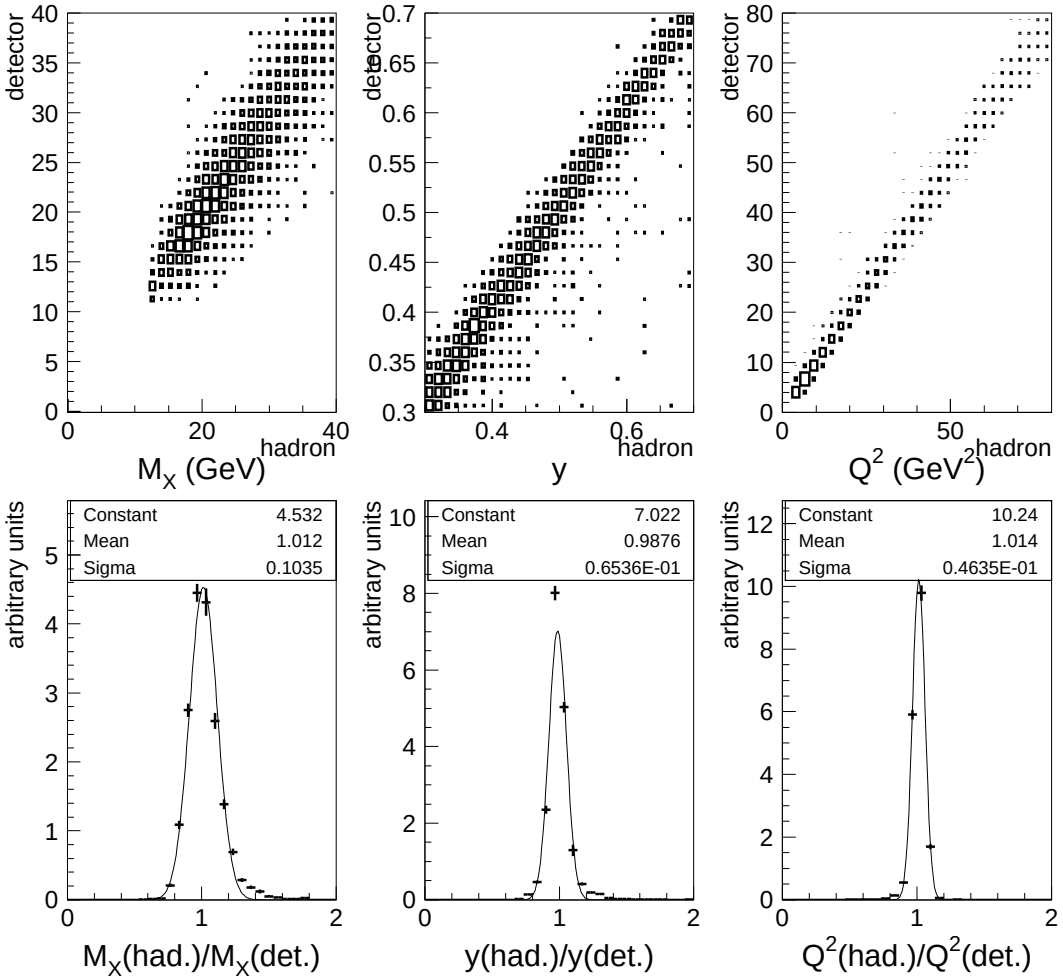

Figure 4.1: Correlation and resolution between detector and hadron quantities. Shown are the variables M_X (after rescaling by -4%), y and Q^2. All selection cuts later used in the analysis have been applied.

the variables M_X, Q^2 and y. Quantities derived from measurements of the scattered positron show a better resolution than quantities derived from the hadronic final state. For this reason, quantities that can be reconstructed from the hadronic final state as well as the scattered positron, will be reconstructed from measurements of the positron (see section 5.3 for the definitions). The variables ϕ, η and $p_\perp^\star$ for the hardest jet are shown in Figure 4.2. While the angular resolution is excellent in azimuth as well as in polar angle, there is considerable smearing in the transverse momentum of the jet. Figure 4.3 shows the variables $x_{I\!P}$ and $z_{I\!P}$. The left of the two plots of $x_{I\!P}$ has been generated without any diffractive selection applied. At high values of $x_{I\!P}$, the X system of the hadronic final state tends to be boosted so much into the proton direction, that

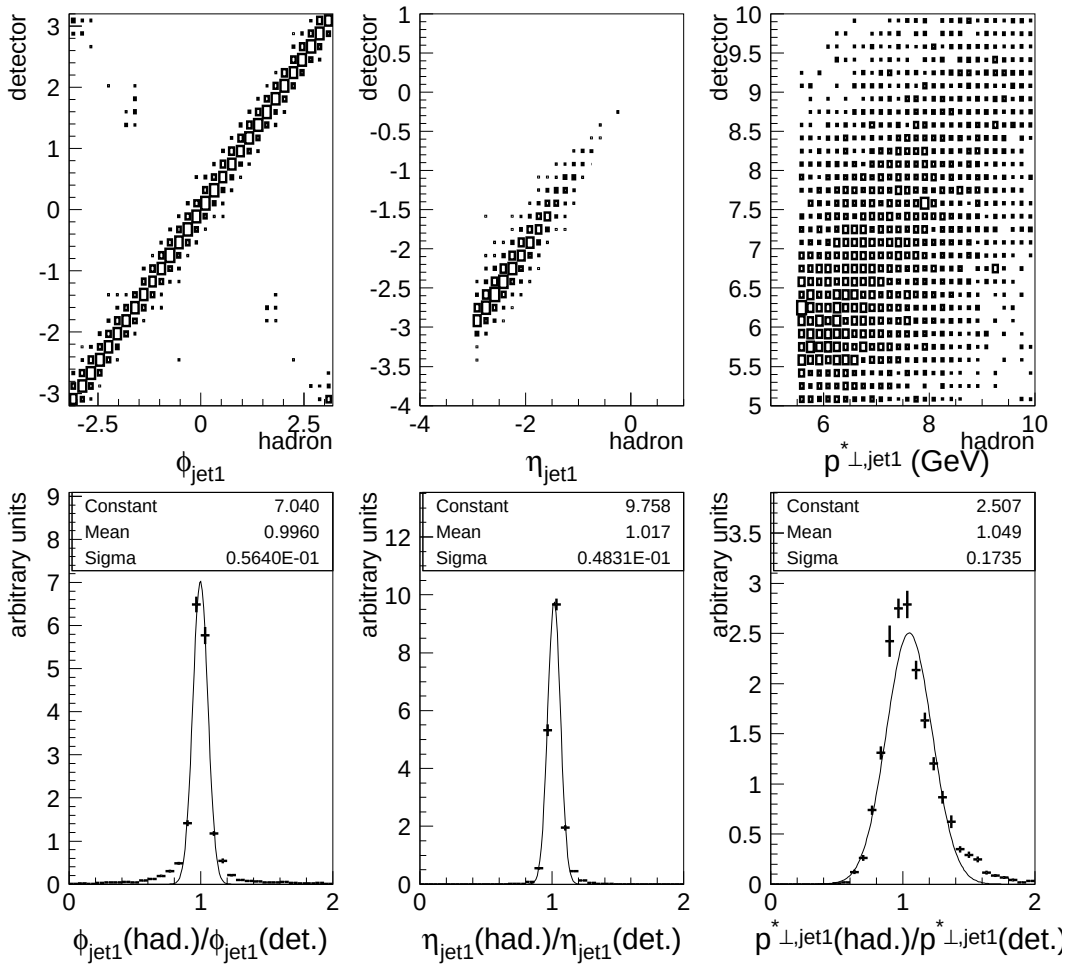

Figure 4.2: Correlation and resolution between detector and hadron quantities. Shown are the variables ϕ, η and $p^{\star}_{\perp}$ (after rescaling by -5%) of the hardest hadron-jet. All selection cuts later used in the analysis have been applied. The values for the hardest hadron jet were compared to the detector-level jet closest in angle, not the hardest jet in the detector.

a considerable part of the X system is not detected. This leads to the effect, that M_X is measured smaller at the detector level than its actual value. Restricting the measurement to small values of $x_{I\!P}$ restores a good correlation between detector- and hadron level.

Hadronization Corrections

As described below in section 4.2.3 the theoretical predictions are calculated at the level of the partons emerging from the hard interaction. To compare these results to the measured cross section at the level of stable hadrons, the effects of the hadronization need to be studied. This is done by comparing the differential cross section of a Monte Carlo model that includes hadronization before and after hadronization has taken effect. The signal Monte Carlo sample is in principle quite suitable for this purpose, but has a rather small sample size. An additional sample was generated with the

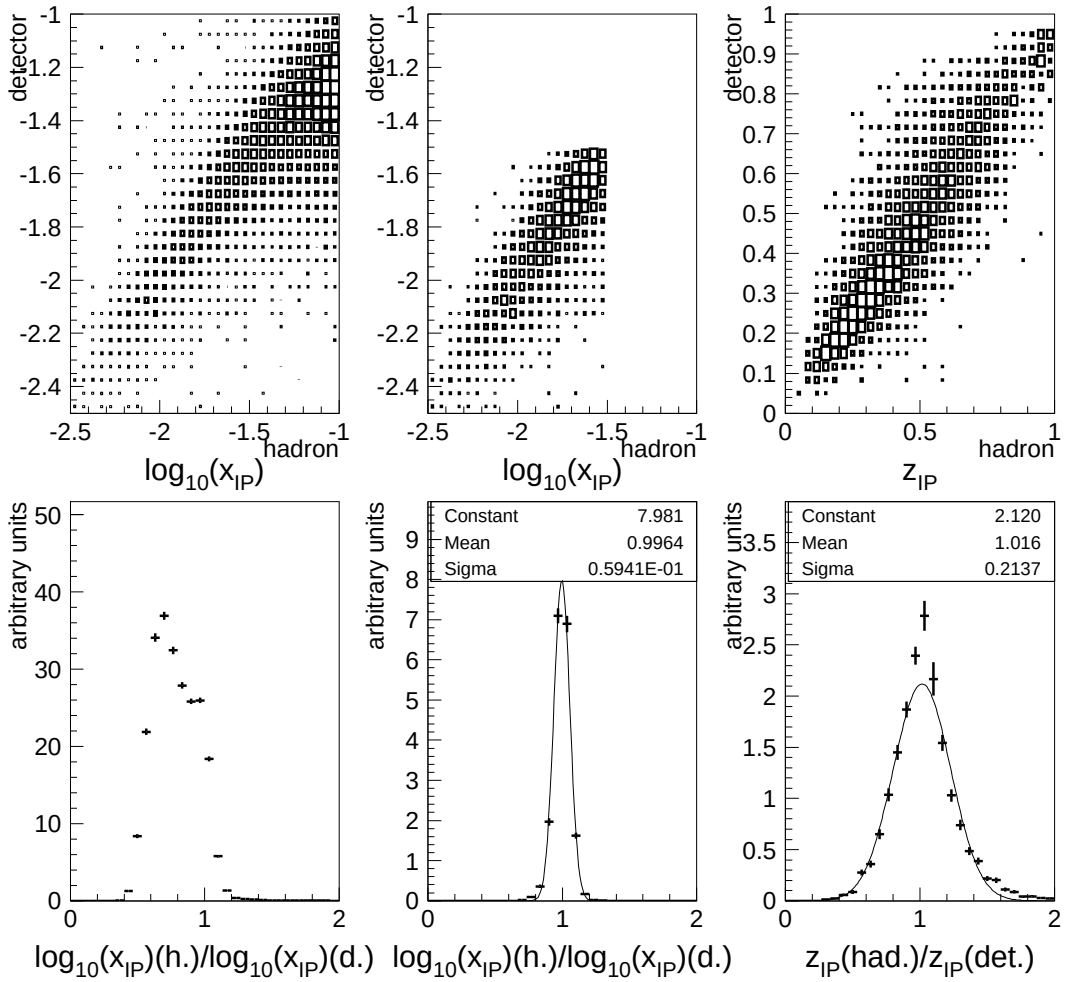

Figure 4.3: Correlation and resolution between detector and hadron quantities. Shown are the variables $x_{I\!P}$ and $z_{I\!P}$. The left plot of $x_{I\!P}$ was obtained without the diffractive selection (see section 5.5). All selection cuts later used in the analysis have been applied to the two plots on the right.

same parameters as the one described in section 4.1.1, the only difference being the absence of the time consuming detector simulation. This additional sample has three times the luminosity as the one given in table 4.1. Combining the samples reduces the statistical uncertainty on the hadronization corrections by a factor of two compared to the statistical uncertainty in the correction between detector and hadron level. The combined sample will be referred to as hadronization simulation. Additionally the exact modeling of the hadronization process is subject to systematic uncertainties, as different models produce somewhat different correction factors. However, these uncertainties have not been studied in this analysis.

Radiative Corrections

The measurement of kinematic variables that are reconstructed from measurements of the scattered positron is affected by initial- and final state QED radiation. This

introduces undesired kinematic dependences which tend to obscure the QCD process studied. To exclude the effects of QED radiation from the measured cross section, the data is multiplied by the ratio of a model prediction that does not include radiative effects and one that does. For the latter, the hadronization simulation is used, while the former (the non-radiative simulation) is generated with identical parameters, with the exception that QED radiation is disabled.

4.1.2 Non-Diffractive Background

To estimate the effects of non-diffractive background events polluting the diffractive data sample, the `RAPGAP` program is used in its inclusive DIS mode. The Monte Carlo sample used for this purpose was generated for the study of dijets in DIS [46]. It contains two subsamples, one for the direct interaction, and one with a resolved photon contribution. The simulation is based on the CTEQ5L parton densities [47].

In order to avoid double counting when combining the diffractive and non-diffractive simulations, the two samples are merged in phase space. Only events with $x_{I\!P} < 0.2 \ \wedge \ M_Y = m_p$ at the level of stable hadrons are included from the diffractive simulations, while for events with $x_{I\!P} > 0.2 \ \vee \ M_Y > 5$ GeV the non-diffractive sample is used. The remaining phase space region $m_p < M_Y < 5$ GeV is covered by the `DIFFVM` simulation discussed below. The resulting background after the diffractive selection is then subtracted from the data to extract the cross sections.

The simulation of the inclusive sample does not include the effects of QED radiation, leading to differences between simulation and data in spectra that are typically affected by radiation effects (particularly y). However, the small amount of non-diffractive background left in the final sample leads to a negligible effect ($< 1\%$) on the final cross section.

4.1.3 Proton Dissociation

The `RAPGAP` Monte Carlo model used in this study only generates events in which the outgoing hadronic system Y is an elastically scattered proton. However, as the Y system is not directly measured in the experiment, it may also be a low mass proton dissociation system. Matching the detector acceptance, the cross section presented here is defined for $M_Y < 1.6$ GeVand $|t| < 1$ GeV^2. To properly account for the contribution of proton dissociative scattering, further Monte Carlo samples are needed in addition to the signal sample to cover the whole range in M_Y.

`RAPGAP` Inclusive

The phase space of $M_Y > 5$ GeV is already included in the non-diffractive background sample, described in section 4.1.2 and needs no further consideration.

`DIFFVM`

The `DIFFVM` program [48] simulates diffractive vector meson production and includes a sophisticated treatment of the dissociating proton in the low M_Y region. It is used in this analysis to study the response of the forward detectors to low mass ($m_p < M_Y < 5$ GeV)

proton dissociation systems. The non-resonant part of the M_Y distribution is modeled by a $(1/M_Y^2)^{1+\epsilon}$ with $\epsilon = 0.08$, while the t dependence is modeled as en exponential decrease of slope 1.6 GeV^{-2}. This parameterization is motivated by measurements of diffractive vector meson production at H1 [49].

`RAPGAP` Proton Dissociation

Recently the `RAPGAP` Monte Carlo generator has been extended to include diffractive proton dissociation in addition to proton elastic diffraction. This provides the opportunity to check the validity of the assumption that the X system has negligible influence on the forward detectors.

4.2 Next to Leading Order Predictions

As the renormalization scale for the processes under investigation here tends to be rather low (as low as 25 GeV^2 for $p_\perp^{\star 2}$ as scale), the corresponding value for α_s is so large (up to ~ 0.2), that the effects of $\mathcal{O}(\alpha_s^2)$ cannot be neglected. In fact it turns out that for diffractive dijet production in DIS, the contribution of $\mathcal{O}(\alpha_s^2)$ is larger than the leading order. Thus one can expect that also terms of $\mathcal{O}(\alpha_s^3)$ may still significantly contribute to the cross sections.

As discussed in section 2.2.1, the calculation depends on the factorization- and renormalization scales. In this study, for both scales $Q^2 + p_\perp^{\star 2}$ was used, where $p_\perp^\star$ is the transverse momentum system of the hardest jet in the $\gamma^\star$p rest frame. Due to the finite order of the calculation the computed cross sections depend on the exact scale chosen in the computation. To estimate the uncertainties arising from this effect, the scale is varied by a factor of 4 and 0.25.

4.2.1 `nlojet++`

For this analysis the program `nlojet++` [50] was adapted from DIS dijet production to diffractive dijet production. In the calculation of dijet cross sections terms up to $\mathcal{O}(\alpha_s^2)$ are included. The predictions of `nlojet++` calculations will be used for comparisons to the data. This includes the comparison of data to predictions based on some given set of diffractive parton densities as well as the theoretical predictions involved in fitting diffractive parton densities to the data.

4.2.2 Adaption to Diffractive Processes

The `nlojet++` program was originally written to predict cross sections in non-diffractive DIS and hadron-hadron scattering and had to be modified to be usefully employed in the prediction of diffractive cross sections. However, under the assumption of 'Regge'-factorization `nlojet++` can be used to calculate the cross section for $I\!P$-electron scattering at fixed $x_{I\!P}$ by replacing the original parton densities of the proton by those of the pomeron and lowering the beam energy by a factor of $x_{I\!P}$. The results for different values of $x_{I\!P}$ are then summed, weighted by the corresponding pomeron flux and width of the $x_{I\!P}$ interval. For this study, the cross section prediction is evaluated at 24 values

of $x_{I\!P}$ evenly spaced in $\log(x_{I\!P})$, ranging from 0.00211 to 0.0291. Similarly the reggeon contribution was computed using parton densities from [36] and the flux factors derived from inclusive diffractive scattering where an elastically scattered proton is actually detected [37].

4.2.3 Hadronization Corrections

The `nlojet++` program predicts cross sections at the level of the partons emerging from the hard interaction. In contrast the objects physically interacting with the H1 detector are hadrons that emerge from a series of soft interactions between the outgoing partons. This hadronization process (see section 2.2.3) causes migrations in variables involving the hadronic final state. Additionally there are variables, in particular $x_{I\!P}$, whose definition differs between hadron- and parton level. While on the parton level $x_{I\!P}$ is defined as the actual momentum fraction of the pomeron, it is calculated on hadron level from the hadronic quantity M_X. Only the quantities derived from measurements of the positron alone are undisturbed by hadronizaton.

The effects of the hadronization are estimated by the study of the hadronization Monte Carlo model described in section 4.1.1. The cross section is determined in the Monte Carlo sample once at the level of stable hadrons and once at the level of the partons. The correction factor is computed separately for each bin of each distribution by dividing the hadron level cross section by the parton level cross section. Such a correction factor may only be applied if there is reasonable agreement between the hadron- and parton level quantities. Figure 4.4 shows the correlation and resolution for the hardest jet in the variables ϕ, η and $p_\perp^\star$. It can be clearly seen that the angular correlation in azimuth and polar angle is excellent. The correlation of transverse momentum is not quite as good but still sufficient for a meaningful hadronization correction. Figure 4.5 shows the correlation and resolution in the variables $x_{I\!P}$, M_{12} and $z_{I\!P}$. The resolution in $x_{I\!P}$ is excellent. The small tail is caused by the slightly different definitions of $x_{I\!P}$. A similar effect is visible for $z_{I\!P}$, though here the resolution is limited by the resolution of the dijet mass M_{12} that is strongly affected by hadronization. The correction factors for several key kinematic distributions are shown in Figure 4.6.

The unusually high hadronization correction factor at high $z_{I\!P}$ (see Figure 4.6) is clearly suspicious. A detailed study revealed a rather subtle effect: It is possible, that the hadronization of the two quarks from the hard scattering and the pomeron remnant results in just two mesons, which are then identified as the dijet system. In this case the reconstructed $z_{I\!P}$ is very close to one, while the momentum fraction carried by the gluon may take any value. This causes a migration of events, that are generated at any $z_{I\!P}$, to a $z_{I\!P}$ close to one. As this happens only rarely, the deficit of events at low $z_{I\!P}$ is barely noticeable. However, only few events are natively produced at very high $z_{I\!P}$, such that the influx of events into the highest $z_{I\!P}$-bin is a major contribution there. For this reason, the hadronization correction in the highest $z_{I\!P}$-bin cannot be deemed reliable. Nevertheless, the data cross section is still measured in this kinematic region, as only the NLO calculation is affected by the hadronization correction, not the data itself.

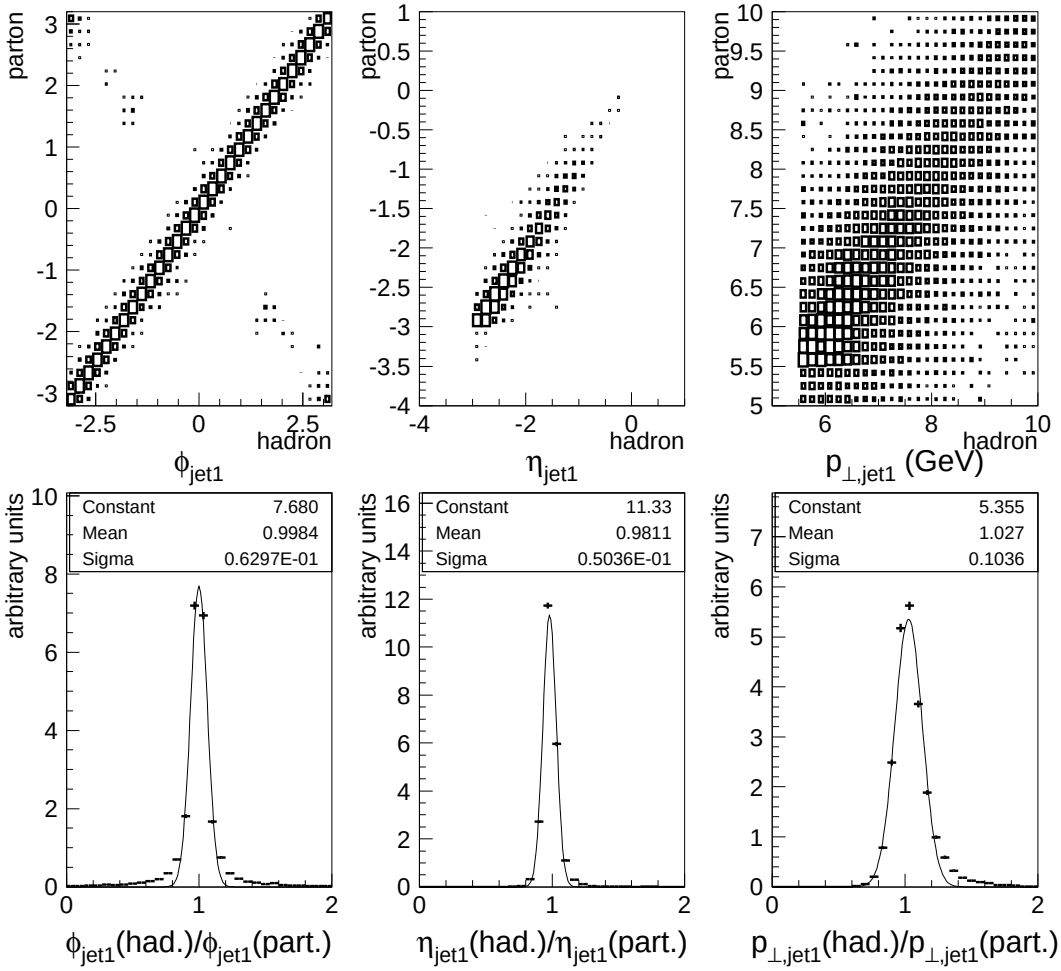

Figure 4.4: Correlation and resolution between parton and hadron quantities. Shown are the variables ϕ, η and $p_\perp^\star$ of the hardest hadron-jet. All selection cuts later used in the analysis have been applied. The values for the hardest hadron jet were compared to the parton-level jet closest in angle, not the hardest jet among the partons.

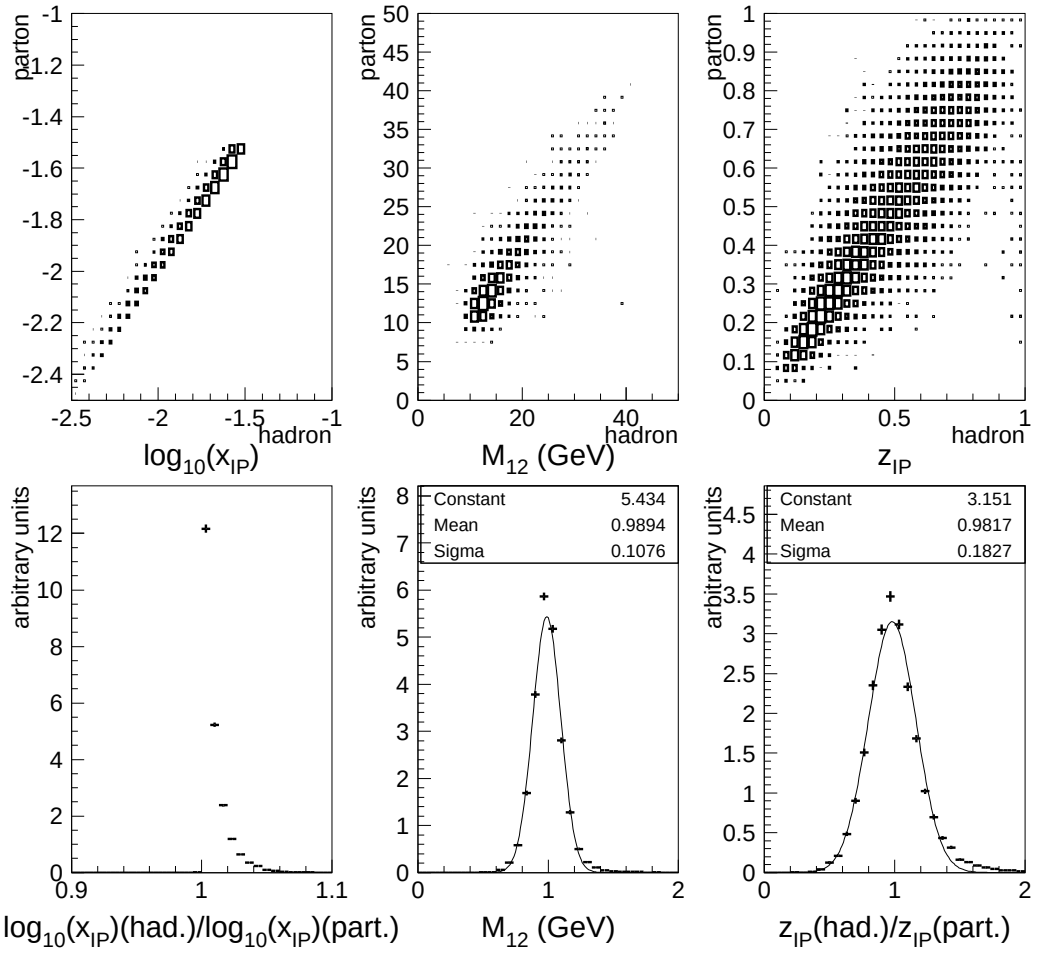

Figure 4.5: Correlation and resolution between parton and hadron quantities. Shown are the variables $x_{I\!P}$, M_{12} and $z_{I\!P}$. All selection cuts later used in the analysis have been applied.

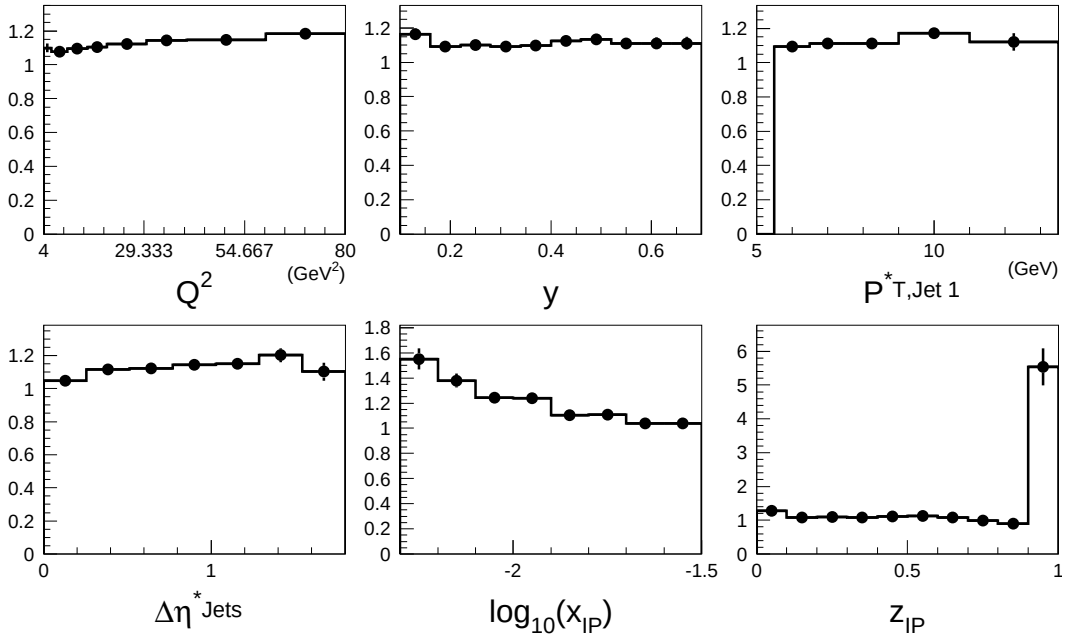

Figure 4.6: Hadronization correction factors. The unusually high factor at high $z_{I\!P}$ is discussed in more detail in the text.

Chapter 5

Data Selection

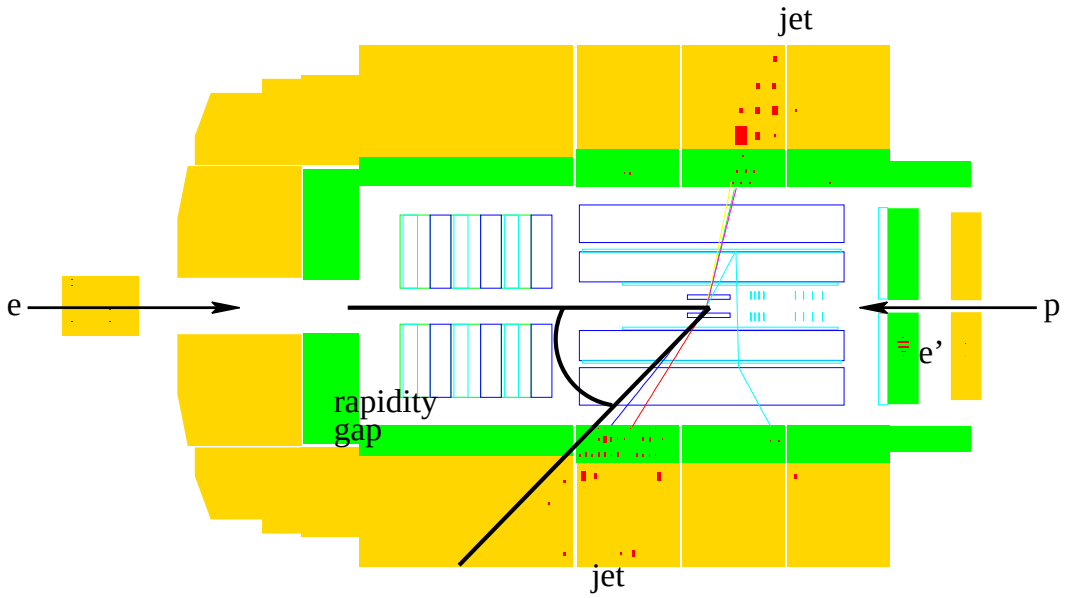

Figure 5.1: A diffractive dijet event in the H1 detector. The scattered positron can be seen in the SPACAL, while the proton leaves undetected through the beam pipe. There is no activity in the detector between the outgoing proton and the hadronic system (rapidity gap).

Figure 5.1 shows a diffractive dijet event in the H1 detector. It can be used to demonstrate the most important steps that need to be undertaken in the proper selection of events. The scattered positron is identified in the SPACAL and two or more jets in the LAr calorimeter and tracking chambers are required. The absence of hadronic activity in the forward part of the H1 detector is enforced to ensure the diffractive nature of the event. Additional steps need to be undertaken to confirm that the H1 detector was in proper operational conditions and its response is adequately described by the simulation.

5.1 Event Rate and Integrated Luminosity

The integrated luminosity for this study was measured with the sub-detector described in section 3.6. At the H1 experiment data is taken in periods called runs, over which the trigger and readout configurations remain constant. These runs can last from a few minutes to several hours. The luminosity is determined separately for each run and later summed over all runs that enter the analysis. In order to enter into this analysis the runs have to meet certain quality criteria:

- They have to be classified as "good" or "medium" quality.
- All relevant sub-detectors described above were supplied with the appropriate high voltage power.
- Information from all relevant sub-detectors was properly read out and stored.
- None of the relevant sub-detectors showed significant noise. A list of excluded runs with high noise in the forward detectors was compiled with the help of [51].
- Runs with a prescale (see section 3.5 for details) higher than two for the used subtrigger S61 are excluded.

The integrated luminosity corresponding to the selected run can then be determined, leading to the numbers shown in table 5.1.

Table 5.1: Integrated luminosity for diffractive dijets in DIS.

Year	**Run Range**	**Luminosity** $[pb^{-1}]$
1999	244968 - 262143	12.9
2000	262144 - 279215	38.6
total	**244968 - 279215**	**51.5**

Figure 5.2 shows the event yield per luminosity as a function of the integrated luminosity. The constant value of the event yield over time shows that operating conditions of the H1 detector were stable and runs with technical problems have been successfully removed.

5.2 Calibration

5.2.1 SPACAL Calibration

As many important kinematic quantities are derived from measurements of the energy and angle of the scattered positron, it is important to ensure the reliability of their determination. In this analysis only events that show a scattered positron in the SPACAL are considered. The SPACAL does not have a uniform geometric acceptance:

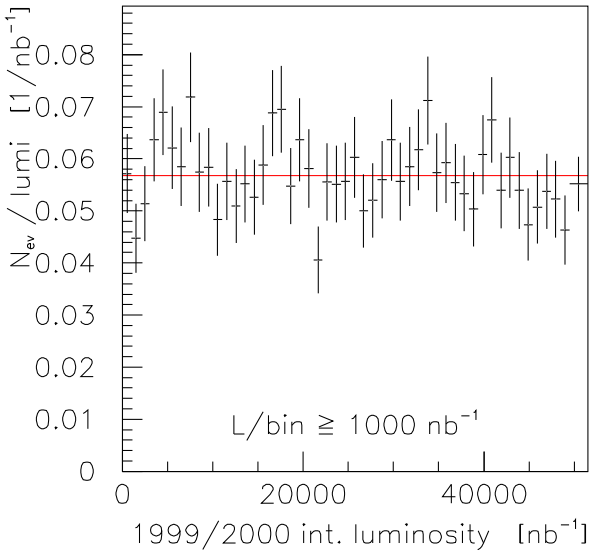

Figure 5.2: Number of diffractive dijet events per luminosity as a function of integrated luminosity. Trigger prescales are applied, but the trigger efficiency has not been corrected for. The transition from 1999 to 2000 data lies at 13,000 nb^{-1}.

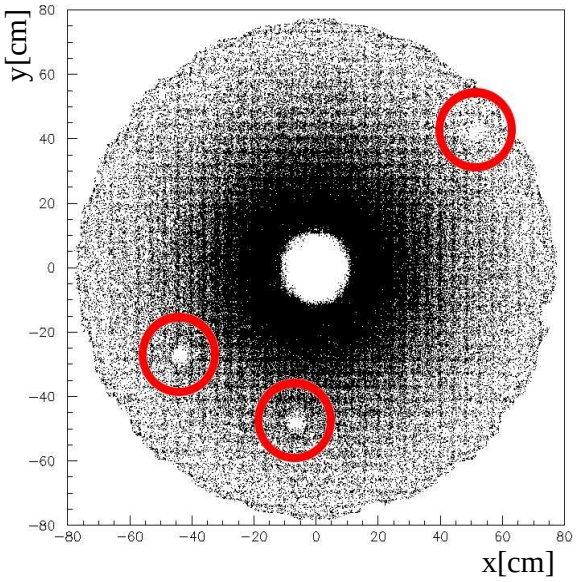

Figure 5.3: Impact positions of candidates for scattered positrons in the SPACAL relative to the beam axis for the 1999 and 2000 data taking periods. Each dot represents a positron candidate of 8 GeV energy or more. Red circles mark the dead regions.

during the 1999/2000 positron data taking period, there were some dead regions as shown in Figure 5.3. These were excluded by introducing the following fiducial cuts:

$$
\begin{aligned}
-44.55\text{ cm} < x_{\text{pos}} < -40.5\text{ cm} \quad &\text{and} \quad -28.35\text{ cm} < y_{\text{pos}} < -24.3\text{ cm}\,, \\
-8.1\text{ cm} < x_{\text{pos}} < -4.05\text{ cm} \quad &\text{and} \quad -48.6\text{ cm} < y_{\text{pos}} < -44.55\text{ cm}\,, \\
48.65\text{ cm} < x_{\text{pos}} < 52.7\text{ cm} \quad &\text{and} \quad 40.5\text{ cm} < y_{\text{pos}} < 44.55\text{ cm}\,.
\end{aligned}
$$

Here, x_{pos} and y_{pos} measure the distance of the positron candidate from the beam axis along the x- and y direction.

While the determination of the scattering angle is rather accurate, the correct measurement of the energy of the positron is much more challenging. Two methods were used to ensure its reliability.

Double Angle-Method

The absolute energy calibration of the SPACAL and its description in the simulation can be checked by comparing the reconstructed energy of identified positrons in the SPACAL to the energy derived by the double angle method. If all particles in the final state of the event are measured, then the system is over-constrained and one may choose one of several different ways do extract kinematic quantities. In this case, the energy of the outgoing positron $E_{e'}$ is calculated from the polar angle of the scattered positron $\theta_{e'}$ the polar angle of the hadronic final state γ_{had} and the initial positron energy E_e:

$$E_{e',da} = \frac{1}{\sin(\theta_{e'})} \cdot \frac{2 \cdot E_e}{\tan(\frac{\theta_{e'}}{2}) + \tan(\frac{\gamma_{had}}{2})}. \tag{5.1}$$

Similarly the inelasticity y can be reconstructed from the angles alone or the hadronic final state alone:

$$y_{da} = \frac{\tan(\frac{\gamma_{had}}{2})}{\tan(\frac{\gamma_{had}}{2}) + \tan(\frac{\theta_{e'}}{2})}, \tag{5.2}$$

$$y_{had} = \frac{(E - p_z)_{had}}{2 \cdot E_e}, \tag{5.3}$$

where the angle of the hadronic system is determined from:

$$\tan(\frac{\gamma_{had}}{2}) = \frac{(E - p_z)_{had}}{p_{\perp,had}}. \tag{5.4}$$

$(E - p_z)_{had}$ is the difference between energy and the momentum in z direction summed over all hadronic final state objects. Additionally $(E - p_z)$ is defined as $(E - p_z)_{had} + (E - p_z)_e$, where $(E - p_z)_e$ is reconstructed from the positron angle and energy as measured in the SPACAL.

The double angle method can be problematic at low positron energies and high values of the inelasticity y due to QED radiation effects and the fact that the hadronic final state may not have been completely contained in the detector, prohibiting the correct reconstruction of γ_{had}. To suppress these effects in addition to the standard selection cuts described in section 5.4.1, the following selection criteria are applied for the calibration study:

- 45 GeV$< E - p_z <$ 65 GeV to ensure event containment.

- $y_{had} < 0.3$ to remain within the applicable range of the double angle method.
- $|y_{had} - y_{da}|/(y_{had} + y_{da}) < 0.2$ to ensure a proper reconstruction of the hadronic final state.

The ratio E_{SPACAL}/E_{da} is shown for positrons of energy $E_{SPACAL} > 20$ GeV in Figure 5.4. The resulting peak at unity demonstrates that the calibration of the SPACAL

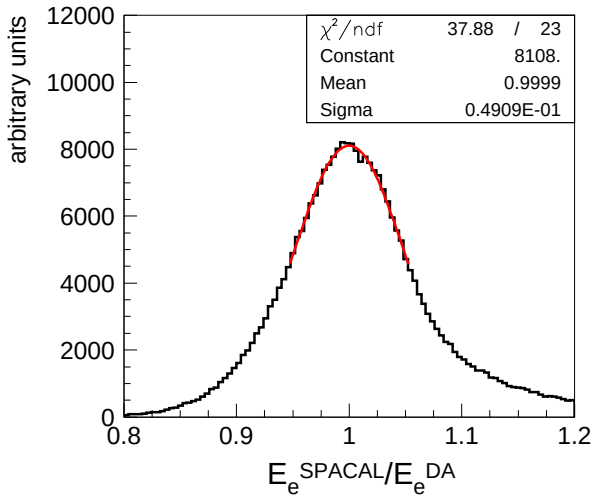

Figure 5.4: Positron calibration with the double angle method. The ratio E_{SPACAL}/E_{da} for positrons of $E_{SPACAL} > 20$ GeV shows the expected peak at unity.

calorimeter at high energies is correct. The average ratio of E_{da}/E_{SPACAL} for data and the simulation (see Figure 5.5, left and middle) is also investigated as a function of positron energy. Both data and the simulation are close to the desired value of

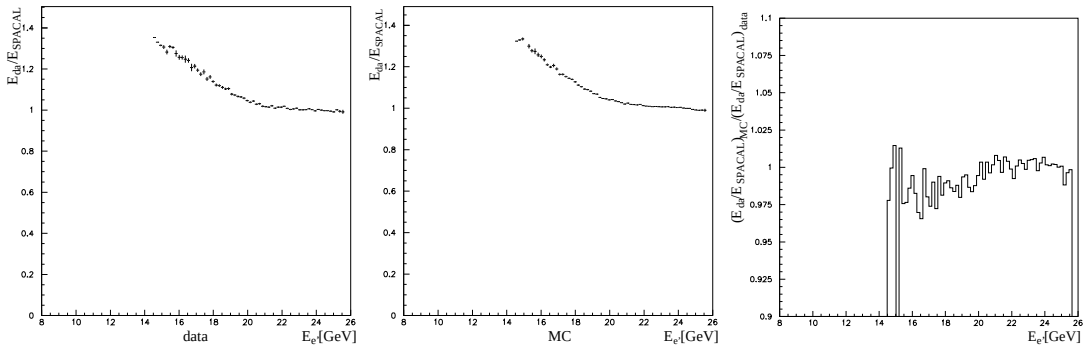

Figure 5.5: Energy dependence of the positron calibration. The ratio of positron energies determined by the SPACAL and the double angle method for data (left) and simulation (middle). The ratio of both plots is shown on the right.

unity for positron energies larger then ≈20 GeV. Below this value the effects of QED radiation are clearly visible. This can be used to check, whether the radiative effects are properly described in the simulation. The ratio of the two plots (see Figure 5.5, right) is reasonably close to unity even at quite low positron energies, confirming the validity of the simulation.

The Kinematic Peak

The energy distribution of positrons scattered into the spacal features a prominent maximum around the incoming beam energy of 27.5 GeV, the so called kinematic peak. To verify that the measured positron energy matches this expected value, a data sample was selected with a positron in the SPACAL as sole requirement. The energy distribution for this sample can be seen in Figure 5.6. The positrons used for this sample fulfill all the quality conditions required for the data, additionally events with reconstructed vertex were excluded to supress events at high inelasticity y, corresponding to low positron energies. The peak of the distribution centers around the expected 27.5 GeV, confirming the calibration of the SPACAL. As the studies of the double angle

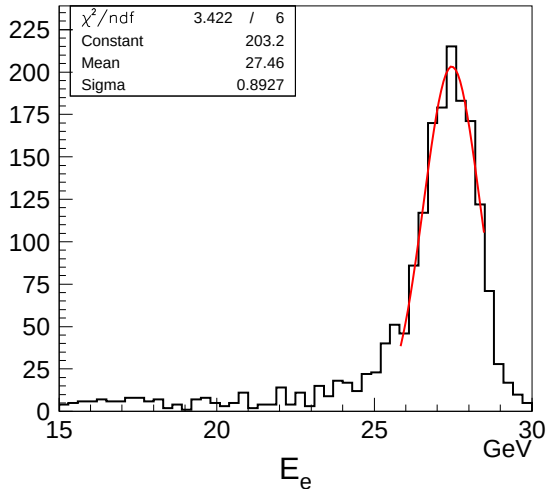

Figure 5.6: Energy distribution of positrons detected in the SPACAL. The peak of the distribution is centered at the expected value of 27.5 GeV.

method and the kinematic peak both show no indications of problems with the applied positron energy calibration, no further corrections are necessary.

5.2.2 Calibration of the LAr Calorimeter for Hadron Response

Once the reliability of the energy measurement in the SPACAL has been established, it can be used to calibrate the LAr calorimeter. For this purpose DIS events with one jet are selected, such that the balance in the transverse momentum between the positron $p_{\perp,e}$ as reconstructed from the SPACAL and the hadronic final state $p_{\perp,had}$ as reconstructed from the LAr calorimeter can be used to calibrate the LAr calorimeter. The following criteria were applied to the data sample:

- $Q^2 > 9$ GeV^2 to ensure a reasonable total $p_\perp$ in the final state.
- $E_{e'} > 20$ GeV to ensure a reliable measurement of $p_{\perp,e}$.
- Positron-quality cuts were applied as described in section 5.4.1.
- 45 GeV$< E - p_z < 65$ GeV to ensure event containment.

- The jet reconstructed from LAr clusters alone with transverse momentum $p_{\perp,jet}$ must contain the majority of the transverse momentum of the hadronic final state: $\frac{|p_{\perp,jet}-p_{\perp,had}|}{p_{\perp,jet}+p_{\perp,had}} < 0.2$. This guarantees that the majority of the transverse momentum of the hadronic final state is carried by a single jet and thus localized in η and ϕ.

If the response of the calorimeter is adequately modeled in the Monte Carlo simulation, the absolute energy scale of the LAr calorimeter has little effect on the measurement of the cross section at hadron level. Thus the agreement in the behavior of the LAr calorimeter was analyzed by studying the double ratio

$$\frac{\left(\frac{p_\perp^{hadrons}}{p_\perp^e}\right)_{data}}{\left(\frac{p_\perp^{hadrons}}{p_\perp^e}\right)_{MC}}, \tag{5.5}$$

which is studied as a function of η_{jet} (6 bins) and $p_{\perp,jet}$ (8 bins). In each of the bins a Gaussian is fitted to the distribution of the double ratio. The fit results for each bin is shown in Figure 5.7, left. The points lie within the nominal uncertainty of 4%, but there is evidently room for improvement. For each η-range a correction factor (shown

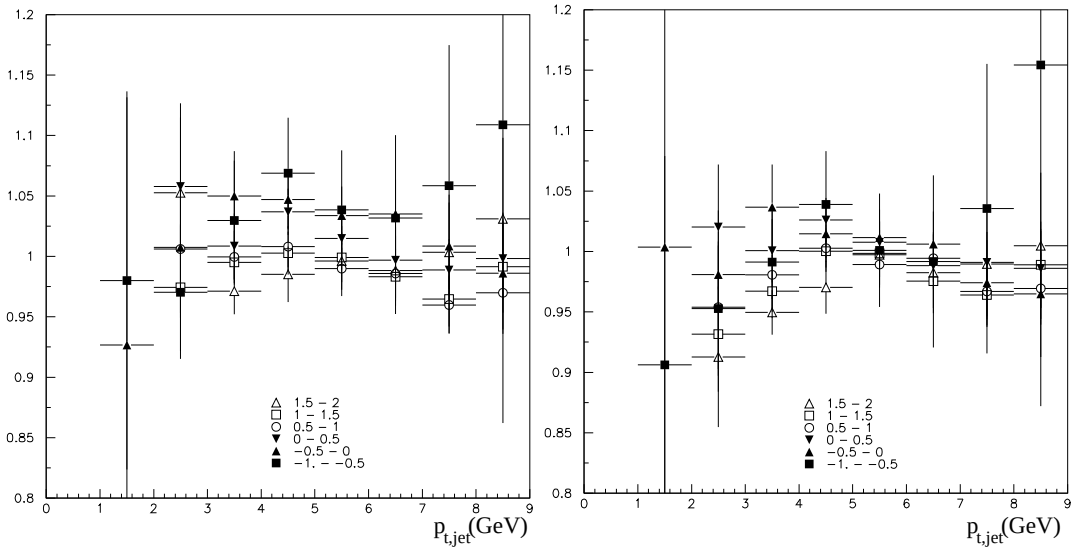

Figure 5.7: Energy calibration of the LAr calorimeter. Shown is the double ratio of equation 5.5 as a function of the transverse momentum of the dominant jet. The different symbols denote different η_{jet} ranges as denoted in the plot. The left plot shows the situation before, the right one after the calibration adjustment.

in table 5.2) is determined as the best constant fit to the $p_{\perp,jet}$ dependent double ratio in the range 3-9 GeV (3-8 GeV for the most backward η_{jet} bin). The factors for the three most forward η_{jet} bins do not differ significantly from one.

These correction factors are then applied in the data to the energies of all LAr calorimeter clusters in the appropriate η-ranges, which results in the right plot of Figure 5.7. In the $p_{\perp,jet}$ region above 4 GeV the double ratio is now closer to one and shows less scatter among the different η-ranges than without the correction.

Table 5.2: Correction factors for the LAr calorimeter calibration.

η-range	correction factor
-1.0 - -0.5	1.053
-0.5 - 0.0	1.037
0.0 - 0.5	1.018
0.5 - 1.0	0.994
1.0 - 1.5	1.000
1.5 - 2.0	0.999

In the final analysis jets are not reconstructed from LAr calorimeter clusters alone but from the improved calorimeter clusters combined with tracking information to gain the best possible measurement for the resulting jets (see [52] for details). In this method tracking information is used at low momenta and calorimeter information at high momenta while avoiding double counting. The result is called combined object. In the case of of low jet energies, as for this study, the track and calorimeter information contribute about equally (as can be seen in Figure 5.20), such that the improved calibration has a reduced impact on final jet energies.

5.3 Reconstruction of Kinematic Variables

The kinematic variables Q^2, y and W, defined in section 2.1.1 are reconstructed from measurements of the scattered positron energy $E_{e'}$ and angle θ_e only:

$$y = 1 - \frac{E_{e'}}{E_e} \sin^2(\frac{\theta_e}{2}), \tag{5.6}$$

$$Q^2 = 4E_{e'}E_e \cos^2(\frac{\theta_e}{2}), \tag{5.7}$$

$$W^2 = ys - Q^2. \tag{5.8}$$

Due to the high precision in the measurement of the positron angle and energy this method yields the most precise values for these variables. However, it is important to note that the electron method is prone to errors due to QED radiation (as discussed in section 4.1.1).

The hadronic final state is measured with the central tracking system and the LAr calorimeter. The information of both detector components are combined avoiding double counting to achieve the best possible precision (see [52] for details). As the scattered proton (i.e. the Y system), is leaving the detector through the beam pipe and is separated from the X system by a gap in rapidity, all activity in the main detector can be attributed to the X system. The sum of the four vectors of all these combined objects p_X can be used to calculate the invariant mass M_X of the X system. This can then be used to evaluate the longitudinal momentum fraction $x_{I\!P}$ that the pomeron

carries of the proton:

$$M_X = \sqrt{p_X^2}, \tag{5.9}$$

$$x_{I\!P} = \frac{Q^2 + M_X^2}{Q^2 + W^2}. \tag{5.10}$$

The momentum fraction that the parton entering the hard interaction takes in the pomeron $z_{I\!P}$ is reconstructed from Q^2, M_X and the invariant mass of the dijet system M_{12}:

$$z_{I\!P} = \frac{Q^2 + M_{12}^2}{Q^2 + M_X^2}. \tag{5.11}$$

Of importance for the selection is also the variable η_{max}, which denotes the pseudorapidity of the most forward LAr cluster with an energy above a noise threshold of 400 MeV, where the pseudorapidity η is measured as:

$$\eta = -\ln\left(\tan\frac{\theta}{2}\right), \tag{5.12}$$

θ being the polar angle of the corresponding particle.

5.4 DIS- and Jet Selection

The identification of dijet events in diffractive DIS is based on three main criteria: the existence of jets in the hadronic final state, the measurement of the scattered positron, indicating a high momentum transfer Q^2 and the absence of a high mass proton dissociation system, indicating diffractive scattering. The selection of jet events in DIS follows the standard procedure at H1 [53].

The selection starts already during data-taking by the setup of an appropriate trigger (see 3.5 for details on the H1 trigger system). For this study the sub-trigger S61 was used, it is a combination of the following requirements:

- an energy deposit in the SPACAL (the positron candidate),
- an preliminarily reconstructed event vertex,
- a track of high transverse momentum (at least 800 MeV) in the main jet chambers (indicating a jet).

The energy in the SPACAL has to be localized in a block of four adjacent calorimeter cells, exceed 6 GeV and arrive within a time window of 20 ns. Additionally the sub-trigger S61 also requires several indicators of background related events to be absent (mostly related to the timing structure of the event relative to the bunch crossing). However, the sample selected with this trigger still contains a large number of background events that need to be discarded by a more sophisticated analysis, which will be discussed in the following.

5.4.1 Positron Identification

The scattered positron is identified in the SPACAL mainly by shower shape. Electromagnetic showers have smaller radii and are shorter than their hadronic counterparts, thus the positron candidate is restricted to

$$r_{cluster} < 3.5 \text{ cm}. \tag{5.13}$$

For this search fiducial cuts are applied to exclude areas that are not well described in the simulation (see section 5.2.1) or are close to the edge of the SPACAL and thus may not contain the whole shower. This is achieved by a cut on the polar angle of the positron candidate

$$156^\circ < \theta_{e'} < 176^\circ \tag{5.14}$$

and the requirement of a minimum distance of the cluster to the beam-axis

$$d_{cluster-beam} > 9 \text{ cm}. \tag{5.15}$$

Similarly to avoid leakage of energy into the beampipe, the energy in the innermost layer of the SPACAL (the so called veto-layer) E_{veto} must be lower than 1 GeV. Additionally the requirement on the cluster energy is tightened to 8 GeV to achieve a high trigger efficiency and low photoproduction background. Additionally several cuts are applied that serve to suppress different backgrounds. An event vertex has to be reconstructed within 35 cm (in z-direction) from the nominal interaction point:

$$|z_{vtx}| < 35 \text{ cm}. \tag{5.16}$$

This reduces the background by beam-gas interactions. The misidentification of an isolated hadron (mostly pions) as positron can be suppressed by the different shower-shapes of electromagnetic and hadronic showers. In particular hadronic showers tend to be much more extended than electromagnetic ones, so background from hadrons can be reduced by requiring the backward (hadronic) layer behind the positron candidate to contain only negligible energy:

$$E_{had} < 0.5 \text{ GeV}. \tag{5.17}$$

To reduce the background due to initial state radiation and photoproduction a cut on $E - p_z > 35$ GeV is introduced. The kinematic variable y is restricted to the range $0.1 < y < 0.7$, to minimize the influence of final state QED radiation. The upper limit of the y cut also coincides with the 8 GeV energy requirement for the positron. This cut also serves to give the measured cross section a concise definition independent of detector acceptance. Similarly a restriction of $4 < Q^2 < 80$ GeV^2 is imposed to translate the SPACAL acceptance into independent kinematical quantities. These selection criteria are summarized in table 5.3.

The Monte Carlo simulation used to correct the data for detector effects has some flaws that need to be corrected before any correction factors can be extracted. In particular the radius of the positron cluster in the SPACAL is typically reconstructed 1.8 mm too large. This is corrected, by subtracting 1.8 mm from the simulated cluster size. The distribution of the the collision vertex in z-direction is slightly shifted and

Table 5.3: Positron identification and DIS cuts.

Quantity	Cut Value	Reason
y	$0.1 - 0.7$	containment, QED radiation
Q^2	$4 - 80$ GeV^2	SPACAL acceptance
θ_e	$156° - 176°$	SPACAL acceptance
$E_{e'}$	>8 GeV	avoid trigger limit and γp bgr.
$\lvert z_{vtx}\rvert$	<35 cm	veto beam/gas, beam pipe bgr.
$E - p_z$	>35 GeV	γp and ISR background
distance cluster-beam pipe	>9 cm	high bgr. in inner SPACAL
electron cluster radius	<3.5 cm	electron misidentification
had. energy behind electron	<0.5 GeV	electron misidentification
energy in SPACAL veto layer	<1.0 GeV	avoid leakage out of SPACAL
SPACAL fiducial cuts	–	avoid dead SPACAL cells

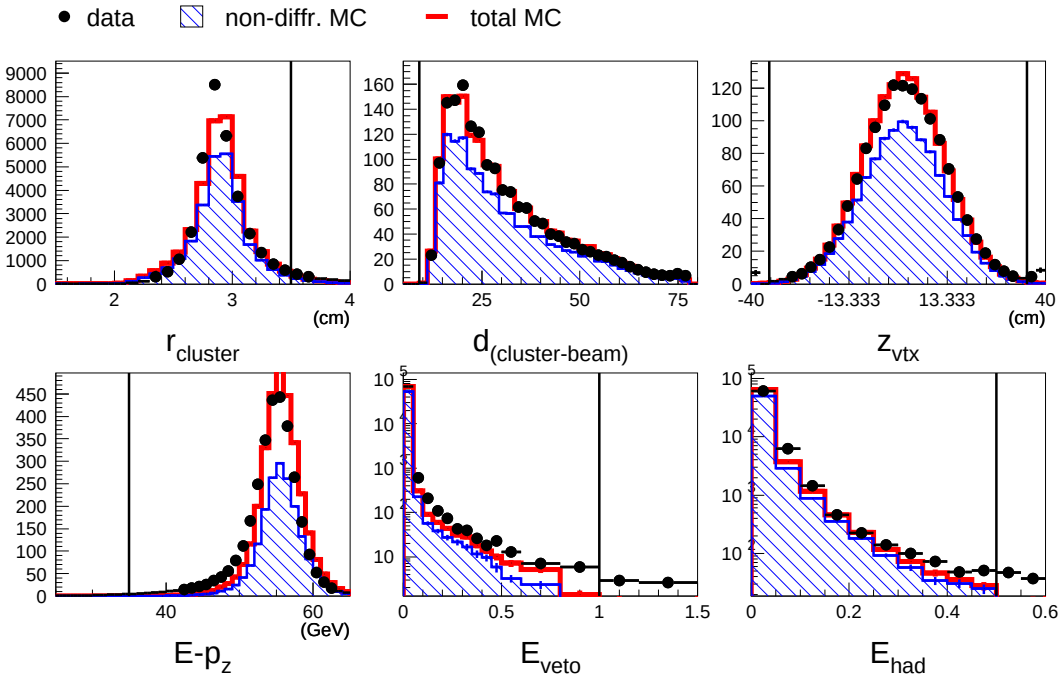

Figure 5.8: The distributions of the positron identification criteria as given in table 5.3. The cuts are marked by the black lines, the only cuts not applied to this sample are the diffractive cuts discussed below and the cut on each variable shown. The units on the y-axis of the plot are arbitrary.

somewhat narrower in the simulation compared to the data. This effect is corrected by weighting the simulated events with the ratio of two Gaussians, which were fitted to the data and simulation respectively.

Figure 5.8 shows a comparison between the shapes of the data and the Monte Carlo simulation for the cuts that select the scattered positron. The non-diffractive background

simulation (see section 4.1.2) is shown in blue, while the red line represents the sum of the signal (see section 4.1.1) and the background. The Monte Carlo simulation is normalized to the data. Background that is rejected is generally very small and well modeled by the simulation. The distribution of $E - p_z$ is slightly skewed between data and simulation. This is caused by the absence of QED radiation effects in the background simulation, a problem that will be discussed in more detail below.

5.4.2 Jet Criteria

The combined objects in the hadronic final state are grouped into jets by the inclusive $k_\perp$ algorithm [54, 55]. This algorithm has been chosen for its collinear and infrared safety. If the dijet cross sections are to be compared with a NLO QCD calculation, it is necessary to use the same jet algorithm also to determine the observables in the calculation. However, NLO QCD calculations typically show divergences when a very soft gluon is radiated in the final state (infrared divergence) or one of the final state partons splits into two nearly collinear partons (collinear divergence). These divergences cancel, if the physical observables are calculated from the emerging partonic final state with a jet algorithm that is infrared- and collinear safe. The formerly popular cone algorithm (see for example [56] for a description) does not have these features and is therefor not used in the comparison to NLO QCD calculations.

For this study an inclusive $k_\perp$ algorithm with distance parameter 1 (as described in [54, 55]) is used to group the particles of the final states into jets. The algorithm is applied to the combined objects introduced in section 5.2.2 after boosting them into the $\gamma^\star$p rest frame.

Jet Selection

The jets found in this manner are ordered in their transverse momentum $p_\perp^\star$ in the $\gamma^\star$p rest frame, where $p_{\perp,jet1}^\star$ denotes the hardest jet. Before any further cuts are applied any events that contain only one or no jet are rejected.

In order to achieve high precision in the measurement of the jet properties it is necessary to restrict the analysis to jets that lie within the main part of the detector. For this reason the jets are required to have pseudorapidities that make them impact and contained in the LAr calorimeter:

$$2 > \eta_{jet,lab} > -1. \tag{5.18}$$

To allow comparison to previous analyses (i.e. [13]), the definition of the cross section at hadron level is slightly different. At hadron level the pseudorapidity of the jets is constrained in the $\gamma^\star$p rest frame to a range that corresponds to the above stated range in the laboratory system:

$$0 > \eta_{jet,\gamma^\star \mathrm{p}} > -3. \tag{5.19}$$

Additionally the jets are required to have a minimum transverse momentum in the $\gamma^\star$p system. This is needed to provide a hard scale for the successful application of perturbative QCD and also avoids the low resolution that accompanies the measurement

of low $p_\perp$ jets:

$$p^\star_{\perp,jet1} > 5.5 \text{ GeV} \tag{5.20}$$
$$p^\star_{\perp,jet2} > 4.0 \text{ GeV} \tag{5.21}$$

The cuts on the jets are chosen to be asymmetric in order to avoid problems that can appear in NLO QCD calculations, which can be numerically unstable due to crossing symmetries otherwise. These restrictions are summarized in table 5.4.2. Figure 5.9

Table 5.4: Summary of the jet selection cuts. The cut to the transverse momenta is applied in the $\gamma^\star$p rest frame. The jets are identified with the inclusive $k_\perp$jet algorithm with a distance parameter of 1.0.

Quantity	Cut Value
N_{jet}	$\geq$2
$p^\star_{\perp,jet1}$	>5.5 GeV
$p^\star_{\perp,jet2}$	>4.0 GeV
$\eta^{lab}_{jet(1,2)}$	-1.0−2.0

shows a comparison between data and the Monte Carlo simulation where all analysis cuts except the diffractive selection have been applied. In general the description is excellent, however there are significant deviations in the y- and $\langle\eta\rangle$-spectrum. The

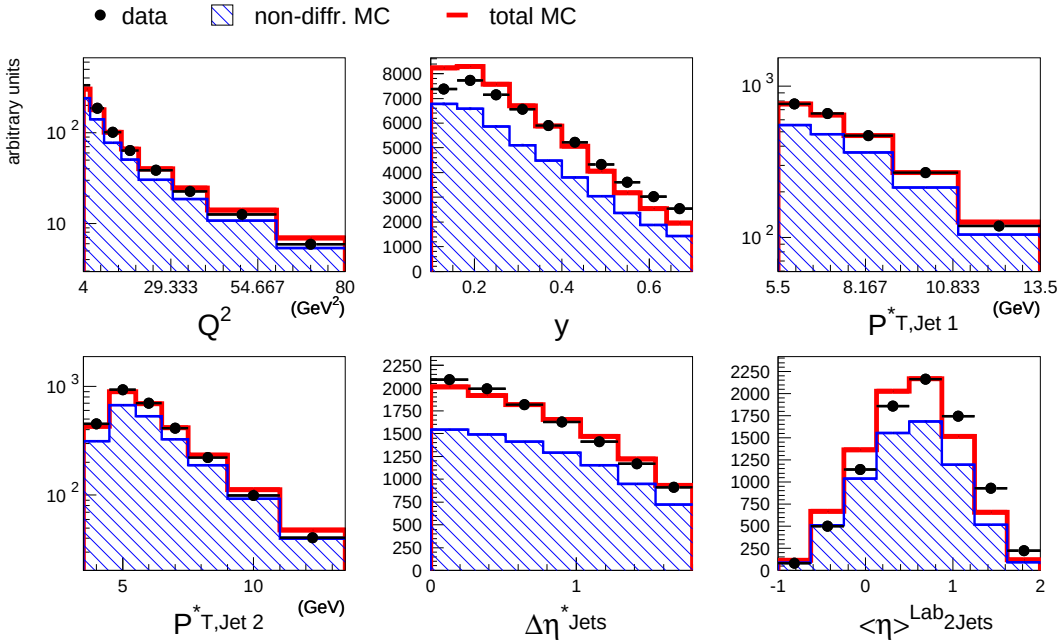

Figure 5.9: Control plots for the inclusive dijet sample. All cuts except the diffractive selection have been applied. The simulation is normalized to the data.

discrepancy in $\langle\eta\rangle$ has also been observed in other studies of jets in DIS [53]. However,

its exact origin is uncertain; unordered gluon radiation which is not included in the DGLAP evolution equations may play a role. This difference in y is caused by the absence of QED radiation in the background simulation (blue). If a simulation is used, that includes radiative effects, the y-shape is well reproduced (see Figure 5.10). For this purpose a Monte Carlo simulation was used that was originally generated for an analysis of forward jets in DIS [53]. The sample was generated with the `DJANGOH` program [57] and is described in detail in [53]. Due to technical difficulties, this Monte Carlo sample cannot be easily split into diffractive and non-diffractive contributions, so that it cannot be used to subtract the non-diffractive background. Instead merging the non-diffractive component of this sample with the signal simulation, no cuts are applied in M_Y and $x_{I\!P}$ and the complete sample is used to compare to the inclusive data set (i.e. without diffractive cuts). It nevertheless shows that the data are in accord with the simulation. The difference between the two background simulations will be covered in the systematic uncertainty concerning the background subtraction.

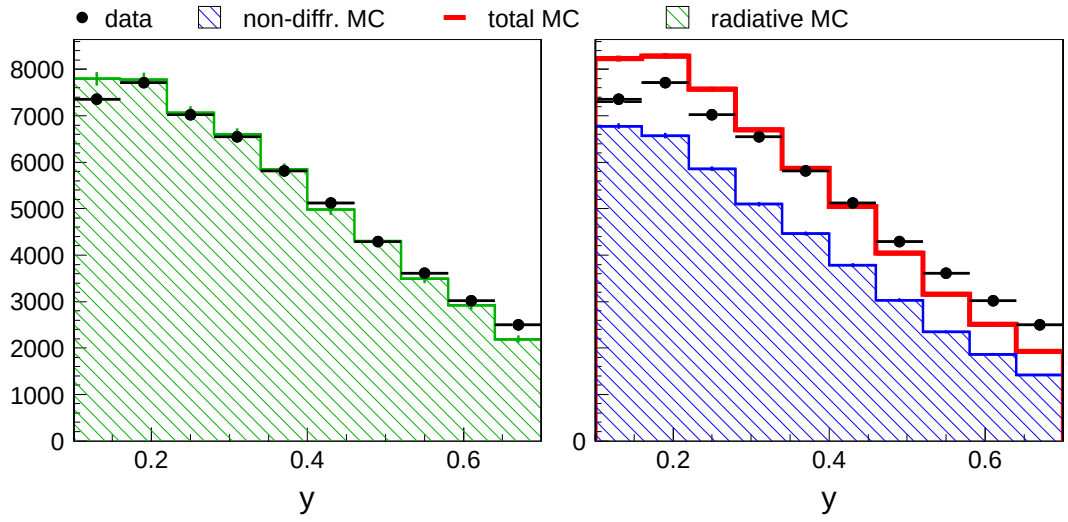

Figure 5.10: Effects of QED radiation on the y distribution. The y spectrum of the inclusive dijet sample (black points) is compared to a Monte Carlo model including QED radiation (left) and the non-radiative model otherwise used in this study (right). The simulation is normalized to the data.

5.5 Diffractive Selection

Ideally one would like to detect the scattered proton, that is characteristic for diffractive events. However, this is a formidable technical challenge, as the scattered proton typically has very low transverse momentum and thus travels very close to the outgoing proton beam. During the data taking period of 1999 and 2000 the H1 detector included a sub-detector to measure the properties of scattered protons. Unfortunately its geometrical acceptance was too small to make a precise measurement of dijets in diffractive DIS possible [58]. In this analysis the large rapidity gap method [12, 13] is used instead. In this approach a large range in rapidity between the outgoing proton and the central

hadronic system is required to be devoid of activity. This is achieved by looking for activity in the very forward region of the LAr calorimeter and the forward detectors discussed in section 3.4.

The pseudorapidity of the most forward LAr calorimeter cluster above noise threshold (400 MeV) η_{max} is required to be smaller then 3.2. The first two layers of the FMD must not contain more than one hit in total. The third layer of the FMD is allowed to contain up to one hit as well. The PRT scintillator-panels 1 to 5 and FTS panels 8 to 15 are required to be devoid of any activity at all. These cuts restrict the selected events to pomeron momentum fraction of roughly $x_{I\!P} \lesssim 0.03$. To provide a clean cross section definition and further suppress non-diffractive background a cut of $x_{I\!P} < 0.03$ is furthermore imposed. The above cuts are summarized in table 5.5.

Table 5.5: Diffractive selection cuts.

Quantity	**Cut Value**
$x_{I\!P}$	<0.03
η_{max}	<3.2
FMD-hits (layer 1 and 2 together)	≤ 1
FMD-hits (layer 3)	≤ 1
PRT-hits (layers 1-5 together)	$=0$
FTS-hits (panels 8-15)	$=0$

These cuts cannot guarantee elastic scattering of the proton, however, as shown in [59], they roughly correspond to a restriction of the mass of the proton dissociation system to $M_Y < 1.6$ GeV and $|t| < 1$ GeV^2. To estimate the migrations over the mass threshold, it is important to understand the response and efficiency of all involved detectors. The cross section at hadron level is restricted to this phase space and a Monte Carlo simulation is used to extrapolate the results from the rapidity gap selection into this kinematic range of diffraction.

The simulation is complicated by the large amount of dead material between the interaction point and the actual detectors, leading to secondary interactions that are hard to model. The other problem arises due to the uncertainty of the model simulations in kinematic regions that are difficult to access experimentally. Of particular interest here are events that are diffractive (i.e. have an elastically scattered proton), but also cause activity in the forward detectors. Unfortunately the reliability of this model has been tested only within rather wide margins of error with a sample for which the elastically scattered proton was actually detected, leading to rather large errors due to the extrapolation.

The simulation of the response of the proton remnant tagger is complicated by the large amount of material which a particle has to pass before it reaches the scintillator panels. Accordingly, the measurements of the detection efficiency for dissociated protons (determined by detecting the proton remnant in the forward LAr calorimeter) is not well described by the Monte Carlo Simulation. The efficiencies of the individual panels in the simulation were adjusted following a scheme developed for the analysis of diffractive meson production [60]. This approach proves successful not by simply adjusting the

individual panel efficiencies but instead by fixing the pairwise correlations between panels.

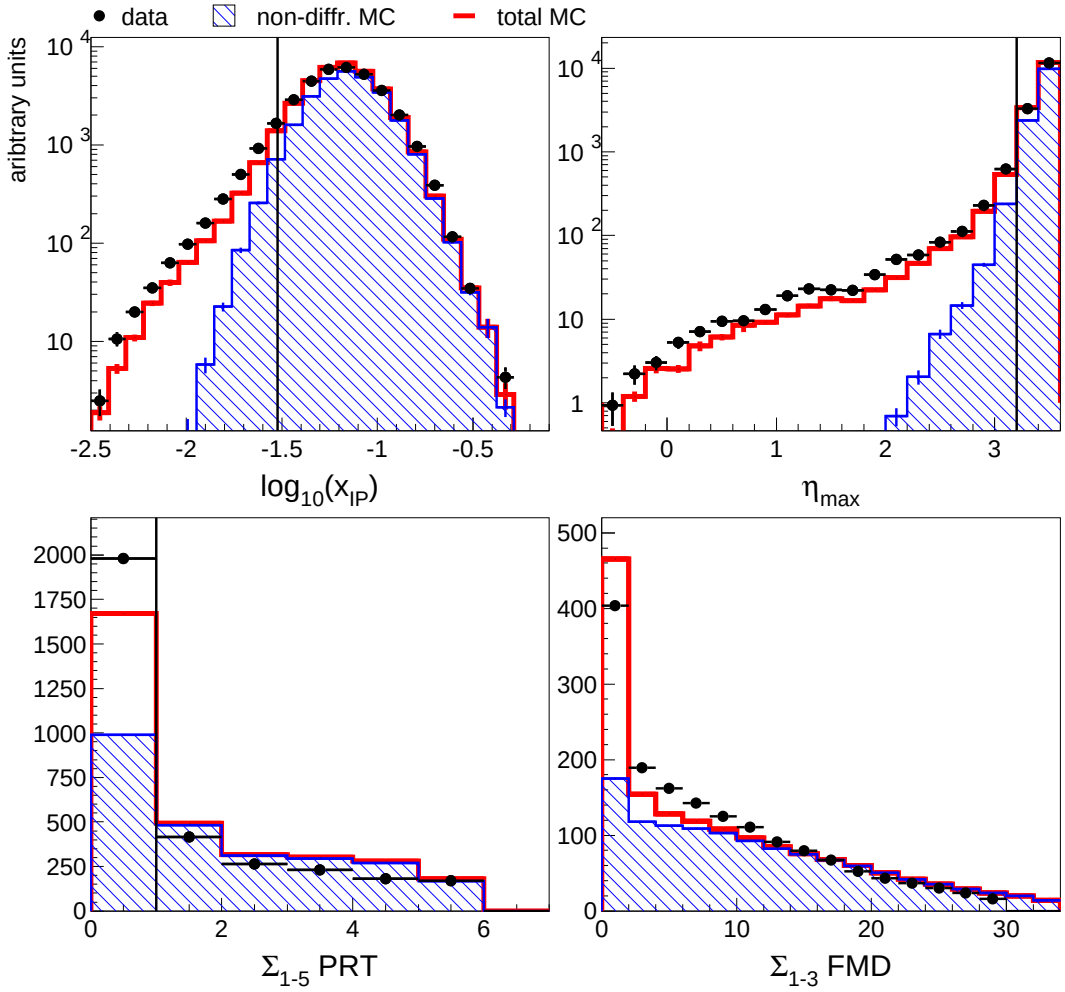

Figure 5.11: Control plots for diffractive quantities. Data are the black points, the hatched area denotes in inclusive background simulation and the line the total simulation. The black vertical lines indicate the selection cuts summarized in table 5.5.

Figure 5.11 shows the distributions of the most important cut quantities of the diffractive selection. The relative normalization of the diffractive and non-diffractive samples are determined by a fit to the η_{max}-distribution. Relative to the signal simulation, the non-diffractive background simulation is increased by a factor of 1.4. The overall agreement between data and simulation is reasonable. The remaining differences in the FMD-hit spectrum are caused by noise in the data and low mass proton dissociation, which are not simulated. The correction of this effect is discussed in section 5.6.4. The events remaining after this diffractive cut constitute the final sample of this analysis which contains 2723 events. The data sample is therefore about seven times larger than the one used in the last analysis of diffractive dijets by the H1 experiment [13]. This large improvement can be attributed to the increased integrated luminosity and the widened range in y.

5.6 Correction of Detector Effects

Even under optimal running conditions, there are still noise and other detector imperfections that degrade the measurement and need to be corrected for. In this analysis a bin-by-bin correction scheme is chosen for most of the correction factors. The actual cross section at the level of stable hadrons in a bin i of width Δ_i is computed as:

$$\sigma_i^{had} = \frac{N_i^{data}/\epsilon_i^{trigger} - N_i^{background}}{\Delta_i \cdot \mathcal{L} \cdot C_i^{QED}} \cdot C_{FMD} \cdot C_{pdiss} \cdot C_i^{detector}. \tag{5.22}$$

Here N_i^{data} is the actual number of events measured in bin i and $N_i^{background}$ is the background estimated from simulations. $\mathcal{L}$ denotes the integrated luminosity as described in section 3.6 and $\epsilon_i^{trigger}$ the efficiency of the used trigger as detailed below (section 5.6.3). C_{FMD}, C_{pdiss}, C_i^{QED} and $C_i^{detector}$ are correction factors for the noise in the FMD, M_Y- and $|t|$-migration of proton dissociative events, QED radiative effects and the transition between detector level quantities and the hadron level respectively and will be described in more detail below. Factors carrying a subscript i are determined for each bin separately, while the other factors are applied globally.

5.6.1 Correction for Proton Dissociation

As the forward detector selection cannot guarantee an elastically scattered proton but only a low mass dissociative system, the cross section definition for this study was chosen also to include events with $M_Y < 1.6$ GeV $\wedge$ $|t| < 1$ GeV^2. As M_Y and $|t|$ cannot be directly measured, it has to be estimated how many events outside of the cross section definition are not rejected by the forward detectors, and likewise how many events that fulfill the definition are not accepted.

Intensive studies of the tagging efficiencies of the forward detectors were presented in [59]. Following the method of this study, the correction for migrations of events over the threshold of $M_Y < 1.6$ GeV $\wedge$ $|t| < 1$ GeV^2 is obtained by:

$$C_{pdiss} = 1 + \frac{N_{gen}^{diss}(M_Y < 1.6 \text{ GeV} \wedge |t| < 1 \text{ GeV}^2) - N_{rec}^{diss}}{N_{gen}^{diss}(M_Y < 1.6 \text{ GeV} \wedge |t| < 1 \text{ GeV}^2) + R \cdot N_{gen}^{ela}(|t| < 1 \text{ GeV}^2)}, \tag{5.23}$$

where $N_{gen/rec}^{diss}$ denotes the number of proton dissociative events that are generated and reconstructed respectively. Analogously N_{gen}^{ela} represents the generated number of elastic events. R denotes the relative normalization of elastic and dissociative cross sections and is set to 1, a value compatible with the results presented in [12, 37]. As the main signal simulation only contains events with elastically scattered protons, a dedicated simulation for the study of proton dissociation is necessary. In this study the `DFFVM` program was used as described in section 4.1.2. The correction factor thus obtained is:

$$C_{pdiss} = 0.99 \pm 0.03(\text{syst.}). \tag{5.24}$$

The estimation of the systematic uncertainty is determined by varying:

- the ratio R of elastic to dissociative cross sections between 0.5 and 2,

- the shape of the generated M_Y distribution by $M_Y^{\pm 0.3}$,
- the shape of the generated $|t|$ spectrum by $e^{\pm 1 \cdot |t|}$ (dissociation) and $e^{\pm 2 \cdot |t|}$ (elastic).

C_{pdiss} covers only the migrations of proton dissociative events over the M_Y and $|t|$ cuts. The migrations of the proton elastic events over the $|t|$ threshold is properly simulated in the signal Monte Carlo sample and therefore absorbed into $C_i^{detector}$.

The reliability of this approach was tested by the study of a newly improved version of RAPGAP that includes the proton dissociation similar to DIFFVM. With such a model the correction factor C_{pdiss} can be simply determined as the factor of migration as observed in the improved Monte Carlo sample. A small sample was generated to check the consistency of the correction factor C_{pdiss} between the determination from the two different models and to look for any kinematic dependence of C_{pdiss}. A dependence of C_{pdiss} on any kinematic variable would necessitate a deeper study of proton dissociation with the improved RAPGAP, as DIFFVM can only be used to determine global correction factors. The results are shown in Figure 5.12 as a function of $x_{I\!P}$ and $z_{I\!P}$, the two

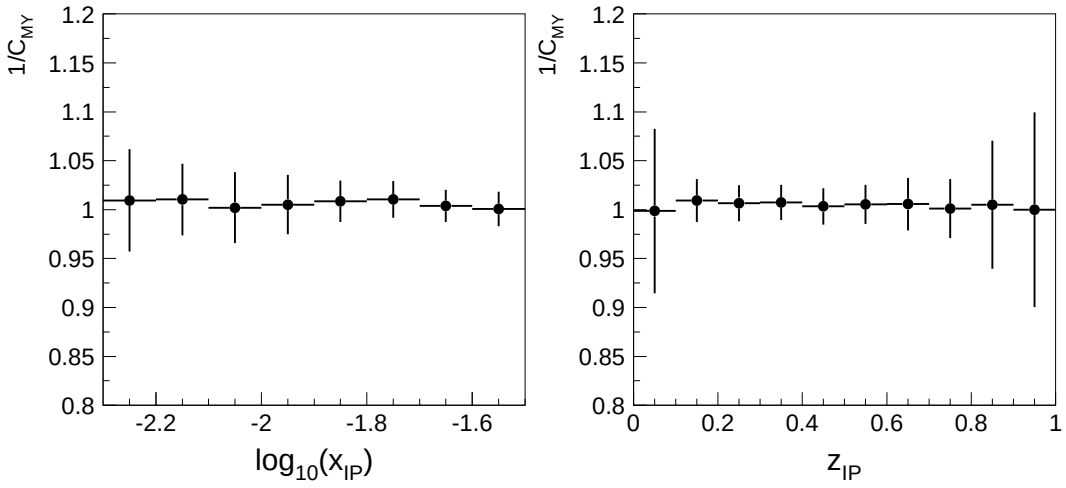

Figure 5.12: The M_Y and $|t|$ migration correction as determined from the RAPGAP Monte Carlo model including proton dissociation. Shown is the inverse of the correction factor C_{pdiss} as a function of $x_{I\!P}$ (left) and $z_{I\!P}$ (right). Both distributions show no kinematic dependence and are compatible in their absolute value to the factor determined from DIFFVM. Only statistical uncertainties are shown.

variables on which C_{pdiss} would most likely depend. However no such dependence is visible, warranting the application of a global correction factor to the data. Additionally it can be seen that RAPGAP and DIFFVM agree in the value C_{pdiss}.

5.6.2 Rapidity Gap Selection Inefficiency

The rapidity gap method to identify diffractive events is not ideal. In particular at high $x_{I\!P}$ it is not entirely unlikely that parts of the pomeron remnant have enough forward momentum to cause activity in the sub-detectors used to identify the rapidity gap, thus falsely tagging this event as non diffractive. The fraction of events lost due to this is

accounted for in the correction factor to hadron level, derived from the signal simulation. However, the accuracy of the Monte Carlo model in describing the forward energy flow of diffractive events needs to be tested for the correction factor to be trustworthy. To study the forward energy flow in diffraction a rapidity gap selection is clearly unsuitable, instead it is necessary to detect the elastically scattered proton. Such a measurement was performed at H1 [58], showing that the forward energy flow and thus the rapidity gap selection inefficiency is correctly described by the RAPGAP Monte Carlo model within the statistical errors of the measurement.

5.6.3 Trigger Efficiency

As has been described in section 3.5, events in the H1 detector are preselected by a complex trigger system. The need to strongly limit the rate of permanently stored events inevitably leads to the loss of some signal events. The cross section needs to be corrected for these losses. Typically the correction factors can be extracted from the data itself. However this approach runs into problems in this study due to the limited statistical power of the data. Instead the correction factors are determined from the signal simulation also used to correct for other detector effects (see section 4.1.1) after validation by the data.

Trigger Efficiency in the Data

The trigger consists of the combination of several trigger elements, whose efficiency can be separately determined. The total trigger efficiency is determined by the appropriate combination of the separate sub-efficiencies. The efficiencies of separate trigger elements can be measured with the help of control triggers. They should have been active in a sizeable sample of the desired data events and must not contain the trigger element under investigation. The efficiency of the trigger element is then the ratio of the selected events with active control trigger and active trigger element and all selected events with active control trigger. To check the efficiency of the SPACAL element of the subtrigger S61, the subtrigger S77 was used which relies mainly on the LAr calorimeter. The vertex and track requirements were monitored with the subtrigger S0 which depends almost entirely on SPACAL information.

The rather low statistical precision of this method originates from the rather small sample of diffractive dijet events that were selected by the control triggers. All available control triggers have either high pre-scale factors or are not ideally suited to select diffractive dijet events in DIS.

Trigger Efficiency in the Monte Carlo Model

In the Monte Carlo model the control trigger is not required. The efficiency of each trigger element can be determined by simple taking the ratio of the selected events with the trigger element active and all selected events.

It turns out, that the trigger efficiency in the Monte Carlo model is higher by 3% compared to the one determined from the data. This effect can be traced to several veto elements, which are not adequately simulated. In the determination of the trigger efficiency from the simulation these veto elements are neglected, which is equivalent to

treating them as having 100% efficiency. The losses of signal events due to these veto elements are corrected by scaling the efficiency in the model by a constant factor of 3%.

Figure 5.13 shows the comparison of the trigger efficiencies as determined from data and the Monte Carlo model for various kinematic variables. Generally a good agreement is observed well within the statistical uncertainties.

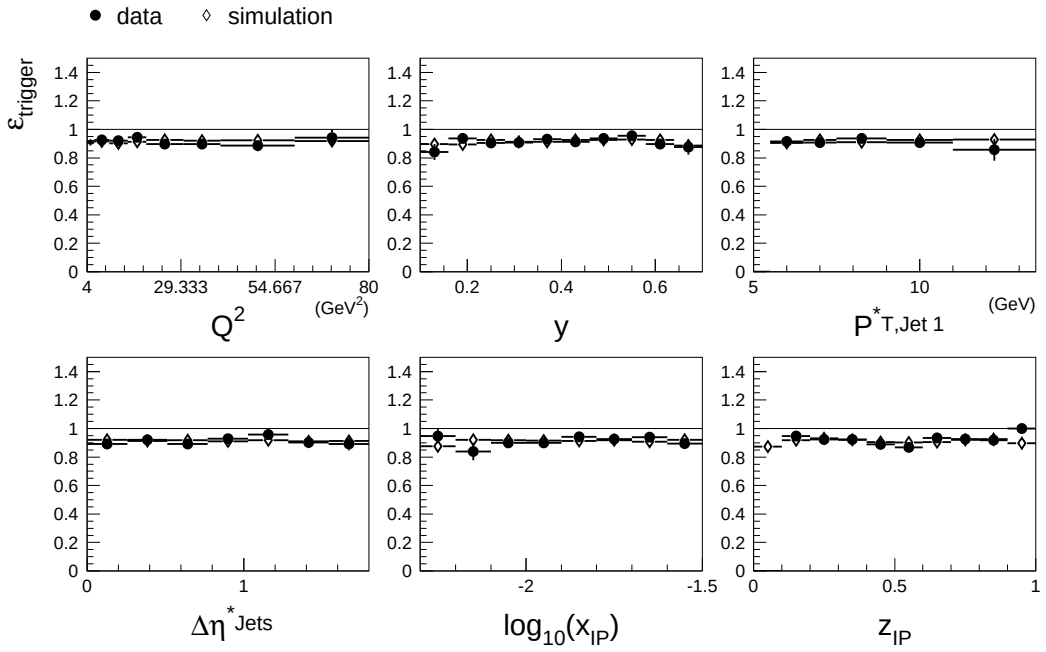

Figure 5.13: Trigger efficiency as determined from data and simulation (scaled as discussed in the text). The trigger efficiency $\epsilon_{trigger}$ is shown as a function of several kinematic variables. For the data (filled symbols) only statistical uncertainties are shown. Errors for the simulation (open symbols) are suppressed but smaller than uncertainties in the data.

5.6.4 Treatment of Detector Noise

Noise in the Proton Remnant Tagger

During the data taking in the years 1999 and 2000, the scintillator panels number 6 and 7 showed permanently high levels of noise. These two sub-detectors were excluded from the analysis. Additionally, the other scintillator panels show intermittent periods of high noise levels, particularly at the end of the running period of 1999. A list of runs with high noise levels in other panels was compiled by [51] and excluded from the analysis.

Calorimeter Noise

The noise in the LAr calorimeter and the SPACAL is included in the signal simulation and therefor accounted for in $C^{detector}$. The noise is not actually simulated, instead the activity in the calorimeters as measured at random times is overlaid over the simulation.

These randomly triggered events are taken when there is no nominal activity in the detector, so that the measured signal is a good estimate of the expected noise during real events. To match the noise in the Monte Carlo sample to the real data, care is taken to overlay the random activity from data taking periods representing the complete measurement.

Noise in the Forward Muon Detector

The noise in the FMD is not accounted for in the Monte Carlo simulations and has to be treated separately. The average number of spurious hits per event in the FMD can be extracted from random trigger data. As can be seen in Figure 5.14(left) the level of activity in the FMD stays constant over the entire data taking period. Thus a global correction factor representing the average FMD noise can be applied to the data. To determine the uncertainty on the average value, random trigger data is studied in groups of 35 runs. A Gaussian is then fitted to the distribution of noise in the run groups (see Figure 5.14, right). From the fit an average value of 1.2% (i.e $C^{FMD} = 1.012$) is determined with an uncertainty of 0.4%.

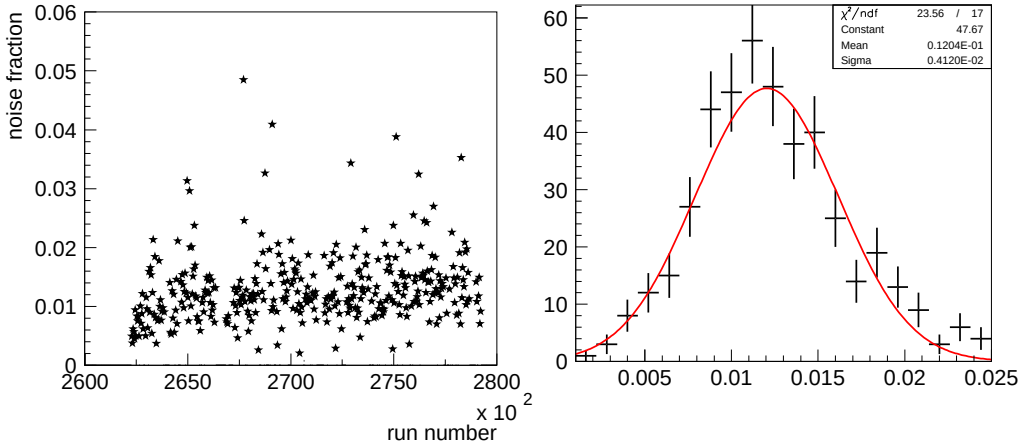

Figure 5.14: Average noise in the forward muon detector. Left: The average noise per event as a function of the run number. Each star corresponds to the sum of 35 runs, only the data taking period of 2000 is shown. Right: The distribution of noise per event in the forward muon detector for all run groups, i.e. the projection of the left graph onto the y-axis. Runs that contain no random trigger data are excluded, data from 1999 and 2000 are used.

5.6.5 Radiative Corrections

The effects of initial- and final state QED radiation are corrected in each bin of the cross sections separately. This is achieved by simulating diffractive dijet production with and without QED radiation (as described in section 4.1.1) and then dividing the resulting differential cross sections. The radiative corrections for key kinematic variables are shown in Figure 5.15. On average the radiative corrections reduce the measured cross section by $\sim 5\%$. The correction factors do not depend on most of the kinematic variables studied, with exception of y.

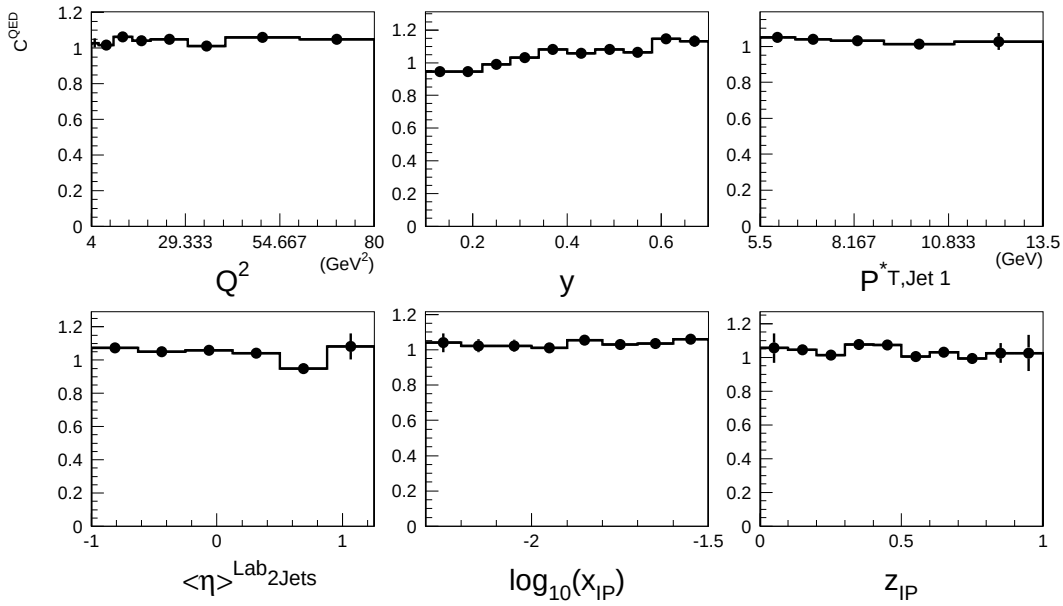

Figure 5.15: Radiative correction factors (C^{QED}) for key kinematic quantities.

5.7 Description of Diffractive Dijet Events at Detector Level by the Monte Carlo Simulation

The measured event rate at the detector level is transformed into a measurement of the differential cross section at hadron level by the correction procedure given by equation 5.22. The correction of the trigger efficiency, QED radiation and most importantly the detector acceptance in a simple bin-to-bin fashion relies on the proper description of the underlying events by the simulation. If the simulation fails to properly describe the shape of a kinematic variable, the migrations between bins in the simulation will not reflect the situation in the data, leading to deficient correction factors. For this reason it is important to ensure that the simulation describes all relevant kinematic variables.

5.7.1 Kinematic Distributions

In its raw form, the signal simulation describes the data reasonably well. However, the simulation is not perfect in all respects. The differences can be minimized by reweighting the simulation in two independent variables. The reweighting is permissible, as the signal simulation only serves to calculate correction factors for the transition to hadron level cross sections.

$\langle\eta\rangle$-Distribution As has been found in previous analyses (for example [53]) the `RAPGAP` Monte Carlo program tends to produce jets that lie more backward than observed in the data. This problem is ameliorated by reweighting the Monte Carlo simulation as a function of the average pseudorapidity of the two hardest jets in the lab-frame ($\langle\eta\rangle$). The result of this reweighting is shown in Figure 5.16.

***y*-Distribution** At very low values of y the model deviates from the data. y is highly correlated with $z_{I\!P}$, which shows similar discrepancies. Due to the correlation only one of these two variables may be reweighted. Here y was chosen, as this variable can be reconstructed with higher resolution and shows less migrations. The result of this reweighting is shown in Figure 5.17. The reweighting in y is determined after the reweighting in $\langle\eta\rangle$. However the order of the reweightings has little effect as $\langle\eta\rangle$ and y are almost completely uncorrelated.

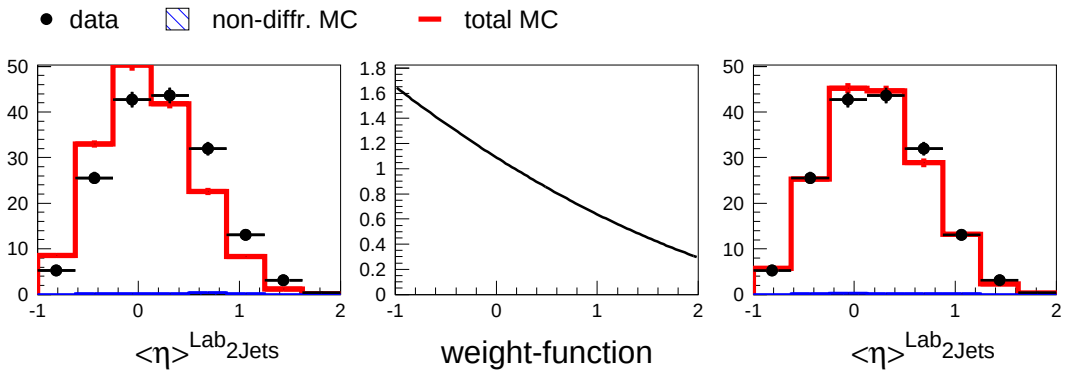

Figure 5.16: Reweighting of the $\langle\eta\rangle$ distribution. The $\langle\eta\rangle$ spectrum of the Monte Carlo simulation is compared to the data before (left) and after (right) the reweighting with the weight-function shown in the middle. The simulation is normalized to the data.

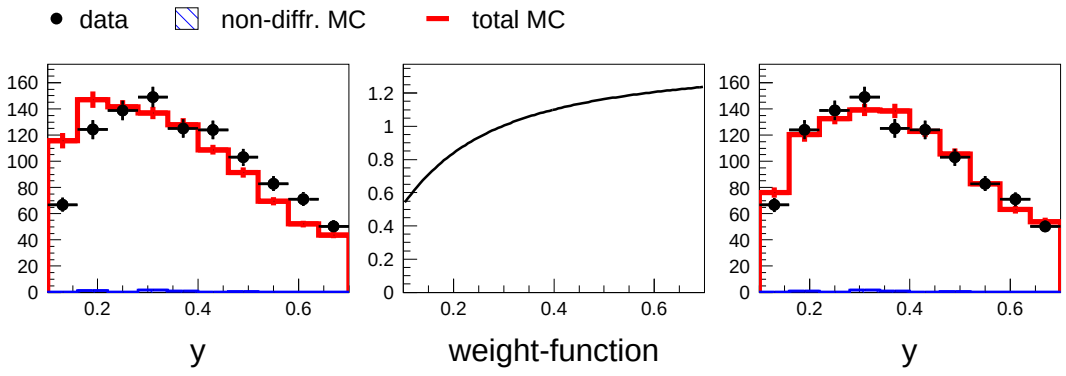

Figure 5.17: Reweighting of the y distribution. The y spectrum of the Monte Carlo simulation is compared to the data before (left) and after (right) the reweighting with the weight-function shown in the middle. The simulation is normalized to the data.

With the above reweightings applied the comparison between data and signal simulation at detector level shown in Figure 5.18 and Figure 5.19 is very good. The remaining difference between the simulation and the data is the difference in normalization. The RAPGAP program predicts $\sim 50\%$ lower cross section than measured. This can be attributed to the missing contributions of $\mathcal{O}(\alpha_s^2)$ and low mass proton dissociation in the calculation. Nevertheless, the sample can be safely used to extract the correction to hadron level, as the absolute cross section does not affect the correction factors.

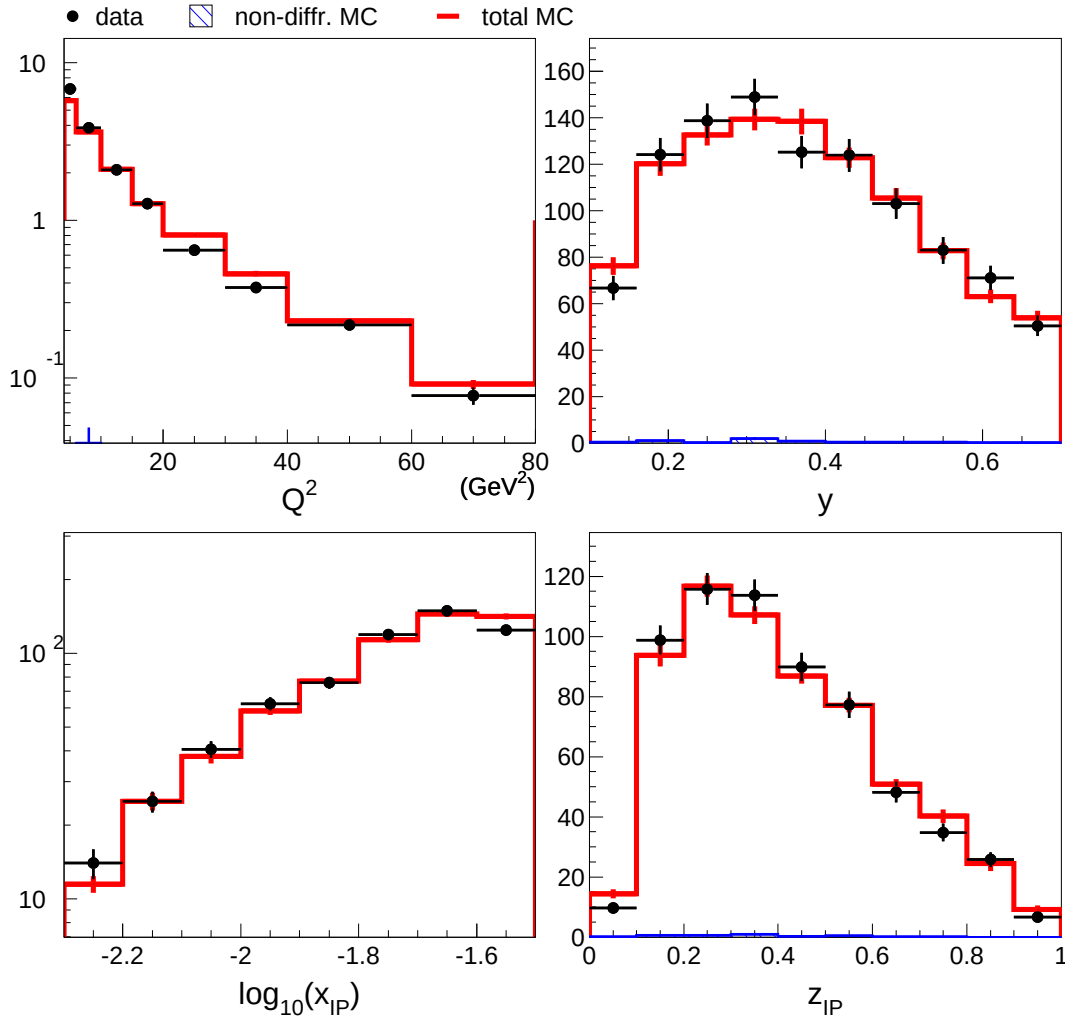

Figure 5.18: Detector level control plots. The simulation is normalized to the data.

5.7.2 Energy Flow

Once the general kinematics of diffractive dijet events are adequately described by the reweighted Monte Carlo simulation, it is important to check whether the simulation also accurately describes the distributions of the basic calorimeter clusters and cells. This is of particular importance, as the simulation is used to calculate the smearing corrections of all the jet related quantities, requiring a good match between data and the simulation even at this low level of reconstruction.

Figure 5.20 shows the average transverse energy flow per event as a function of the pseudorapidity η for all selected diffractive dijet events. Shown is the total flow, summing all combined objects (see [52] for details) and the decomposition into tracks, clusters and matched combinations contributing to the total flow. The description is generally good, showing that the simulation very closely mimics the real behavior of the detector. The simulation shown has been adjusted by all the corrections mentioned in 5.7.1. Only the signal simulation (see section 4.1.1) is presented in Figure 5.20, which is justified by the small contribution of non-diffractive background left.

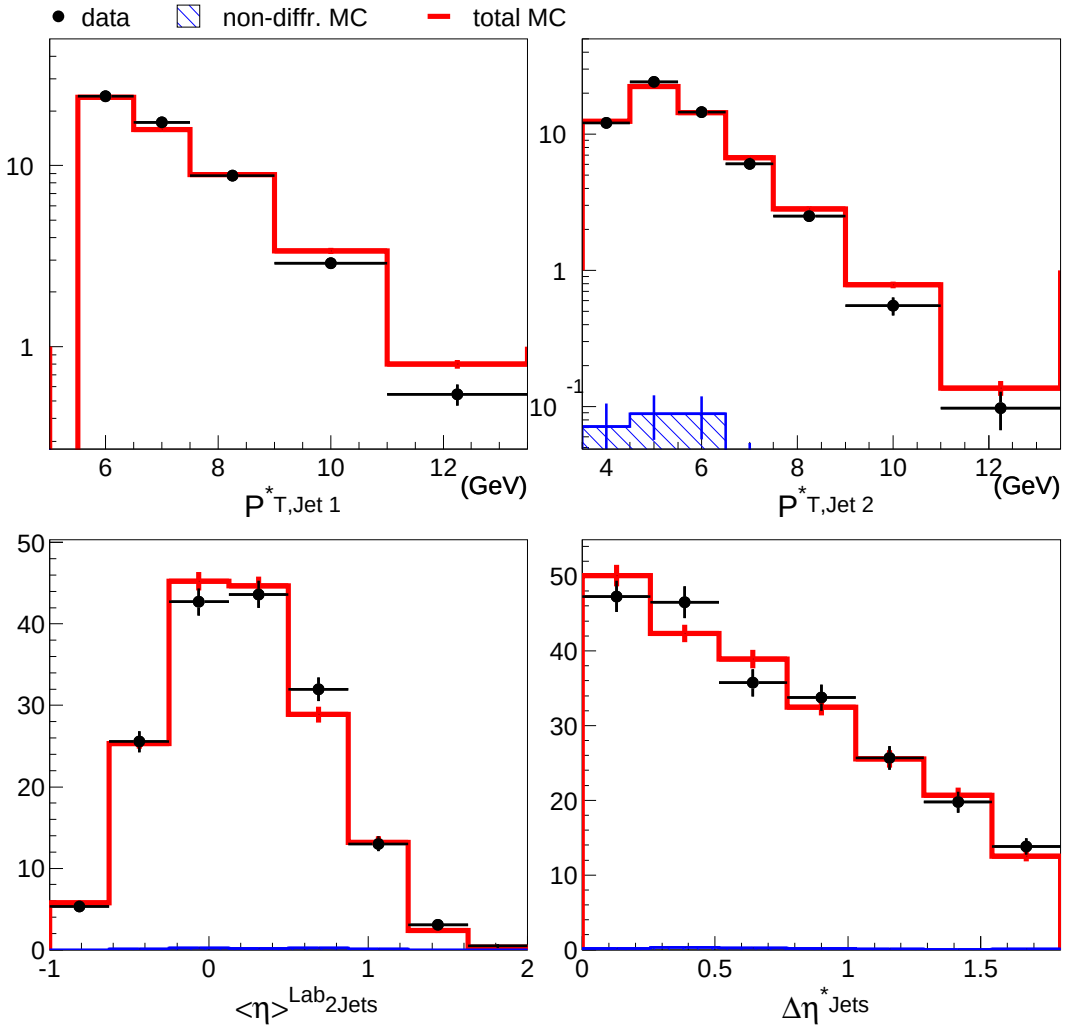

Figure 5.19: Detector level control plots. The simulation is normalized to the data.

To ensure the proper correction of all jet related quantities, the energy flow within and around the jets is studied in more detail. For the two leading jets (and in case of trijet events for the third jet) the energy deposition relative to the jet axis is measured. Figure 5.21 shows the transverse energy carried by combined objects in a band of width 2 in the $\eta - \phi$ plane. The agreement between the data and simulation is good, proving that smearing factors for jet related quantities can be calculated with the simulation presented here. In particular it can be seen that the fragmentation model used (see section 2.2.3) adequately describes the fragmentation of single partons into jets.

5.8 Correction to Hadron Level

All other detector effects, such as the geometric acceptance and detector inefficiencies not explicitely discussed above, are subsumed in the correction factor $C^{detector}$. It is computed for each bin by dividing the simulated cross section at hadron-level by the one at detector level. The signal simulation described in section 4.1.1 is used to determine

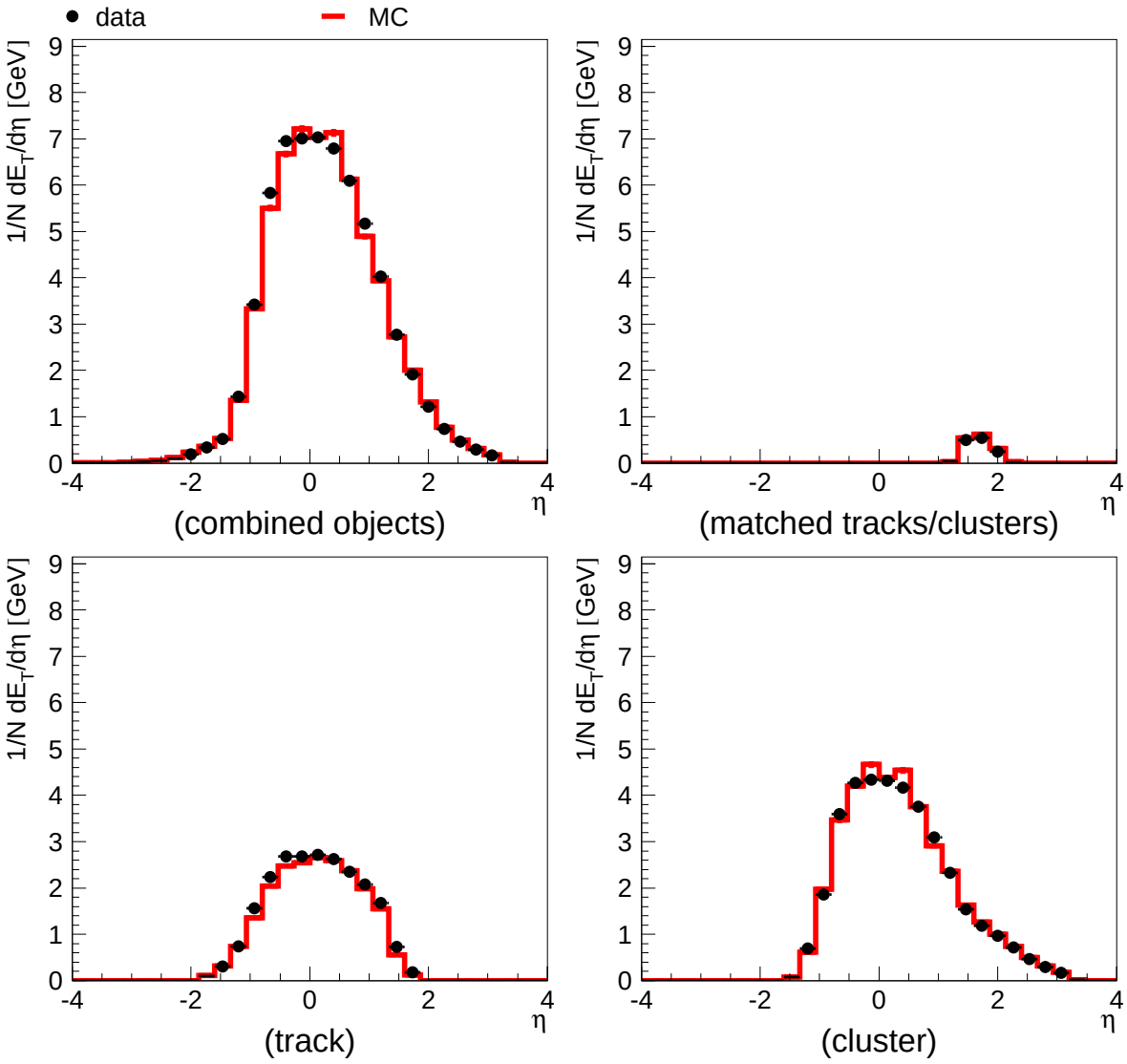

Figure 5.20: The transverse energy flow for diffractive dijet events as a function of pseudorapidity in the laboratory frame. The transverse energy from combined objects (top left), only matched tracks and clusters (top right), clusters (lower left) and tracks (lower right) are shown for data (black points) and the simulation (red line).

this correction factor. The definition of the cross section at hadron level is summarized in table 6.1. There are two notable differences in the definition compared to the detector level. While at the hadron-level a requirement for elastically scattered proton or low mass dissociative system can be imposed, one has to take recourse to a rapidity gap selection at the detector level. For compatibility to older analyses (i.e. [13]), the required pseudorapidity range required for the jets is defined in the laboratory system at detector level, but in the $\gamma^\star$p rest frame at hadron level.

Let N^{det}, N^{had} and $N^{det,had}$ be the number of events that fulfill the cross section definition at detector level, hadron level and both respectively. Then the correction

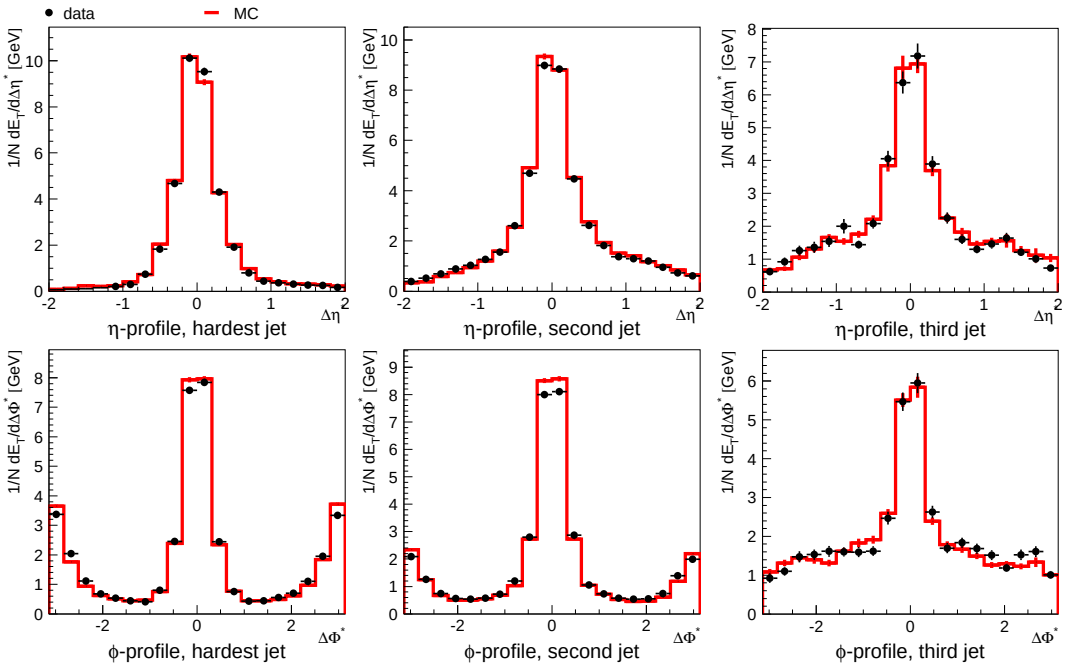

Figure 5.21: Jet profiles for the diffractive di- and trijet events. Shown is the average transverse energy per event of all combined objects as a function of the distance to the jet axis in pseudorapidity (top) and azimuthal angle (bottom). Only energy-contributions from a band of ± 1 unit in ϕ (η) are included in the profiles in η (ϕ).

factor $C^{detector}$ can be calculated as:

$$C_i^{detector} = \frac{N_i^{had}}{N_i^{det}}, \tag{5.25}$$

where i denotes a particular bin in a distribution. The applicability of this correction method is crucially dependent on an accurate description of the data by the Monte Carlo simulation, as migration-effects would otherwise lead to distortions in the hadron-level cross section. Even if the description of the detector level cross sections is good, it is necessary to ensure that migration effects are not overwhelming. To check this, typically the purity (P_i) and stability (S_i), defined as

$$P_i = \frac{N_{i,det=had}}{N_{i,det}}, \tag{5.26}$$

$$S_i = \frac{N_{i,det=had}}{N_{i,had}}, \tag{5.27}$$

are computed for each bin in all relevant histograms. Here $N_{i,det}$, $N_{i,had}$ denote the number of events in bin i (of all events that fulfill the cross section definition at detector or hadron level) for the case that the kinematic quantity under study is reconstructed at detector and hadron level respectively. $N_{i,det=had}$ is the number of events, that is reconstructed and generated in the same bin.

The purity is the fraction of events in a bin at detector level that originated in the same bin at hadron level, while the stability is the fraction of events in a bin at

hadron level that stays in this bin also at detector level. Purities and stabilities for some kinematic quantities are shown in Figure 5.22 and Figure 5.23. In general the purity and stability of quantities derived from measurements of the positron are very high, while they are rather low for the measurements involving the hadronic final state.

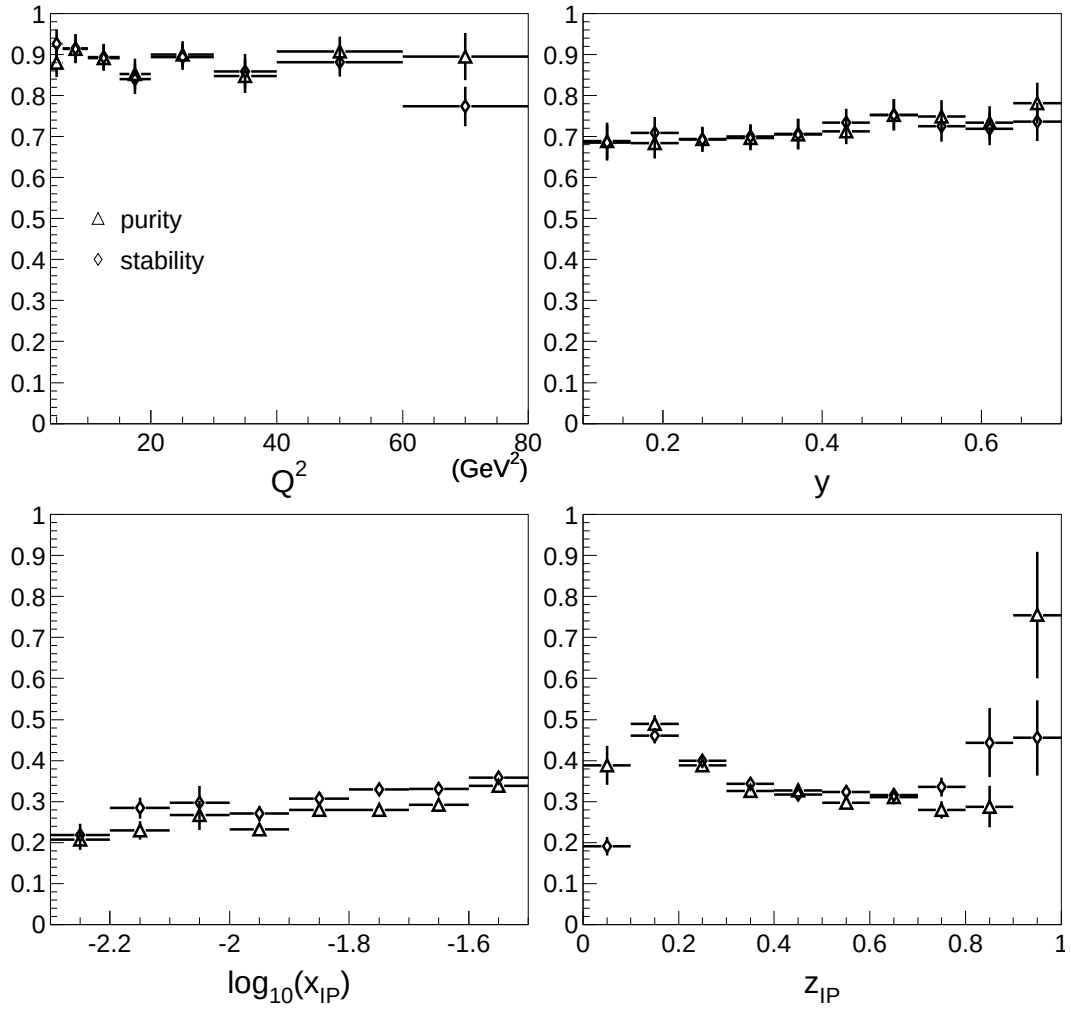

Figure 5.22: Purity and Stability

It should be noted that purity and stability as defined here are only affected by migrations in the particular variable studied. Of additional interest is the global migration in and out of the cross section definition. This can be defined in terms of global purities and stabilities, which are the fraction of events that fulfill both cross section definitions and the number fulfilling the detector- and hadron level definitions respectively. The global purity for the diffractive dijet sample is $P_{global} = 43\%$, while the global stability is $S_{global} = 48\%$. The largest migrations appear in $x_{I\!P}$ and $p_\perp^\star$.

With reasonable purities and stabilities ($\gtrsim 30\%$), the actual correction factors can then be computed. The resulting factors are shown in Figure 5.24 for selected kinematic quantities.

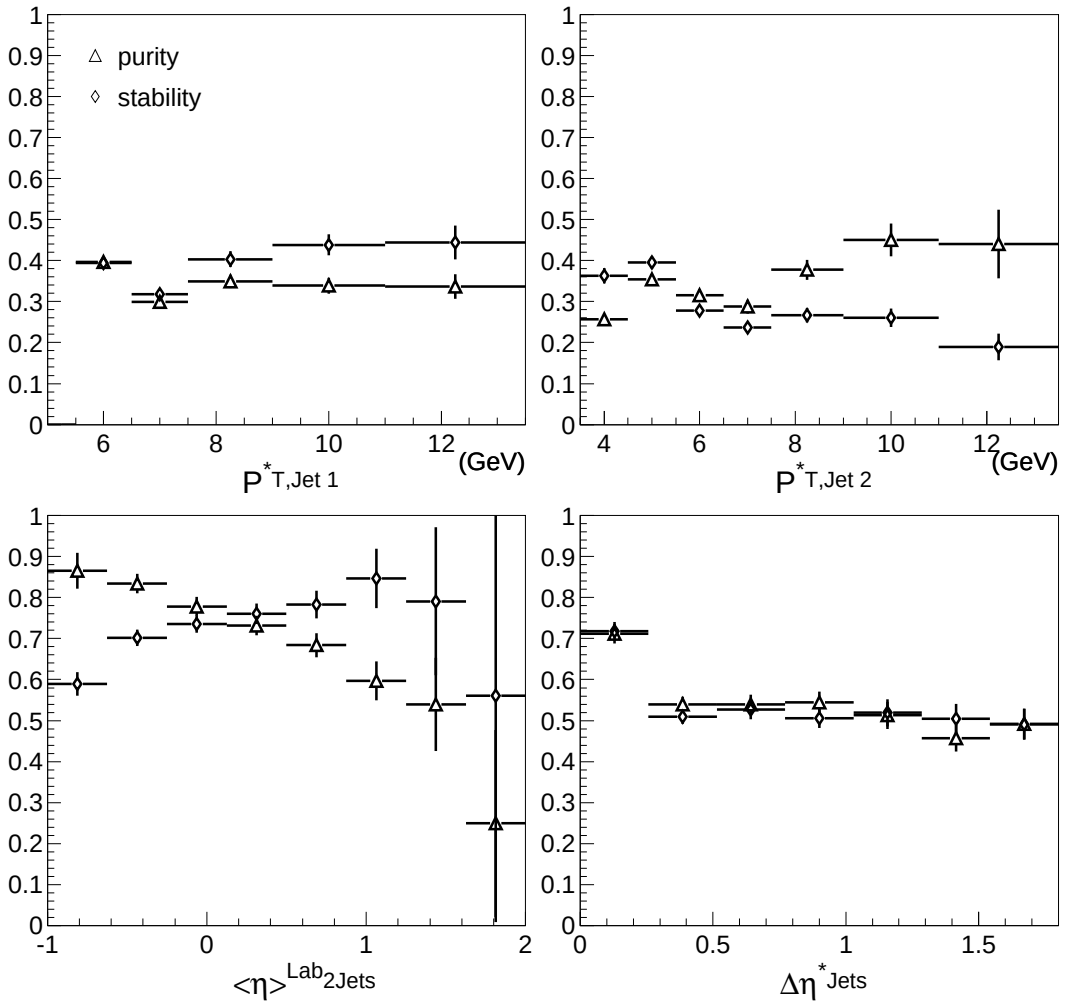

Figure 5.23: Purity and Stability. The opposite trends in purity and stability for $\langle\eta\rangle^{Lab}$ are caused by the somewhat different η ranges considered at hadron and detector level.

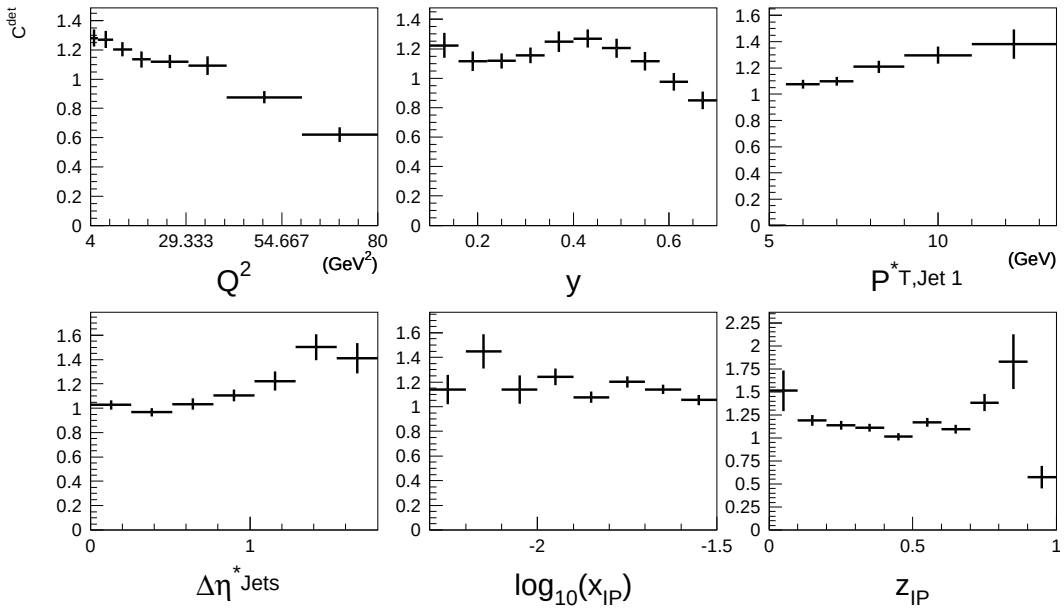

Figure 5.24: Correction factors to hadron level ($C^{detector}$).

Chapter 6

Cross Sections

The result of the correction procedure are cross sections at the stable hadron level. The cross sections presented here are defined for the kinematic region given in table 6.1. The effects of QED radiation have been separated and the cross sections corrected to QED Born level.

6.1 Systematic Uncertainties

In addition to the statistical uncertainty inherent in a measurement based on counting events systematic uncertainties of the results need to be identified and estimated. Most uncertainties were studied differentially, i.e. separately for each bin of all relevant histograms. Exceptions are the uncertainties on global correction factors (for example C^{FMD} and C_{pdiss}). The following sources of uncertainty were considered.

Table 6.1: Summary of the hadron level cross section definition

Quantity	**Range**
diffractive selection	
$x_{I\!P}$	<0.03
M_Y	<1.6 GeV
$\|t\|$	<1 GeV^2
DIS selection	
Q^2	4 - 80 GeV
y	0.1 - 0.7
jet selection	
$\eta^\star_{jet1,2}$	-3 - 0
$p^\star_{\perp,jet1}$	>5.5 GeV
$p^\star_{\perp,jet2}$	>4 GeV

Experimental Uncertainties

LAr calorimeter energy scale: The energy scale of the LAr calorimeter was varied by ±4% in the simulation, which causes a variation in the cross section of 3% to 5%. The changes in cross section are asymmetric, as jets are not only reconstructed from the calorimeter information, but also from track information. Additionally there is a subtle interplay between the $p_\perp^\star$-cut and the $x_{I\!P}$-cut. When the LAr scale is increased, more events pass the $p_\perp^\star$-cut, but M_X also rises, so more events fail the $x_{I\!P}$-cut.

Positron energy: The energy of the scattered positron is known to within 2% at $E_{e'} = 8$ GeV and 0.3% at $E_{e'} = 27.5$ GeV. This translates into a 2% uncertainty on the total cross section.

Positron angle: The uncertainty in the polar angle θ_e of the scattered positron is 1 mrad. This contributes an uncertainty of $\sim 1\%$ to the cross section.

Combined Objects: The contribution of the track momenta to the combined objects was varied by ±3%, resulting in a cross section uncertainty of 3%.

Luminosity: The measurement of the integrated luminosity $\mathcal{L}$ is accurate to within 1.5% [61]. This translates directly into a 1.5% uncertainty on the cross section.

FMD noise: The cross section is corrected for noise in the forward muon detector by a global correction factor. As described in section 5.6.4 this factor was determined as $1.2 \pm 0.4\%$. This leads to an overall normalization uncertainty of 0.4%.

Trigger efficiency: The average difference between the trigger efficiency as extracted from the Monte Carlo simulation and the data is taken as the uncertainty on the trigger efficiency. For this procedure, the trigger-efficiency as a function of Q^2, W, y and $x_{I\!P}$ is considered. As can be seen in Figure 5.13, the agreement is similar for other variables. This causes a total uncertainty of about 1%.

The largest source of experimental uncertainty is the LAr calorimeter energy scale. As the $p_\perp$-spectrum falls very steeply, small changes in the measured $p_\perp$ will lead to considerable cross section differences.

Model Uncertainties

Additionally to the experimental uncertainties discussed above, the final result also depends on the different model predictions and simulations used to correct for various effects.

$x_{I\!P}$-migration: The migrations of non-diffractive events over the cut-boundary of $x_{I\!P} < 0.03$ are sensitive to the background Monte Carlo sample used for the study. As the description of this inclusive background is far from perfect, as seen in Figure 5.11, the normalization of the background sample is varied by 50%. The resulting uncertainty on the cross section is very small ($< 1\%$) due to the small background.

M_Y and $|t|$ migration: The systematic uncertainties connected to migrations over the M_Y and $|t|$ thresholds are discussed in detail in section 5.6.1, giving a total uncertainty of 3%.

Rapidity gap selection inefficiency: The extrapolation of the cross section to diffractive events that cause activity in the forward detectors relies exclusively on the accuracy of the RAPGAP Simulation to describe the forward energy flow of diffractive events. However most analyses of diffraction use the rapidity gap- (or a related) method, and thus cannot verify that the model prediction is actually correct. In [58], the forward energy flow in diffractive DIS was investigated with a sample of elastically scattered protons actually detected in the H1 detector. The study found the RAPGAP model to be correct to within 30% (the large uncertainty is mostly a statistical error due to low sample size). The effect of this uncertainty on this measurement was estimated by reweighting all events in the signal simulation that did not pass the forward detector cuts by ±30%. This translates into a total uncertainty of 5 to 10%. However, this uncertainty shows a strong dependence on $x_{I\!P}$, as events with high $x_{I\!P}$ are much more likely to cause activity in the forward detectors than events with low $x_{I\!P}$.

Unfolding uncertainties: To evaluate the model dependence of the correction factors $C_i^{detector}$, key shapes of the Monte Carlo simulation are varied within the statistical uncertainty of the data. The following distributions are varied:

- $x_{I\!P}$ by $x_{I\!P}^{\pm 0.2}$
- $\hat{p}_\perp$ by $\hat{p}_\perp^{\pm 0.4}$
- $|t|$ by $e^{\pm 2t}$
- y by $y^{\pm 0.3}$

The largest uncertainty is introduced by the $\hat{p}_\perp$ reweighting (4%) followed by $x_{I\!P}$ (3%), while the two other variables have rather small effects. This is to be expected, because the spectra of $x_{I\!P}$ and $p_\perp$ are steep and considerable migration occurs over the cut boundaries.

Additionally there is an uncertainty due to the hadronization corrections (discussed in section 4.2.3). This uncertainty has not been considered here. However, it was investigated in the course of a similar study [62] and found to be of the order of 5%.

The influence of these uncertainties on the total cross section is summarized in table 6.1. The dominating uncertainty is originating from the uncertainty in the rapidity gap selection inefficiency (see section 5.6.2), followed by the uncertainties due to the hadronic energy scale and the variations in the Monte Carlo model (in particular the $\hat{p}_\perp$ slope).

6.2 Dijet Cross Sections

The integrated cross section in the visible range was determined to be:

$$\sigma(ep \to e' X_{2jets} Y) = 52 \pm 1 \text{ (stat.)} \; {}^{+7}_{-5} \text{ (syst.) pb.} \tag{6.1}$$

Table 6.2: Summary of systematic uncertainties. Uncertainties are classified as correlated if a particular systematic variation causes the cross section to move up or down in all bins of the eight variables shown in Figure 6.1 and Figure 6.2 simultaneously. All other uncertainties are classified as uncorrelated, although they may be anti-correlated.

Source of Uncertainty	**Uncertainty**	
	+%	-%
correlated uncertainties		
luminosity	1.5	-1.5
FMD noise	0.4	-0.4
$x_{I\!P}$-migration	0.3	-0.3
M_Y and $\|t\|$ migration	3.0	-3.0
Rapidity gap selection inefficiency	10.7	-5.0
LAr scale	5.2	-2.2
combined objects	2.6	-2.9
uncorrelated uncertainties		
trigger efficiency	0.6	-0.6
SPACAL scale	2.2	-1.5
positron angle	1.5	-0.4
unfolding uncertainties: $\hat{p}_\perp$	4.7	-4.0
unfolding uncertainties: y	1.0	-0.2
unfolding uncertainties: $\|t\|$	0.5	-0.1
unfolding uncertainties: $x_{I\!P}$	1.9	-3.5
total	**14.0**	**-9.0**

When this measurement is translated to the kinematic range of the previous H1 result [13] (i.e. different beam energy, y-range and $p_\perp^\star$-range), the two results are compatible within the uncertainties. The total cross section can be compared to the predictions based on the two parton densities determined from inclusive diffraction [12]:

$$\sigma(\text{H1 2006 DPDF fit A}) = 75\ ^{+27}_{-17}\ (\text{scale unc.})\ \text{pb}, \tag{6.2}$$

$$\sigma(\text{H1 2006 DPDF fit B}) = 57\ ^{+21}_{-13}\ (\text{scale unc.})\ \text{pb}. \tag{6.3}$$

The scale uncertainty is derived by varying the renormalization and factorization scales ($Q^2 + p_\perp^{\star 2}$) by a factor of 4 and 0.25 respectively. The H1 2006 DPDF fit A overestimates the total cross section by $\sim 40\%$, while the prediction of the H1 2006 DPDF fit B for the total cross section is compatible with the measurement within the experimental uncertainties.

The differential cross section has been measured as function of the variables Q^2, y, $x_{I\!P}$, $z_{I\!P}$, $p^\star_{\perp,1}$, $p^\star_{\perp,2}$, $\Delta\eta^\star$ and $\langle\eta\rangle^\star$ (see Figure 6.1 and Figure 6.2). The data are compared to predictions based on the two parton densities mentioned above [12].

The cross sections as a function of Q^2 and $\Delta\eta^\star$ are mostly sensitive to the hard scattering matrix element and accordingly the predictions of the two fits for these variables differ in normalization only. The agreement between the data and the

predictions is reasonable. The $x_{I\!P}$-distribution is particularly sensitive to the pomeron flux factor. As both fits have very similar flux factors, they show a very similar $x_{I\!P}$-slope, which is in good agreement with the data. In the $\langle\eta\rangle^\star$ distribution it can be clearly seen, that in the data the jets tend to be more forward than in both QCD predictions. The lacking agreement in the $\langle\eta\rangle^\star$ distribution was already observed in the comparison to the Monte Carlo simulation (see section 5.7.1) and studies of jet production in non-diffractive DIS [53]. The probable cause for this discrepancy are the simplifying assumptions of the DGLAP-evolution equations. In the Monte Carlo simulation as well as in the NLO prediction, gluon-radiation unordered in $p_\perp$ is neglected (see section 2.2.2). This unordered radiation is likely to cause extra jets in the forward direction in the data, which are neglected in the calculations.

On the one hand, the NLO prediction is quite successful at describing kinematic quantities like Q^2 and $p_\perp$, which are mainly determined by the hard scattering matrix element. On the other hand, significant differences between the data and the QCD predictions can be observed in the $z_{I\!P}$-distribution, and to a lesser degree in the y distribution, which is correlated to $z_{I\!P}$. At first glance this could be taken as evidence for the violation of QCD-factorization (see section 2.3.3). However, the $z_{I\!P}$-distribution is mainly determined by the diffractive gluon density, which was derived from the scaling violations of an F_2^D-measurement and therefore subject to rather large uncertainties at high $z_{I\!P}$. Hence the discrepancies between data and prediction in $z_{I\!P}$ may be caused by the poor knowledge of the diffractive gluon density. A combined QCD analysis of the F_2^D-measurement [12] and the dijet data sets should be suitable to extract diffractive parton-densities with higher accuracy, particularly at high $z_{I\!P}$. This reduced uncertainty will also make the combined analysis a more rigorous test of factorization.

The data set is large enough to allow the measurement of double differential cross sections. Figure 6.3 shows the dijet cross section as a function of $z_{I\!P}$ in four bins of $Q^2+p_\perp^{\star 2}$. As $Q^2+p_\perp^{\star 2}$ is used as the factorization scale for the NLO calculation, the cross section binned differentially in $z_{I\!P}$ and $Q^2+p_\perp^{\star 2}$ gives direct insight into the diffractive gluon density and its dependence on the momentum fraction and the factorization scale.

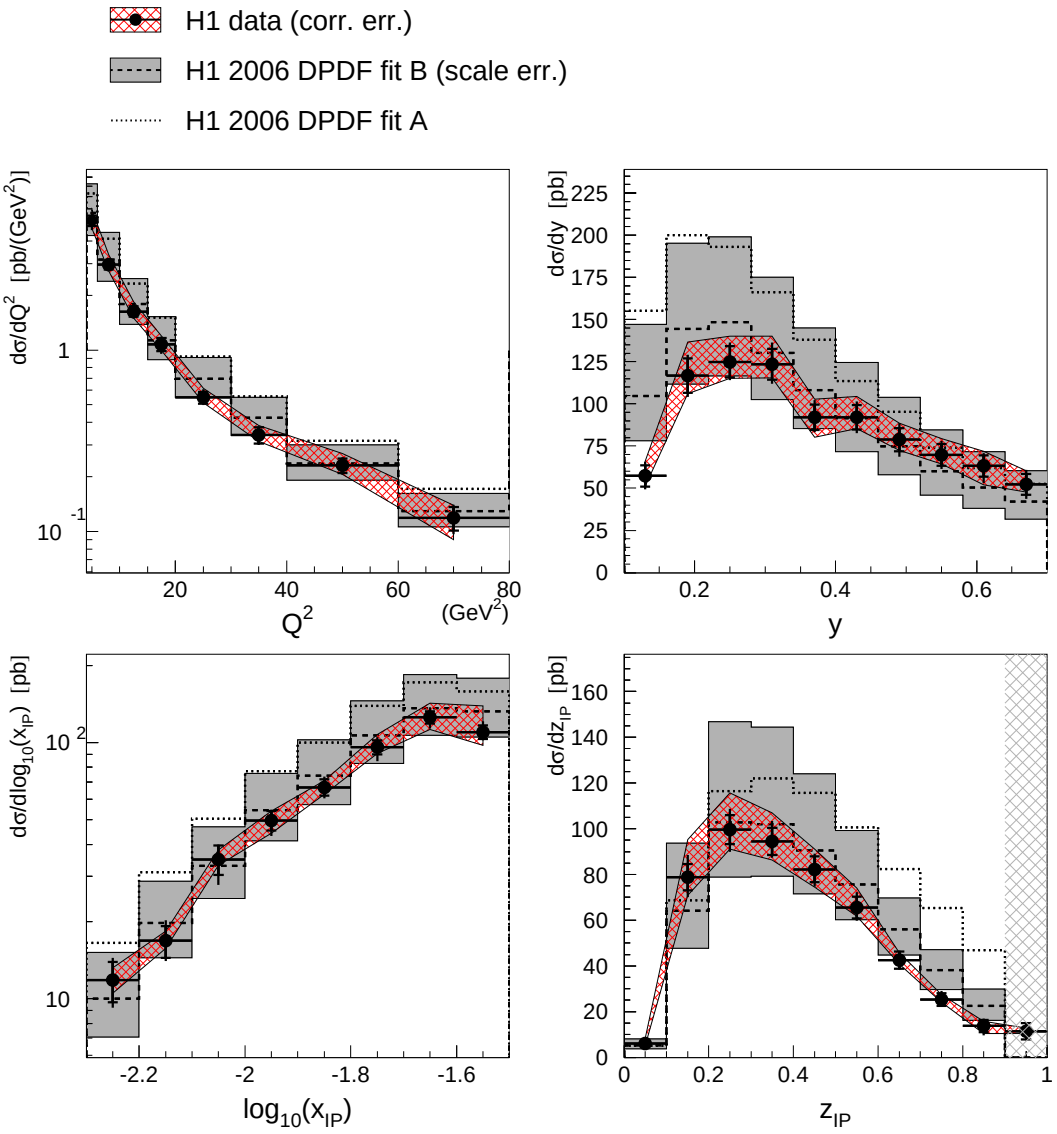

Figure 6.1: Comparison of the data (black points) to the QCD predictions based on the H1 2006 DPDF fit A (dotted line) and the H1 2006 DPDF fit B (dashed line). The inner errorbars on the datapoints represent the statistical uncertainty, the outer errorbars also include uncorrelated systematic uncertainties added in quadrature. The red hatched band shows the correlated systematic uncertainty. The prediction for the H1 2006 DPDF fit B is surrounded by a shaded band showing the scale uncertainty of the prediction (factorization- and renormalization $Q^2 + p_\perp^{\star 2}$ scale were varied by factors of 0.25 and 4. respectively). The highest bin in $z_{I\!P}$ is not compared to the prediction due to problems with the hadronization correction (see section 4.2.3).

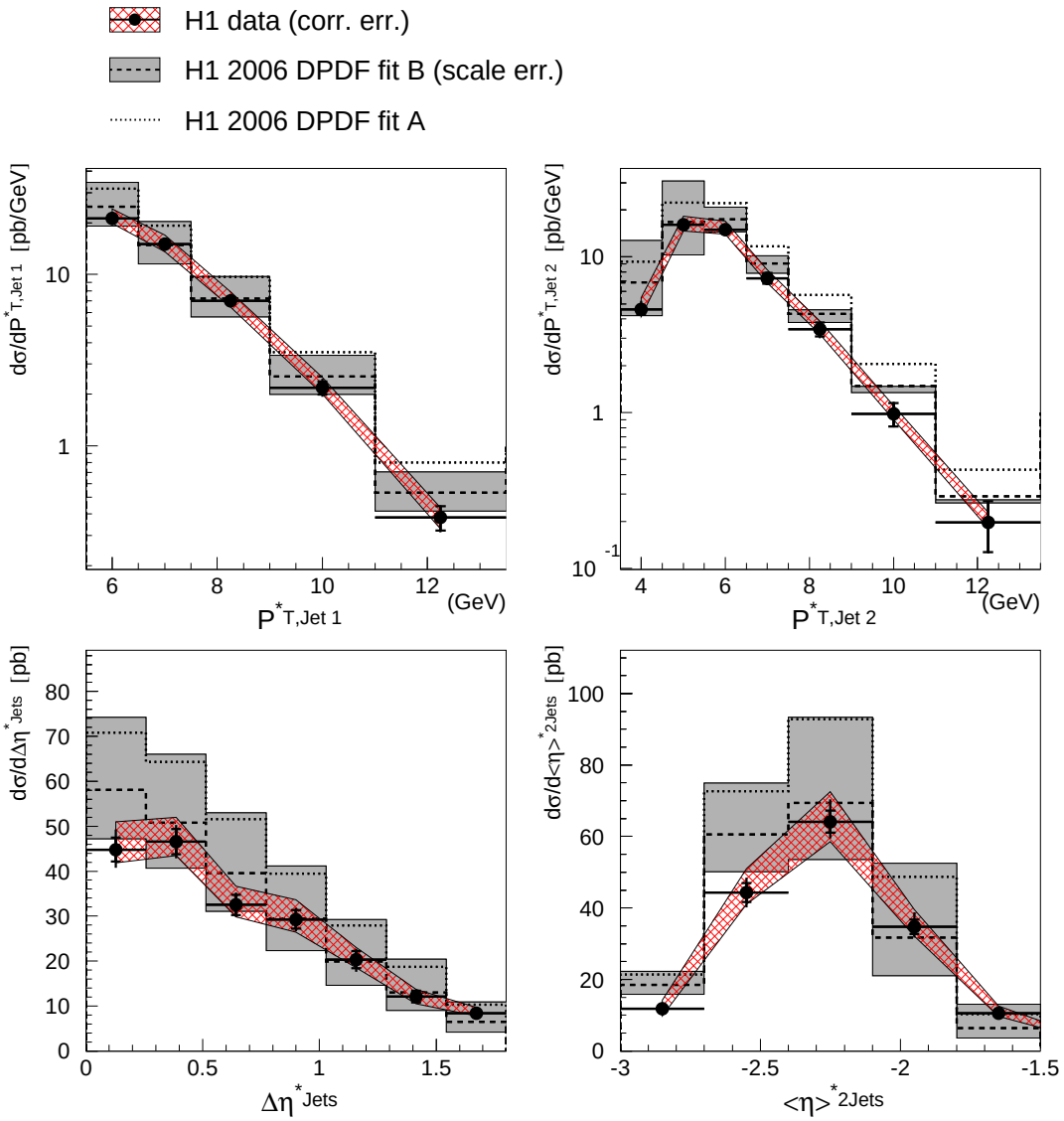

Figure 6.2: Comparison of the data (black points) to the QCD predictions based on the H1 2006 DPDF fit A (dotted line) and the H1 2006 DPDF fit B (dashed line). The inner errorbars on the datapoints represent the statistical uncertainty, the outer errorbars also include uncorrelated systematic uncertainties added in quadrature. The red hatched band shows the correlated systematic uncertainty. The prediction for the H1 2006 DPDF fit B is surrounded by a shaded band showing the scale uncertainty of the prediction (factorization- and renormalization $Q^2 + p_\perp^{\star 2}$ scale were varied by factors of 0.25 and 4. respectively).

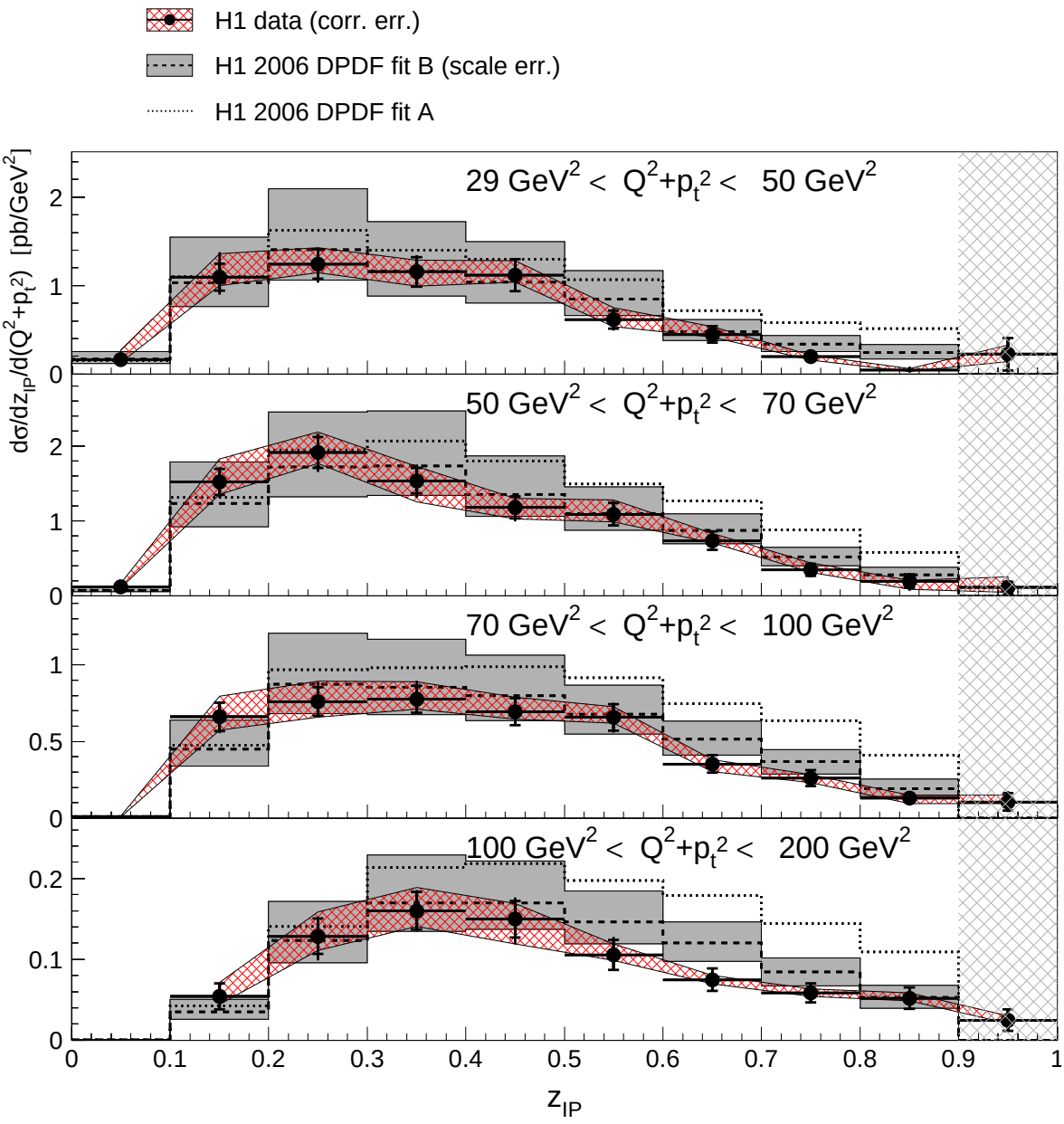

Figure 6.3: Comparison of the data (black points) to the QCD predictions based on the H1 2006 DPDF fit A (dotted line) and the H1 2006 DPDF fit B (dashed line). The inner errorbars on the datapoints represent the statistical uncertainty, the outer errorbars also include uncorrelated systematic uncertainties added in quadrature. The red hatched band shows the correlated systematic uncertainty. The prediction for the H1 2006 DPDF fit B is surrounded by a shaded band showing the scale uncertainty of the prediction (factorization- and renormalization $Q^2 + p_\perp^{\star 2}$ scale were varied by factors of 0.25 and 4. respectively). The highest bin in $z_{I\!P}$ is not compared to the prediction due to problems with the hadronization correction (see section 4.2.3).

Chapter 7

Determination of Diffractive Parton Densities

The parton densities of the pomeron can be extracted from the data by a simultaneous fit to the cross sections of inclusive diffractive scattering and diffractive dijet production. While the dijet cross sections are well suited to constrain the gluon content of the pomeron, data from inclusive diffraction in DIS are needed to determine the quark content and non-leading contributions. For this purpose, the measurement of the diffractive structure function F_2^D from H1 [12] is used.

Of particular interest in the fit is the diffractive gluon density at high momentum fractions z. The $\log Q^2$ dependence of F_2^D is proportional to the diffractive gluon density at low z, as the scaling violations are mainly caused by gluon splitting. At high z, however, the $\log Q^2$ dependence contains large contributions from gluon bremsstrahlung of quarks. This reduces the sensitivity of the F_2^D measurement to the gluon density at high z considerably, which is just the region most important for diffractive dijet production. The large uncertainties of the pure F_2^D analysis at high z can be seen in the large difference between the two densities presented in [12] and shown in Figure 7.8 and Figure 7.9.

7.1 NLO QCD Fit

The fit used is a minimum χ^2 fit taking into account correlated systematic uncertainties of the data. The χ^2 was computed as:

$$\chi^2 = \sum_{set} \sum_{i} \sigma_{i,data}^{-2} \left(\mathcal{O}^{theo}(1 - \sum_{l} s_l \sigma_{i,l}) - \mathcal{O}^{data} \right)^2 + \sum_{set} \left(\sum_{l} s_l^2 \right) \qquad (7.1)$$

Here *set* counts the different data sets: one set of dijet cross sections and two sets of inclusive diffraction taken at different beam energies (see [12] for details). The index i denotes the individual data points. The predicted and measured observables are denoted by $\mathcal{O}^{theo}$ and $\mathcal{O}^{data}$ respectively. $\sigma_{i,data}$ is the uncorrelated uncertainty for each data point, while $\sigma_{i,l}$ is the correlated uncertainty from the systematic source l. To properly treat correlated uncertainties, they are weighted by the factors s_l which contribute to χ^2 themselves due to the so called counterterm. For the dijet data, the

uncertainty is split into two contributions: the correlated uncertainty (see table 6.1) and the uncorrelated uncertainty, which is the quadratic sum of statistical and uncorrelated systematic uncertainty. For the F_2^D data the uncertainties were treated as described in [12].

The fit is based on the program `QCDFIT` [63] originally developed for the analysis of the parton densities of the proton. The program was extended in the course of this study to allow for the inclusion of the diffractive dijet data. In `QCDFIT` the parton densities are evolved according to the DGLAP equations and then used to predict the reduced cross section of the inclusive diffractive measurement and the diffractive dijets. The actual minimization of χ^2 is then delegated to the `MINUIT` package [64].

7.1.1 Generation of Candidate Parton Densities

The fit has three groups of free parameters. Two sets of parameters are used to describe the quark and gluon density of the pomeron while the third governs the pomeron and reggeon flux factors. The parton densities of the pomeron are parameterized at a fixed factorization scale of $\mu_{f,0}^2 = 2.5$ GeV^2 as functions of the momentum fraction z by the function:

$$A \cdot z^B \cdot (1-z)^C \tag{7.2}$$

where A, B and C are free parameters to be determined by the fit. This function is a simplified version of the fit function used in many fits of parton densities of the proton, for example in [65]. The values of the parton densities at all other scales μ_f^2 are then obtained by solving the DGLAP evolution equations. The only free parameter for the pomeron flux is $\alpha(0)_{I\!P}$ (see equation 2.27), all other parameters describing the flux factor were taken from an analysis where the elastically scattered proton is detected in the H1 detector [37]. This actual detection of the outgoing proton provides for a direct determination of the flux parameters. The flux factor for the reggeon exchange was also determined in [37]. The fixed input parameters are summarized in 7.1.

Table 7.1: Fixed parameters used in the fit (see equations 2.26 and 2.27).

Parameter	Value		Source
$\alpha'_{I\!P}$	$0.06^{+0.19}_{-0.06}$	GeV^{-2}	[37]
$b_{I\!P}$	$5.5^{+0.17}_{-2.0}$	GeV^{-2}	[37]
$\alpha(0)_{I\!R}$	0.5 ± 0.1		[14]
$\alpha'_{I\!R}$	$0.3^{+0.6}_{-0.3}$	GeV^{-2}	[37]
$b_{I\!R}$	$1.6^{+0.4}_{-1.6}$	GeV^{-2}	[37]
m_c	1.4 ± 0.2	GeV	[25]
m_b	1.5 ± 0.5	GeV	[25]
$\alpha_s(M_Z^2)$	0.118 ± 0.002		[25]

As the data selection is optimized for the analysis of diffraction, the reggeon contribution plays only a minor role and the parton densities for the reggeon part cannot be extracted from the data sets. Instead the parton densities for the reggeon

are taken from [36]. Due to the small effect of this contribution, the exact choice of parton densities is of little influence as discussed in [12]. Only the normalization of the reggeon contribution enters into the fit as a free parameter. The effects of the possible interference between pomeron and reggeon were neglected, as a previous study [14], which explicitly investigated this effect, found little difference assuming either no or maximal interference.

7.1.2 Parameterization of Dijet Cross Sections

Originally the prediction of diffractive dijet cross sections was not within the scope of the `QCDFIT` program. This capability was added in the course of this study. The parton densities computed in `QCDFIT` are used as the basis for a prediction of the dijet cross section based on the `nlojet++` program, which was adapted for diffraction as described in section 4.2.

For each step in the χ^2 minimization the parameters change and therefore a new calculation is necessary to account for the change of the parton densities. However, a proper calculation of the prediction with `nlojet++` is too time consuming to be feasible. Instead the calculation is parameterized as function of α_s, $x_{I\!P}$, the momentum fraction z and the renormalization- and factorization scale (here $Q^2 + p_\perp^{\star 2}$) similar to the approach used in [66]. To achieve this, the `nlojet++` prediction is computed in bins of $x_{I\!P}$ (index j), z (index k) and $\mu_r^2 = \mu_f^2$ (index l), separately for leading and next to leading order (index m) and for the contributions of different initial partons (index n, separated into gluon, up-type quark and down-type quark). The actual matrix element $\tilde{\sigma}_{j,k,l,m,n}(z_{I\!P})$ for each bin and contribution can be extracted by dividing the corresponding bin by the appropriate power of α_s, parton density and pomeron flux. A close approximation to the full NLO calculation for a different set of parton densities can then be obtained by computing:

$$\sigma(z_{I\!P}) = \sum f_n^{I\!P}(z_{I\!P,k}, \mu_l^2) \cdot \alpha_s^m \cdot \tilde{\sigma}_{j,k,l,m,n}(z_{I\!P}) \cdot f_{I\!P}(x_{I\!P,j}), \tag{7.3}$$

where $f_n^{I\!P}$ are the diffractive parton densities and $f_{I\!P}(x_{I\!P,j})$ the pomeron flux, introduced in section 2.3.3. The binning in $x_{I\!P}$ coincides with the binning in the data, while ten bins were chosen for $\mu_r^2 = \mu_f^2$ and z.

The described procedure greatly decreases computation time as to make the fit viable. The parameterized prediction is a very close approximation to the proper calculation, as long as the parton densities used to generate and evaluate the parameterization don't differ too widely. To ensure a proper determination of the parton-densities from the fit, the results from a first fit are used to generate a new parameterization of the prediction and the fit is repeated. This step is repeated until the resulting parton densities are stable, typically after one iteration (i.e. checking with the new parameterization shows no significant difference in the fit-result).

The reggeon-contribution to the dijet cross section is computed with the `nlojet++` program using the parton densities from [36]. As only the normalization of this contribution is varied in the fit, no parameterization of the reggeon contribution is necessary.

7.1.3 Prediction of the Inclusive Cross Section

The calculation of the cross section of inclusive scattering is much more straight forward. The exact quantity measured in the H1 analysis of inclusive diffraction [12] is $x_{I\!P}\sigma_r^{D(3)}(x_{I\!P}, \beta, Q^2)$, where $\sigma_r^{D(3)}$ is the so called reduced cross section defined by:

$$\frac{\mathrm{d}^3\sigma_{ep\to eXY}}{\mathrm{d}x_{I\!P}\mathrm{d}\beta\mathrm{d}Q^2} = \frac{4\pi\alpha_{em}^2}{\beta^2 Q^4} \cdot Y_+ \cdot \sigma_r^{D(3)}(x_{I\!P}, \beta, Q^2), \tag{7.4}$$

where $Y_\pm = 1 \pm (1-y)^2$. In the approximations discussed in section 2.3.3, the reduced cross section is identical to $F_2^{D(3)}$. The high precision of the measurement, however, compels a more sophisticated treatment, which leads to a description of $\sigma_r^{D(3)}$ in terms of three diffractive structure functions $F_2^{D(3)}$, $F_L^{D(3)}$ and $xF_3^{D(3)}$, similar to inclusive DIS [67]:

$$\sigma_r^{D(3)} = F_2^{D(3)} - \frac{y^2}{Y_+}F_L^{D(3)} - \frac{Y_-}{Y_+}xF_3^{D(3)}. \tag{7.5}$$

$F_3^{D(3)}$ originates from the difference between u- and d quark contents. As in this analysis the pomeron is assumed to be flavor symmetric, $F_3^{D(3)}$ is zero throughout. The other two structure functions are computed to next to leading order from the parton densities by the `QCDFIT` program. The contribution of the reggeon to the reduced cross section is calculated similarly.

The reduced cross section is fitted in the kinematic region of $Q^2 \geq 8.5$ GeV^2 and $M_X > 2$ GeV, although data is available at lower Q^2 and M_X. The restriction in M_X is placed to avoid the resonance region, which is not expected to be adequately described by the quark parton model. The limit on Q^2 was imposed in the F_2^D-analysis [12] to avoid a systematic dependence of the fit results on the lower bound in Q^2 that is observed below 8.5 GeV^2. Both selections follow the described analysis in the F_2^D-study [12].

7.2 Results

Most importantly, it can be stated that a single set of parton distributions and corresponding flux factor can consistently describe the combined data set of dijets and inclusive diffractive scattering. A χ^2/ndf of 196/218 suggests no measurable tensions between the two data sets. Of the total χ^2 27 originate from the 36 dijet datapoints, while the remaining χ^2 of 169 is the contribution of the 190 F_2^D datapoints. The result can also be taken as an indication that the factorization of the diffractive structure function into a pomeron flux and parton densities of the pomeron is a valid approach. The fit results are summarized in tables 7.2 and 7.3.

Notably, the parameter C_{gluon} (the exponent of $(1-z)$) is determined to be positive. C_{gluon} controls the behavior of the gluon density at high z. A positive value indicates that the density approaches zero as z goes to one, as one should expect in the quark parton model. This contrasts with the results from the fit to the F_2^D data alone [12], where C_{gluon} is fitted to a negative value, and the gluon density needs to be suppressed at high z to avoid the resulting singularity at $z = 1$.

Figure 7.1 to Figure 7.4 show the measurement of the reduced cross section obtained from the QCD analysis of the inclusive measurement [12] compared to the results

Table 7.2: Fit results.

Parameter	Fit Value	
$\alpha(0)_{I\!P}$	1.104	± 0.015
$n_{I\!R}$	0.13×10^{-2}	$\pm 0.1 \times 10^{-2}$
A_{gluon}	0.88	± 0.13
B_{gluon}	0.33	± 0.11
C_{gluon}	0.91	± 0.25
A_{quark}	0.13	$\pm 0.9 \times 10^{-2}$
B_{quark}	1.5	± 0.07
C_{quark}	0.51	± 0.09

Table 7.3: Correlation matrix for the fit results.

	A_{gluon}	B_{gluon}	C_{gluon}	A_{quark}	B_{quark}	C_{quark}	$\alpha(0)_{I\!P}$	$n_{I\!R}$
A_{gluon}	1.000	0.933	0.789	0.367	0.360	0.298	0.091	0.109
B_{gluon}	0.933	1.000	0.602	0.378	0.429	0.297	0.118	0.264
C_{gluon}	0.789	0.602	1.000	-0.001	-0.111	-0.016	-0.167	-0.005
A_{quark}	0.367	0.378	-0.001	1.000	0.947	0.950	0.177	0.034
B_{quark}	0.360	0.429	-0.111	0.947	1.000	0.846	0.243	0.072
C_{quark}	0.298	0.297	-0.016	0.950	0.846	1.000	0.161	0.032
$\alpha(0)_{I\!P}$	0.091	0.118	-0.167	0.177	0.243	0.161	1.000	0.346
$n_{I\!R}$	0.109	0.264	-0.005	0.034	0.072	0.032	0.346	1.000

of the combined fit and the H1 2006 DPDF fits A and B. Within the fitted range ($Q^2 \geq 8.5$ GeV^2 and $M_X > 2$ GeV) the three fits are nearly identical. They mainly differ in their extrapolation to low Q^2 and low β. This is not unexpected, as already the two fits obtained from the QCD analysis of the F_2^D-data [12] show this effect. The χ^2-contribution of the F_2^D data of 196 in the combined fit is somewhat greater than the χ^2 of the two fits presented in [12], 158 and 165 for the H1 2006 DPDF fit A and H1 2006 DPDF fit B respectively. This difference in χ^2 is not located in any particular part of the phase-space.

Comparing Figure 6.3 and Figure 7.5 shows a large change in the prediction for the dijet cross section in the combined fit compared to the H1 2006 DPDF fit, while only marginal changes occur in the prediction for the F_2^D measurement as shown in Figure 7.1 to Figure 7.4. This clearly demonstrates that both data sets impose independent constraints on the parton densities.

Additionally, predictions based on the combined fit can be compared to the data as a function of other kinematic variables as shown in Figure 7.6 and Figure 7.7. Compared to the predictions from the H1 2006 DPDF fits, the agreement has improved consistently over all variables. This can be seen most prominently in the $z_{I\!P}$ distribution and also in the closely correlated y distribution. The improvement is somewhat smaller but

still significant in the $p_\perp^\star$ distributions (especially at high $p_\perp^\star$). The shape of the $x_{I\!P}$ distribution is equally well described by the fits, as the pomeron flux has changed only marginally compared to the H1 2006 DPDF fit. The distributions in Q^2 and $\Delta\eta^\star$ are not sensitive to the diffractive parton distributions and the different predictions differ mostly in their normalization. The difference by all data and NLO prediction in $\langle\eta\rangle^\star$ persists in the combined fit, which is to be expected, as this effect is most likely caused by missing gluon radiations in the forward direction.

7.3 Diffractive Parton Densities

Figure 7.8 and Figure 7.9 show the diffractive parton densities derived from the combined fit compared to the parton densities obtained from the F_2^D-measurement alone [12]. In addition to the experimental uncertainties, which are accounted for in the χ^2 calculation, several theoretical uncertainties need to be considered. First of all, the fixed parameters, listed in table 7.1 that enter the fit have uncertainties that are not directly accounted for in the fit. Additionally there is the relative scale uncertainty of the dijet cross section prediction compared to the inclusive F_2^D-measurement. These uncertainties can be studied by varying the corresponding parameters and observing the change in the fit result. The fixed parameters are varied one by one within one standard deviation as given in table 7.1 and the fit is repeated with the changed parameter. The resulting differences between the nominal fit and the varied fits are added quadratically to the experimental uncertainty. Similarly the initial scale $\mu_{f,0}^2$ is changed to 3.5 GeV^2 and the fit repeated. Furthermore the stability of the fit under variations of the fit limit is tested by including only the dijet datapoints that fulfill $z_{I\!P} > 0.2$ in the fit. Additionally the relative scale of the dijet and inclusive data is investigated. This is done by using $f \cdot (Q^2 + p_\perp^{\star 2})$ as renormalization and factorization scale for the dijet prediction, where $f = 1$ corresponds to the nominal fit. The fit is repeated for several values of f. The resulting χ^2 form a parabola as function of $\log(f)$, as can be expected from the logarithmic dependence of the dijet cross section on the renormalization and factorization scale. The change in parton densities due to a different relative scale corresponding to a $\Delta\chi^2 \approx 1$ (i.e. $f = 0.5$ and $f = 1.5$) is then added quadratically to the uncertainty band. The differences in the resulting parton densities are added quadratically neglecting all correlations between the theoretical uncertainties. This poses no problem over most of the phase space, where experimental uncertainties dominate. However, for the gluon density at high z the uncertainty may be underestimated due to the neglected correlations.

The contribution of the theoretical uncertainties is shown in Figure 7.8 and Figure 7.9 as light blue band and is given in more detail in tables 7.4 and 7.5. Of the theoretical uncertainties discussed above the relative scale uncertainty and the variation in the fit range are dominant in the high z region of the gluon density, while at low z the uncertainty on the charm quark mass, α_s and the choice of initial parameterization scale $\mu_{f,0}^2$ have the largest effects. At high z, experimental and theoretical uncertainty contribute equally to the total uncertainty, while the experimental uncertainty dominates at low z. The quark density is only constrained by the F_2^D-data and therefore is nearly unchanged in all systematic variations.

Table 7.4: Uncertainties of the gluon density from different sources at $\mu_f^2 = 90$ GeV^2.

z		**0.01**		**0.1**		**0.5**		**0.8**	
		+%	−%	+%	−%	+%	−%	+%	−%
error source	experimental	14	14	11	11	15	15	32	32
	flux factors	1	2	1	2	< 1	< 1	2	< 1
	m_c	6	6	5	5	3	3	< 1	< 1
	m_b	< 1	< 1	< 1	< 1	< 1	< 1	< 1	< 1
	α_s	3	3	4	4	5	5	5	5
	$\mu_{f,0}^2$	13	-	11	-	3	-	< 1	-
	$z_{I\!P} > 0.2$	1	-	1	-	11	-	33	-
	relative scale	< 1	1	1	3	11	20	28	40
total		**20**	**16**	**17**	**13**	**22**	**25**	**54**	**51**

Table 7.5: Uncertainties of the quark density from different sources at $\mu_f^2 = 90$ GeV^2.

z		**0.01**		**0.1**		**0.5**		**0.8**	
		+%	−%	+%	−%	+%	−%	+%	−%
error source	experimental	14	14	10	10	6	6	10	10
	flux factors	1	2	1	2	< 1	< 1	< 1	< 1
	m_c	6	7	6	7	< 1	1	< 1	1
	m_b	< 1	< 1	< 1	< 1	< 1	< 1	< 1	< 1
	α_s	< 1	< 1	< 1	< 1	< 1	< 1	< 1	< 1
	$\mu_{f,0}^2$	4	-	3	-	< 1	-	2	-
	$z_{I\!P} > 0.2$	< 1	-	< 1	-	< 1	-	< 1	-
	relative scale	< 1	< 1	< 1	< 1	< 1	< 1	< 1	< 1
total		**16**	**16**	**12**	**12**	**6**	**6**	**10**	**10**

The gluon density of the combined fit is quite different from the H1 2006 DPDF fit A, while it is rather close to the H1 2006 DPDF fit B. Not surprisingly, this behavior closely follows the situation observed in the $z_{I\!P}$-distribution (see Figure 6.1), which deviates significantly from the QCD prediction based on the H1 2006 DPDF fit A at $z_{I\!P} \gtrsim 0.4$. The agreement between the three densities at low z is worse than could be expected from the fact that all three fits use identical data in this kinematic region. This shows, that there exist long ranging correlations in the parton densities, so that changes at high z, where the new data is located, will also lead to changes at low z. These correlations could be an effect of the choice of parameterization or a direct result of the DGLAP evolution equations.

The uncertainty due to the choice of initial parameterization is much harder to estimate: different parameterizations may be tried, but there is little physical motivation other than the resulting χ^2 for any particular choice. In addition to the nominal fit, which uses equation 7.2 to parameterize both the gluon and the quark density, several

different parameterizations were used:

gluon	quark	
A	$A \cdot z^B \cdot (1-z)^C$	(7.6)
$A \cdot z^B \cdot (1-z)^C(1+E \cdot z)$	$A \cdot z^B \cdot (1-z)^C$	(7.7)
$A \cdot z^B \cdot (1-z)^C(1+D \cdot \sqrt{z}+E \cdot z)$	$A \cdot z^B \cdot (1-z)^C(1+D \cdot \sqrt{z}+E \cdot z)$	(7.8)

The restricted parameterization of equation 7.6, which correspond to the H1 2006 DPDF fit B, yields a much worse χ^2 than the nominal fit ($\chi^2 = 221$, nominal:$\chi^2 = 196$), most likely because the parameterization of the gluon density is not flexible enough. The extended parameterizations that introduce additional parameters with respect to the nominal fit (equations 7.7 and 7.8), however, lead only to negligible improvements in χ^2 ($\Delta\chi^2 \approx 0.5$). The results with different initial parameterizations are shown in Figure 7.10 and Figure 7.11. In all aspects the fit using the reduced parameterization of equation 7.6 is very close to the H1 2006 DPDF fit B. Both fits use the same parameterization, in particular the constant function for the gluon. This parameterization seems to be overly restrictive, as indicated by the considerable change in the parton densities and decrease in χ^2 when adding more parameters.

At high z the quark densities of all fits are reasonably close to each other, while more prominent differences occur at low z. The cause for the observed discrepancies is most probably the even larger difference in the gluon density at high z that influence the quark densities due to the DGLAP evolution.

The gluon density at high z of the nominal combined fit and the extended fits is quite different from the H1 2006 DPDF fit A but consistent with each other. The results of the H1 2006 DPDF fit B and the restricted combined fit lie in between the two extremes. At lower z the nominal and extended combined fits are quite close to the H1 2006 DPDF fit A, while the reduced combined fit and the H1 2006 DPDF fit B lie considerably higher. This effect is probably caused by the correlations between the low and high z regions of the gluon density that are particularly pronounced in these fits due to the very restrictive parameterization of the gluon density.

Considering only the various combined fits, the parameterization dependence of the parton densities has been reduced compared to the pure F_2^D fit. This shows that the inclusion of the dijet data in the fit improves the reliability of the extracted parton densities.

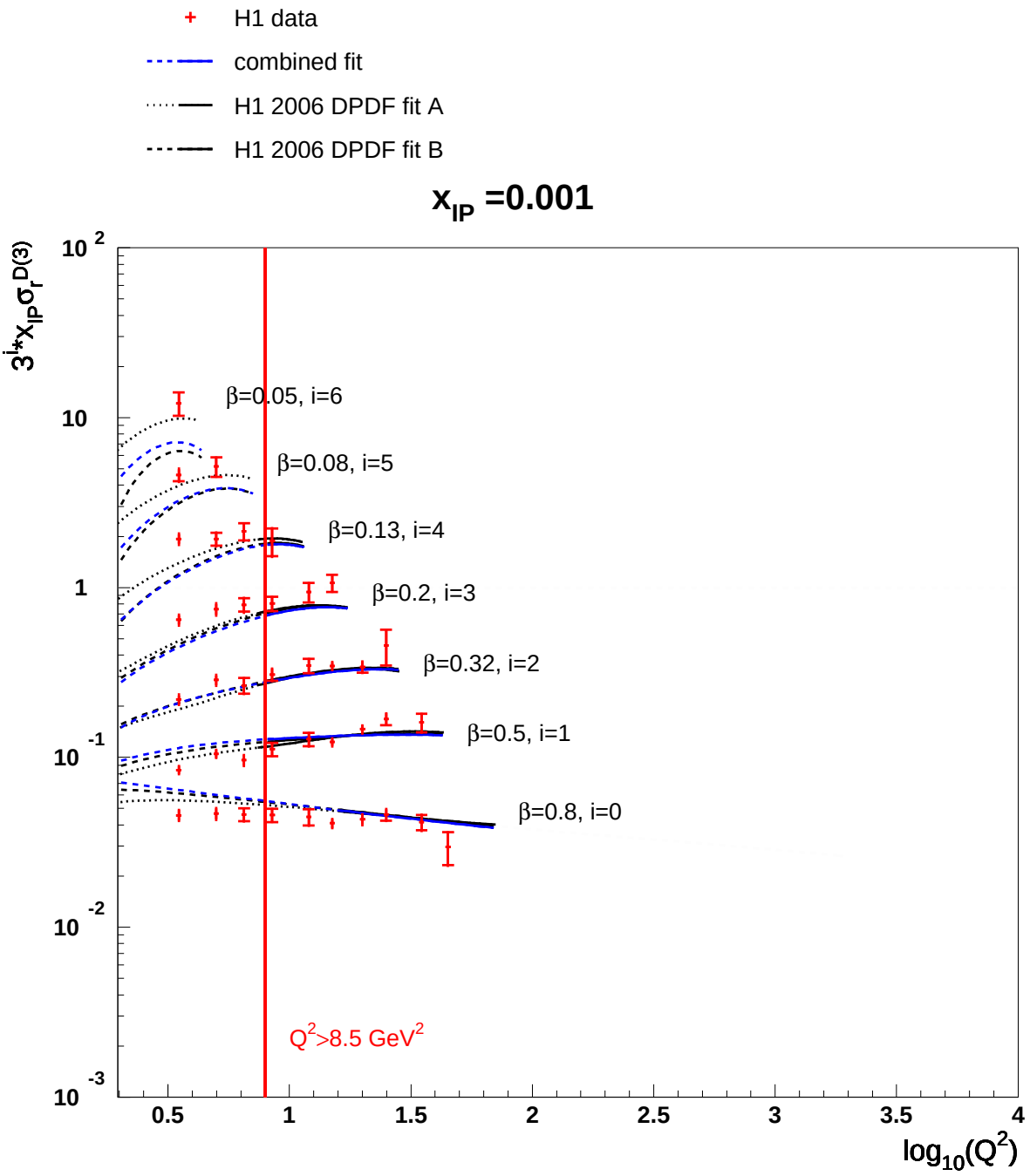

Figure 7.1: The β and Q^2 dependence of the diffractive reduced cross section $\sigma_r^{D(3)}$ multiplied by $x_{I\!P}$ at $x_{I\!P}$=0.001. The cross sections are multiplied by powers of 3 for better visibility. The inner and outer errorbars on the datapoints represent the statistical and total uncertainties, respectively. The data are compared to the results of the combined fit for $E_p = 820$ GeV, which is shown by blue lines. The dashed line indicates the prediction in kinematic regions that were not included in the fit. The two results from [12] are shown as dotted black line (H1 2006 DPDF fit A) and dashed black line (H1 2006 DPDF fit B).

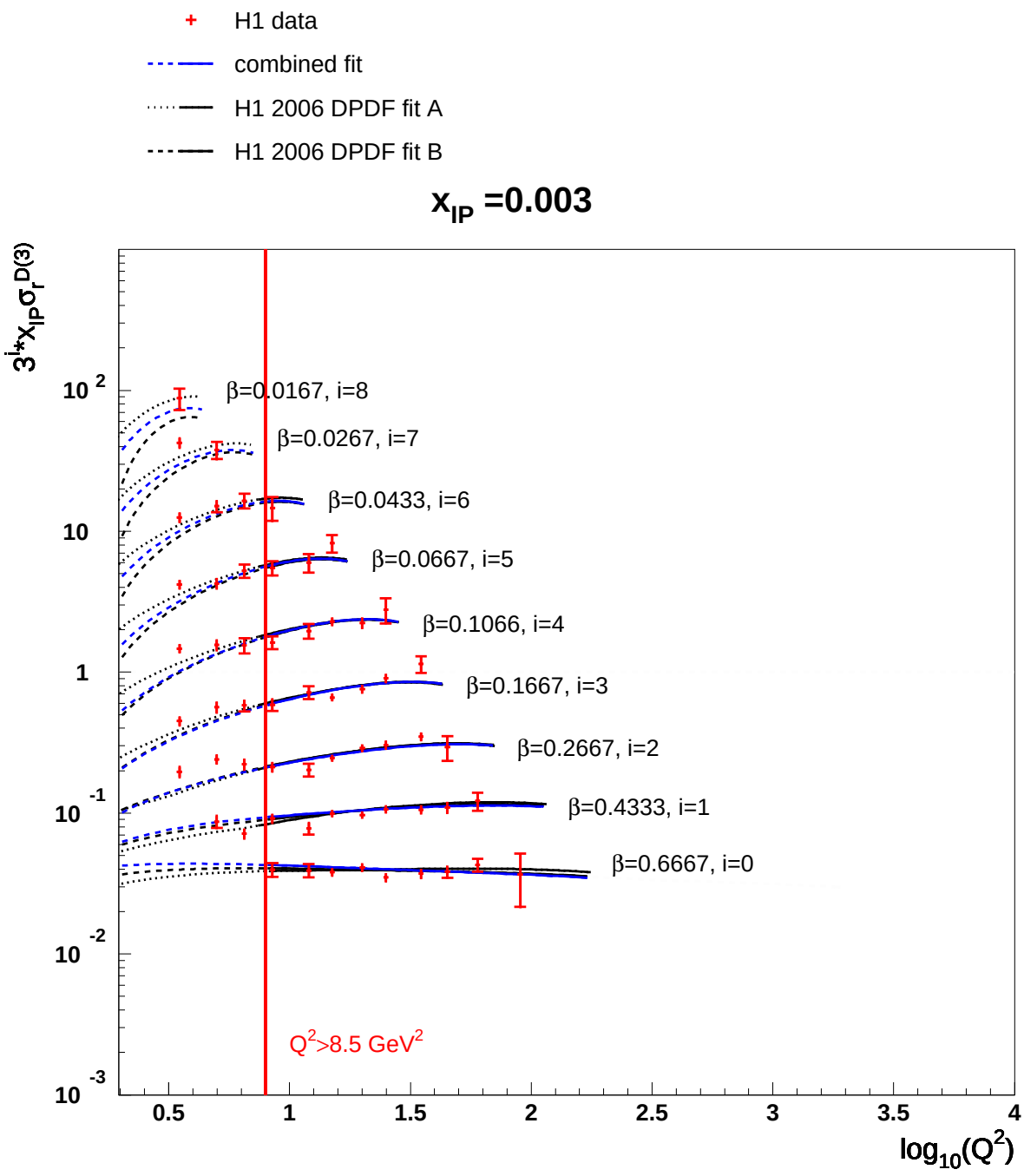

Figure 7.2: The β and Q^2 dependence of the diffractive reduced cross section $\sigma_r^{D(3)}$ multiplied by $x_{I\!P}$ at $x_{I\!P}$=0.003. See caption of figure 7.1 for further details.

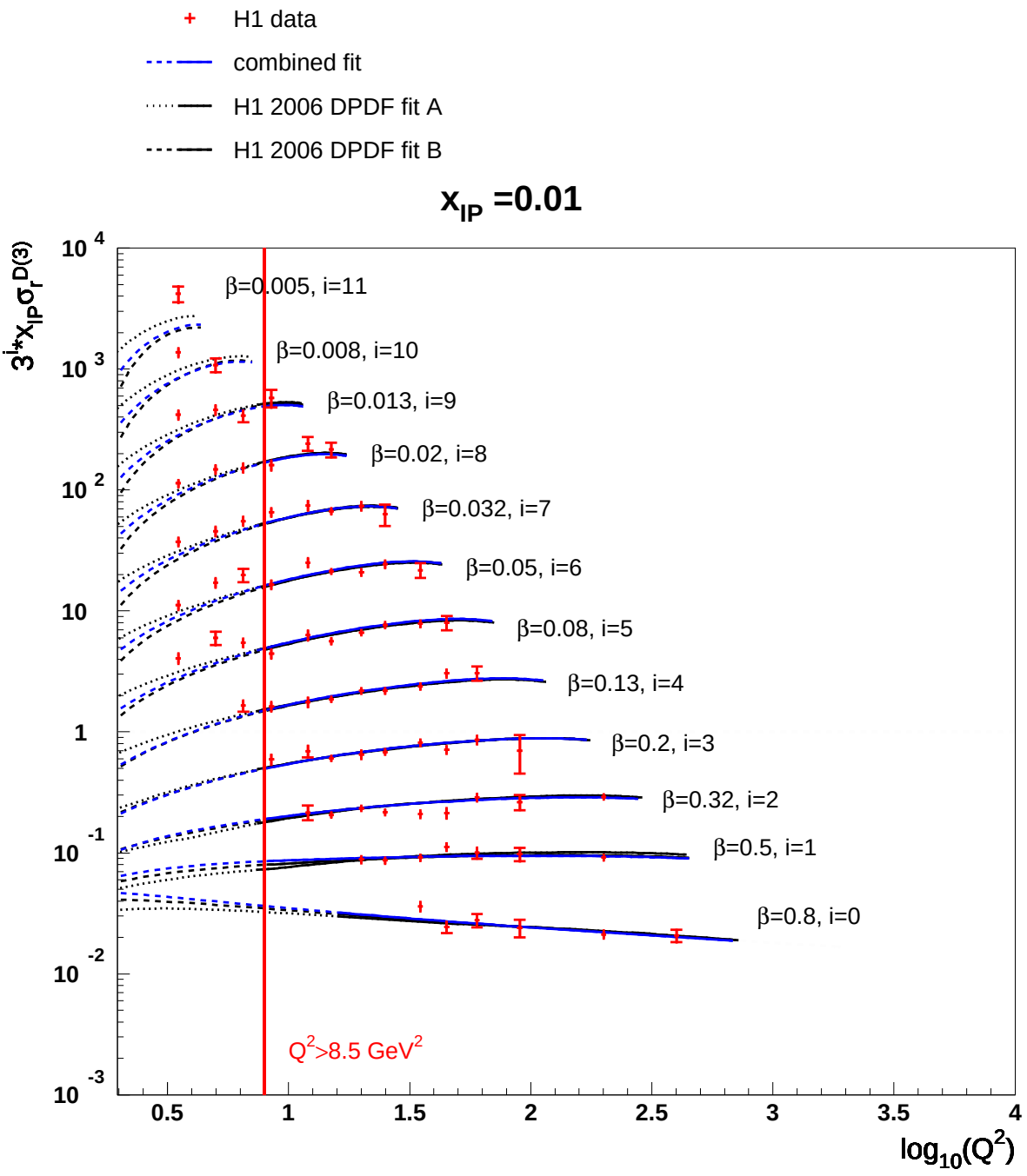

Figure 7.3: The β and Q^2 dependence of the diffractive reduced cross section $\sigma_r^{D(3)}$ multiplied by $x_{I\!P}$ at $x_{I\!P}$=0.01. See caption of figure 7.1 for further details.

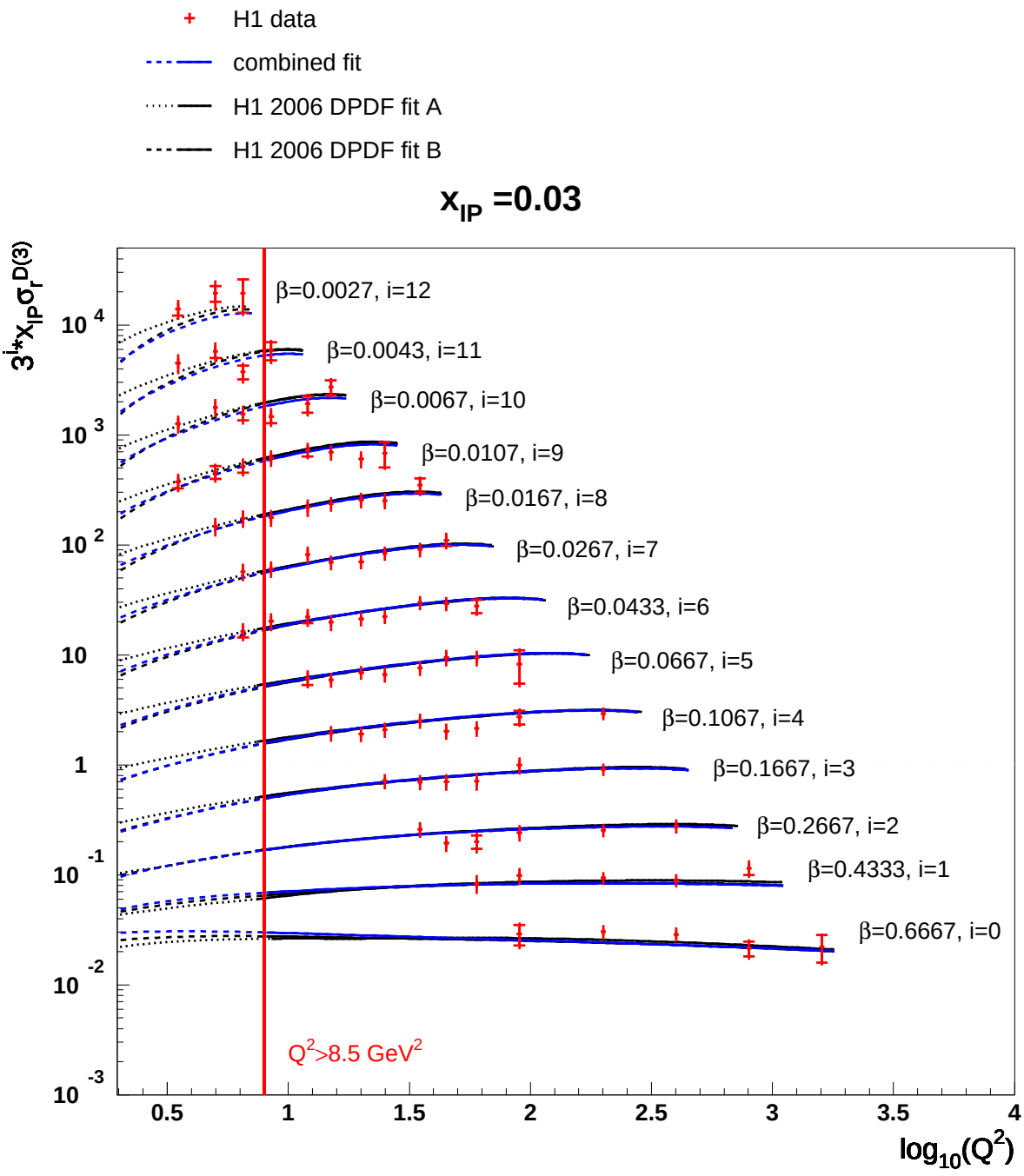

Figure 7.4: The β and Q^2 dependence of the diffractive reduced cross section $\sigma_r^{D(3)}$ multiplied by $x_{I\!P}$ at $x_{I\!P}$=0.03. See caption of figure 7.1 for further details.

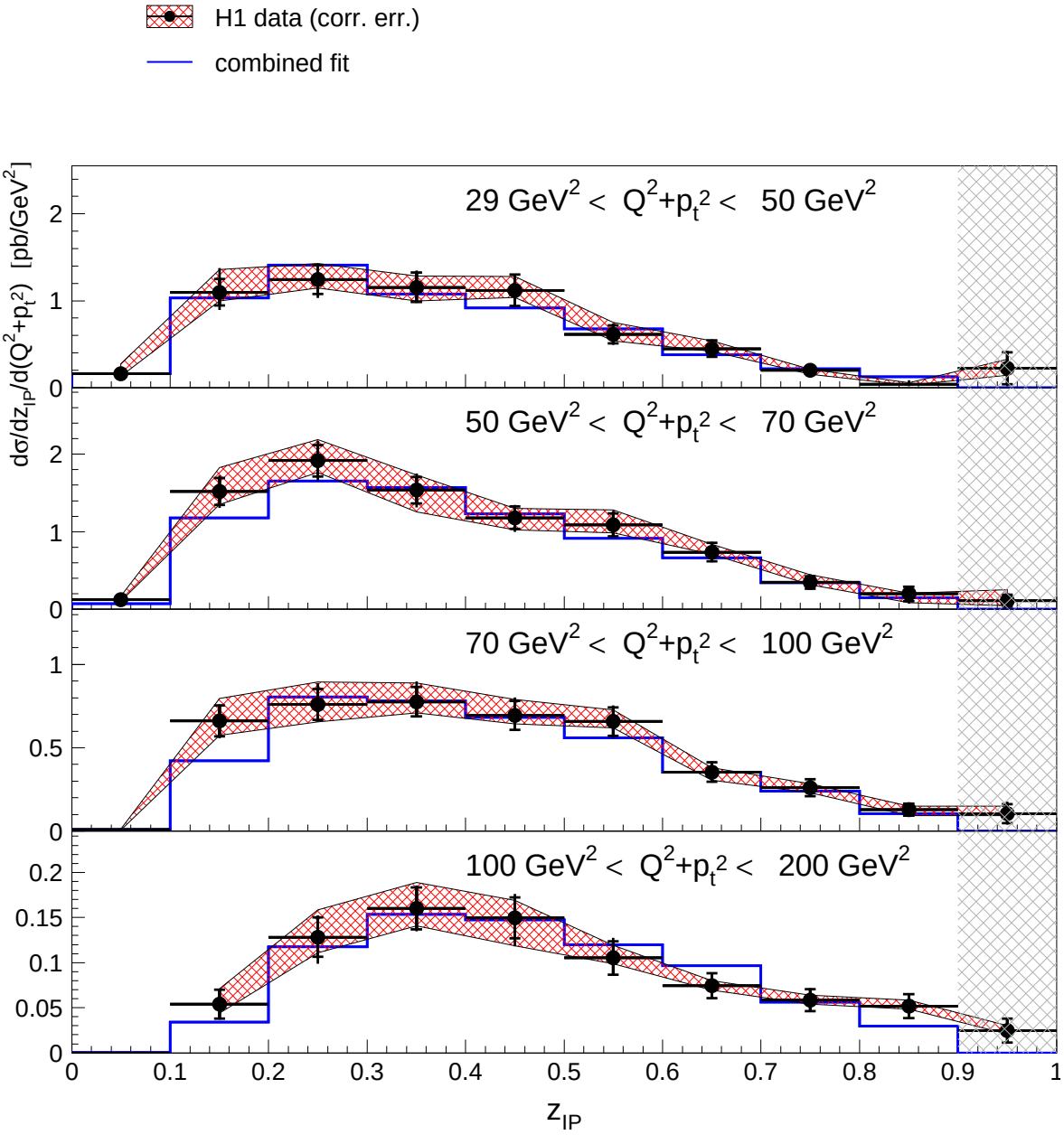

Figure 7.5: Cross section of diffractive dijets double differential in $z_{I\!P}$ and the scale $\mu^2 = Q^2 + p_\perp^{\star 2}$. The data are shown as black points with the inner and outer error-bar denoting the statistical and uncorrelated systematic uncertainties respectively. The red hatched band indicates the correlated systematic uncertainty. The blue line shows the NLO QCD prediction based on the combined fit. Data points in the grey hatched area were not included in the fit due to problems with the hadronization corrections.

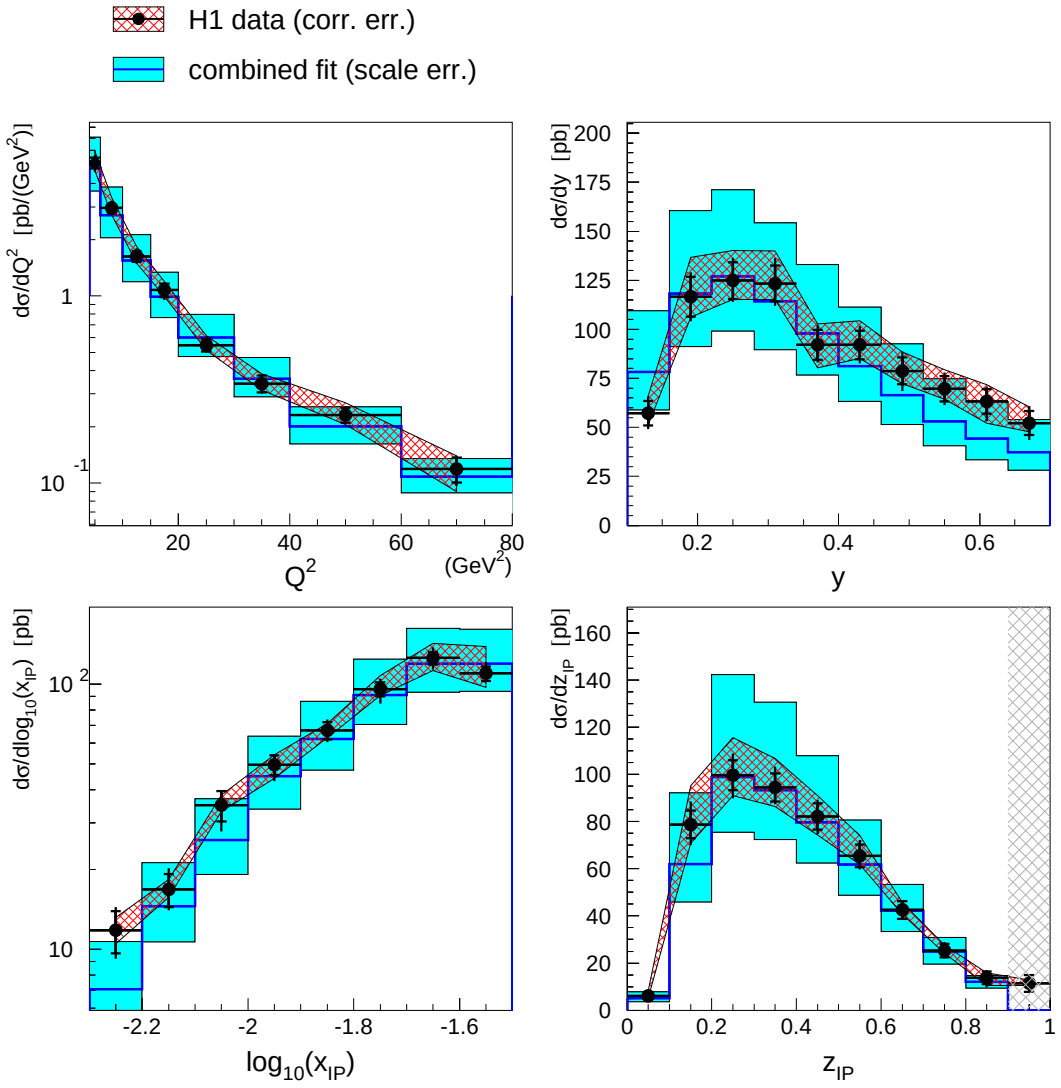

Figure 7.6: Comparison of the data (black points) to the QCD predictions based on the combined fit (blue line). The inner errorbars on the datapoints represent the statistical uncertainty, the outer errorbars also include uncorrelated systematic uncertainties added in quadrature. The red hatched band shows the correlated systematic uncertainty. The prediction for the combined fit is surrounded by a shaded band showing the scale uncertainty of the prediction (factorization- and renormalization scale $Q^2 + p_\perp^{\star 2}$ were varied by factors of 0.25 and 4. respectively). The highest bin in $z_{I\!P}$ is not compared to the prediction due to problems with the hadronization correction (see section 4.2.3).

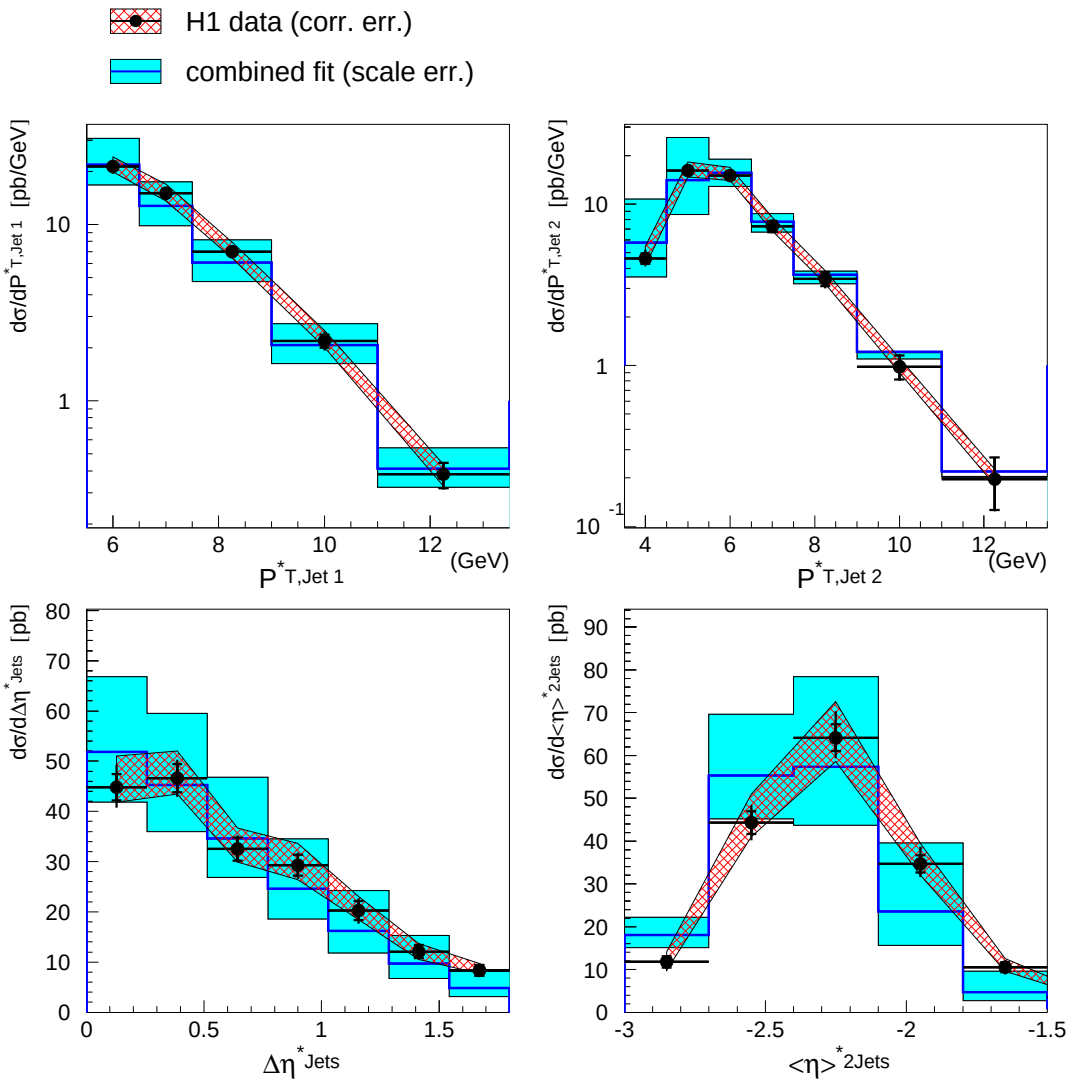

Figure 7.7: Comparison of the data (black points) to the QCD predictions based on the combined fit (blue line). The inner errorbars on the datapoints represent the statistical uncertainty, the outer errorbars also include uncorrelated systematic uncertainties added in quadrature. The red hatched band shows the correlated systematic uncertainty. The prediction for the combined fit is surrounded by a shaded band showing the scale uncertainty of the prediction (factorization- and renormalization scale $Q^2 + p_\perp^{\star 2}$ were varied by factors of 0.25 and 4. respectively).

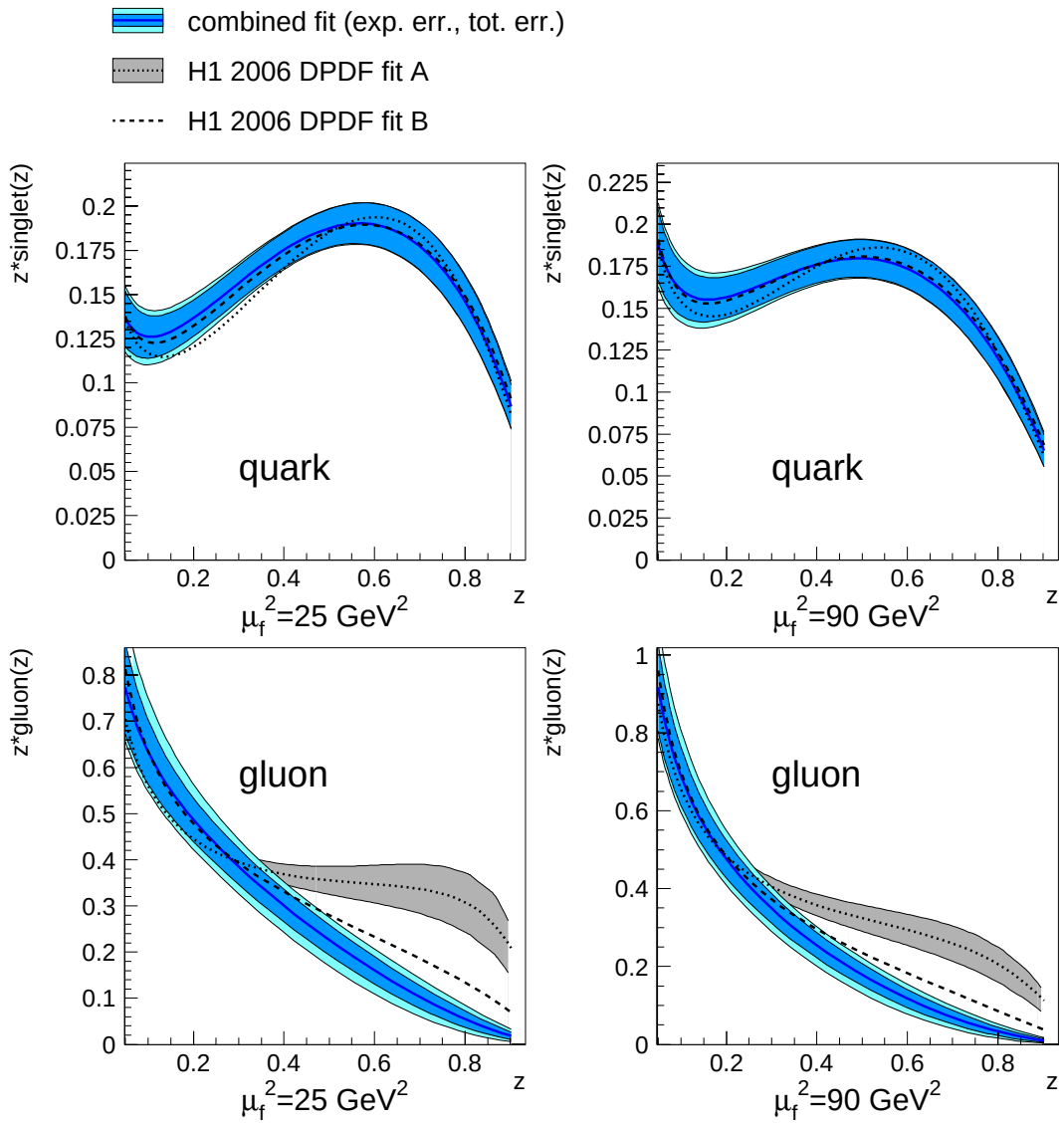

Figure 7.8: Diffractive parton densities from the combined fit. The quark and gluon densities are plotted as function of the momentum fraction z for two different factorization scales μ_f^2. The result of the combined fit is represented by the dark blue line surrounded by a blue band and a light blue band representing the experimental and total uncertainties respectively. The dotted and dashed lines denote the densities of the H1 2006 DPDF fit A and B respectively. The uncertainty of the gluon density of the H1 2006 DPDF fit A is shown as grey band.

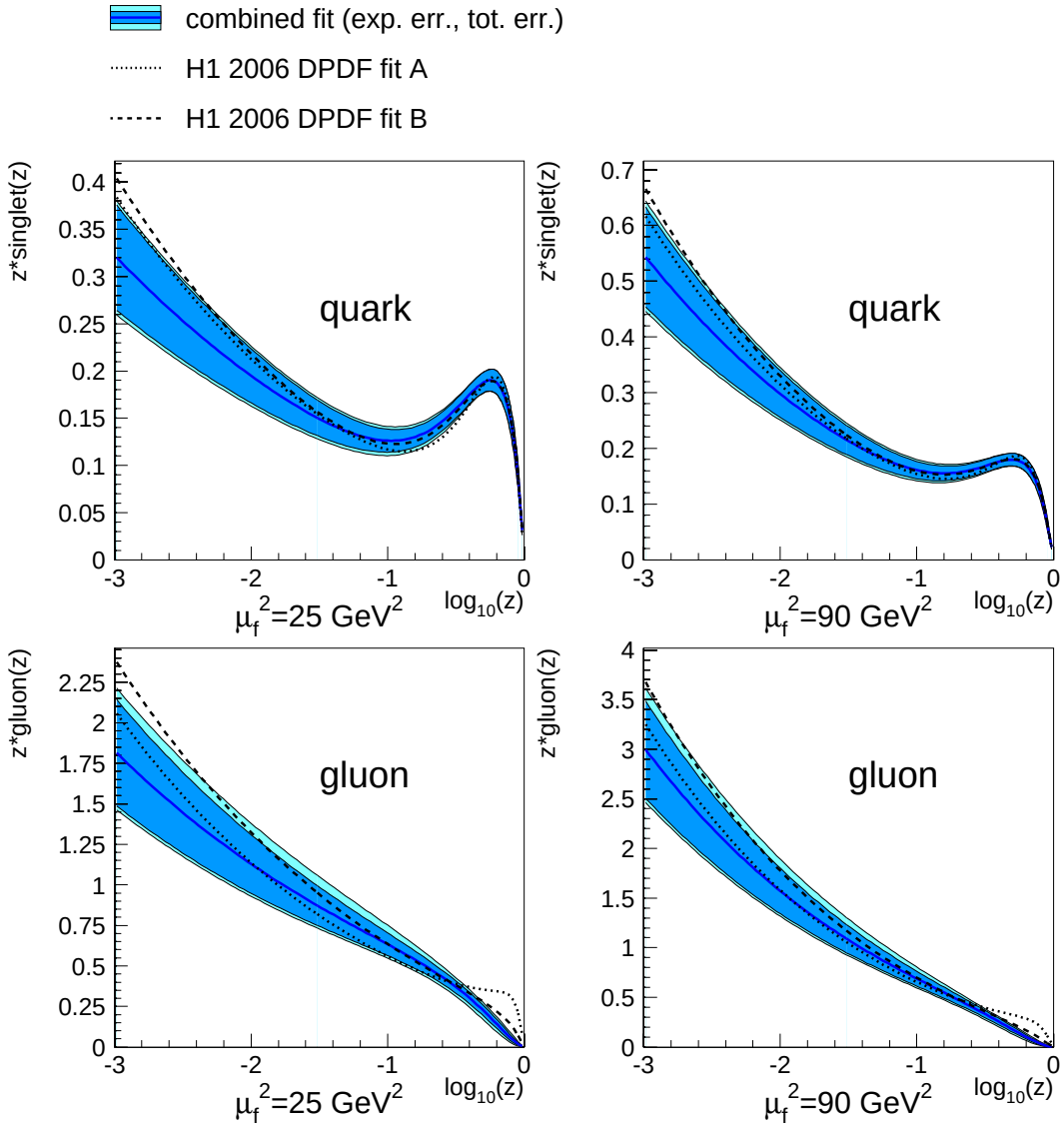

Figure 7.9: Diffractive parton densities from the combined fit. The quark and gluon densities are plotted as function of the momentum fraction $\log_{10}(z)$ for two different factorization scales μ_f^2. The result of the combined fit is represented by the dark blue line surrounded by a blue band and a light blue band representing the experimental and total uncertainties respectively. The dotted and dashed lines denote the densities of the H1 2006 DPDF fit A and B respectively.

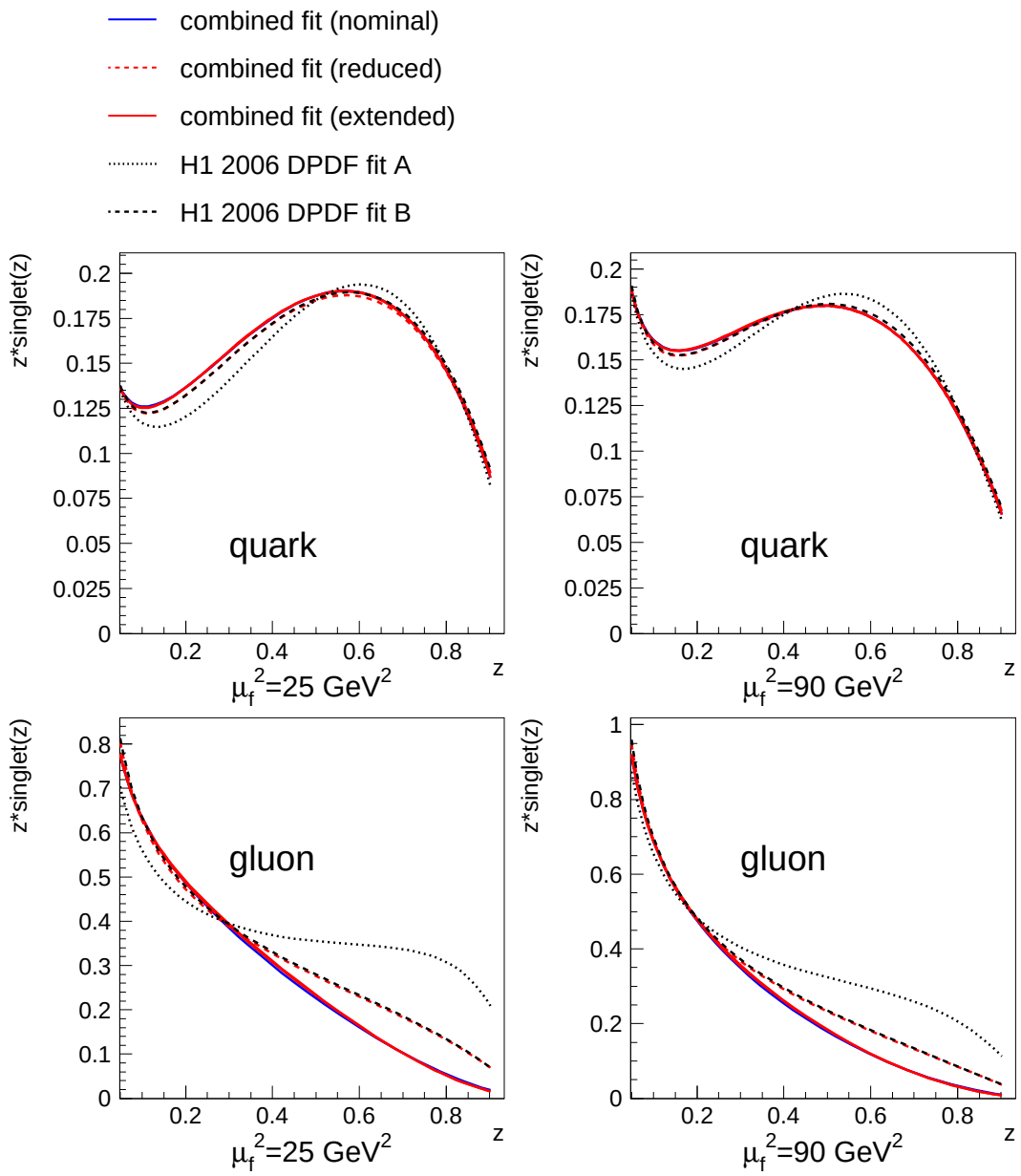

Figure 7.10: Parton densities for different initial parameterizations. The quark and gluon densities are plotted as function of the momentum fraction z for two different factorization scales μ_f^2. The result of the nominal combined fit is represented by the dark blue line. The fits with the extended parameterization of equations 7.7 and 7.8 are nearly indistinguishable and shown as one red line, which largely overlaps the nominal fit. The densities resulting from the reduced parameterization of equation 7.6 is denoted by a red dashed line. The dotted and dashed black lines indicate the densities of the H1 2006 DPDF fit A and B respectively.

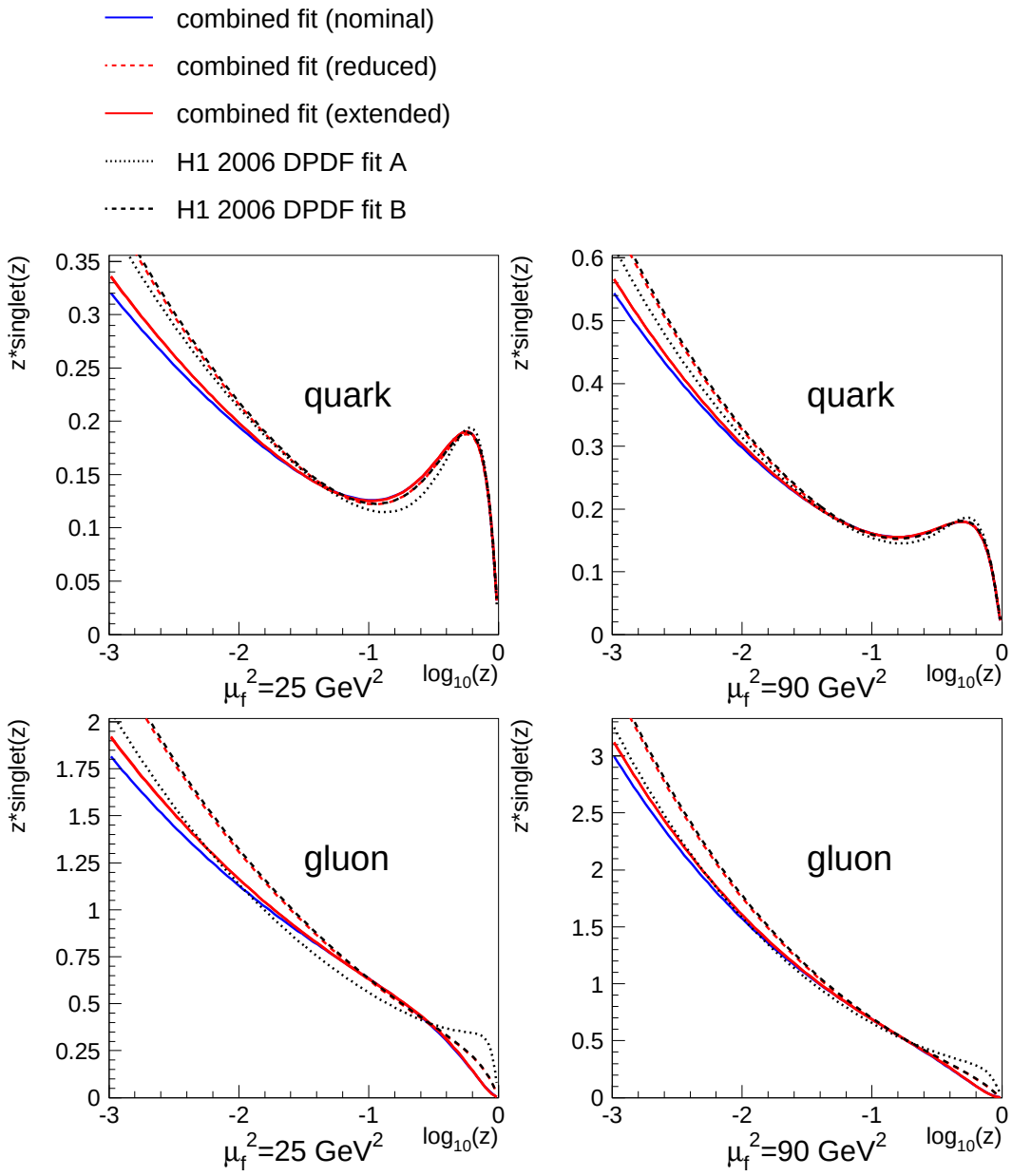

Figure 7.11: Parton densities for different initial parameterizations. The quark and gluon densities are plotted as function of the momentum fraction $\log_{10}(z)$ for two different factorization scales μ_f^2. The result of the nominal combined fit is represented by the dark blue line. The fits with the extended parameterization of equations 7.7 and 7.8 are nearly indistinguishable and shown as one red line, which largely overlaps the nominal fit. The densities resulting from the reduced parameterization of equation 7.6 is denoted by a red dashed line. The dotted and dashed black lines indicate the densities of the H1 2006 DPDF fit A and B respectively.

Chapter 8

Conclusion

In this analysis the cross section of dijet production in diffractive deep inelastic scattering was measured in the kinematic range $4\ \mathrm{GeV}^2 < Q^2 < 80\ \mathrm{GeV}^2$, $0.1 < y < 0.7$, $x_{I\!P} < 0.03$, $M_Y < 1.6$ GeV, $|t| < 1\ \mathrm{GeV}^2$, $p^\star_{\perp,jet1} > 5.5$ GeV, $p^\star_{\perp,jet2} > 4$ GeV and $-3 < \eta^\star_{jet} < 0$ at the level of stable hadrons. The resulting total dijet cross section is:

$$\sigma(ep \to e' X_{2jets} Y) = 52 \pm 1\ (\mathrm{stat.})\ ^{+7}_{-5}\ (\mathrm{syst.})\ \mathrm{pb}.$$

Due to the larger integrated luminosity and kinematic range compared to previous measurements (i.e [13]), it was possible to increase the accuracy of the measurement and produce double differential cross sections.

The measured cross sections were compared to NLO QCD predictions based on diffractive parton densities extracted from a NLO QCD fit to diffractive structure function data [12] (called H1 2006 DPDF fit A and B). The differential cross sections differ significantly from QCD predictions based on the H1 2006 DPDF fit A, but are reasonably described by ones based on the H1 2006 DPDF fit B. Although these two fits from [12] describe the F_2^D data nearly equally well, they have significantly different gluon densities at high momentum fraction z, the kinematic region most important for the dijet cross section. This large difference clearly shows the lack of sensitivity of the F_2^D data to the gluon density in this kinematic region.

The high accuracy of the dijet measurement combined with the inherent sensitivity of diffractive dijet events to the diffractive gluon density provide an ideal basis for the extraction of the gluon density with a higher accuracy than possible with an analysis of F_2^D-data alone. The best results are obtained when both data sets are combined, as the F_2^D-data is mostly sensitive to the quark density and the gluon density at low z, while the dijet cross section is dominated by the gluon contribution at high z.

The F_2^D data set from [12] was combined with the dijet data and a NLO DGLAP fit was performed to extract new and improved diffractive parton densities. The combined fit describes both data sets well, with a total χ^2/ndf of 196/217, which confirms the factorization approach of earlier analyses [7, 10, 11]. The diffractive quark density of the combined fit is very similar to the quark densities of [12], which can be expected, as the same F_2^D data set was used in both analyses. The gluon density of the combined fit, however, differs significantly from the density of the H1 2006 DPDF fit A, while it is reasonably close to the H1 2006 DPDF fit B. The gluon density derived from the

combined fit is much more stable with respect to the choice of initial parton density parameterization than the pure F_2^D fit.

The improvement of the parton densities presented in this work is most noticeable in the gluon density at high momentum fraction z. This region is of particular interest for diffractive physics at hadron colliders like the Tevatron or LHC. At these accelerators diffractive scattering involving high-z gluons play an important role for instance in the production of jets [22]. Knowledge of the diffractive gluon density will be of particular importance to estimate the multi-jet background in diffraction at the LHC, an important uncertainty in the search for the Higgs-meson in diffraction [68, 69]. Unfortunately, accurate knowledge of the diffractive parton densities is not the only obstacle for a reliable prediction of diffractive processes at hadron colliders. In particular the breakdown of QCD factorization in hadron collisions due to multiple interactions is not really understood [21, 70].

Any further improvement of the measurement of diffractive parton densities at H1 will have to rely on an improved detector in addition to a larger data sample. Already in this analysis the systematic uncertainties play an important role, and merely increasing the statistical quality of the data sample will not be enough to significantly improve the determination of the parton densities. In the dijet sample as well as the F_2^D data, a large part of the systematic uncertainty is caused by the poor understanding of the forward tagging detectors and the forward energy flow of the events. These uncertainties may be eliminated, if the rapidity gap method is abandoned and the elastically scattered proton is detected directly instead. For the HERA II data taking period special detectors (the very forward proton spectrometer) have been added to the H1 detector for exactly this purpose.

Bibliography

[1] Gross, D. J. and Wilczek, F. *Phys. Rev. Lett.* **30**, 1343–1346 (1973).

[2] Politzer, H. D. *Phys. Rev. Lett.* **30**, 1346–1349 (1973).

[3] Regge, T. *Nuovo Cim.* **14**, 951 (1959).

[4] Regge, T. *Nuovo Cim.* **18**, 947–956 (1960).

[5] Forshaw, J. R. and Ross, D. A. *Cambridge Lect. Notes Phys.* **9**, 1–248 (1997).

[6] Donnachie, S., Dosch, G., Nachtmann, O., and Landshoff, P. *Camb. Monogr. Part. Phys. Nucl. Phys. Cosmol.* **19**, 1–347 (2002).

[7] Collins, J. C. *Phys. Rev.* **D57**, 3051–3056 (1998). Erratum-ibid. D **61** (2000) 019902.

[8] Bjorken, J. D. and Paschos, E. A. *Phys. Rev.* **185**, 1975–1982 (1969).

[9] Feynman, R. P. *Phys. Rev. Lett.* **23**, 1415–1417 (1969).

[10] Ingelman, G. and Schlein, P. E. *Phys. Lett.* **B152**, 256 (1985).

[11] Donnachie, A. and Landshoff, P. V. *Phys. Lett.* **B191**, 309 (1987).

[12] H1 Collaboration. *Measurement and QCD Analysis of the Semi-Inclusive Diffractive Deep-Inelastic Scattering Cross Section at HERA*. DESY 06-049, submitted to *Eur. Phys. J.*, hep-ex/0606004.

[13] Schätzel, S. *Measurements of Dijet Cross Sections in Diffractive Photoproduction and Deep-Inelastic Scattering at HERA*. PhD thesis, Univ. Heidelberg, (2004).

[14] Adloff, C. et al. *Z. Phys.* **C76**, 613–629 (1997).

[15] Adloff, C. et al. *Eur. Phys. J.* **C20**, 29–49 (2001).

[16] Adloff, C. et al. *Phys. Lett.* **B520**, 191–203 (2001).

[17] Derrick, M. et al. *Z. Phys.* **C68**, 569–584 (1995).

[18] Chekanov, S. et al. *Nucl. Phys.* **B713**, 3–80 (2005).

[19] Chekanov, S. et al. *Nucl. Phys.* **B672**, 3–35 (2003).

[20] Chekanov, S. et al. *Eur. Phys. J.* **C38**, 43–67 (2004).

[21] Kaidalov, A. B., Khoze, V. A., Martin, A. D., and Ryskin, M. G. *Phys. Lett.* **B567**, 61–68 (2003).

[22] Affolder, A. A. et al. *Phys. Rev. Lett.* **84**, 5043–5048 (2000).

[23] Hofstadter, R. *Ann. Rev. Nucl. Part. Sci.* **7**, 231–316 (1957).

[24] Breidenbach, M. et al. *Phys. Rev. Lett.* **23**, 935–939 (1969).

[25] Eidelman, S. et al. *Phys. Lett.* **B592**, 1 (2004).

[26] Gribov, V. N. and Lipatov, L. N. *Sov. J. Nucl. Phys.* **15**, 438–450 (1972).

[27] Dokshitzer, Y. L. *Sov. Phys. JETP* **46**, 641–653 (1977).

[28] Altarelli, G. and Parisi, G. *Nucl. Phys.* **B126**, 298 (1977).

[29] Kuraev, E. A., Lipatov, L. N., and Fadin, V. S. *Sov. Phys. JETP* **45**, 199–204 (1977).

[30] Balitsky, I. I. and Lipatov, L. N. *Sov. J. Nucl. Phys.* **28**, 822–829 (1978).

[31] Sjostrand, T. *Comput. Phys. Commun.* **39**, 347–407 (1986).

[32] Sjostrand, T. and Bengtsson, M. *Comput. Phys. Commun.* **43**, 367 (1987).

[33] Webber, B. R. *Nucl. Phys.* **B238**, 492 (1984).

[34] Gribov, V. N. *JETP Lett.* **41**, 667–669 (1961).

[35] Kaidalov, A. B. and Simonov, Y. A. *Phys. Lett.* **B477**, 163–170 (2000).

[36] Owens, J. F. *Phys. Rev.* **D30**, 943 (1984).

[37] H1 Collaboration. *Measurement of Diffractive Deep-Inelastic Scattering with a leading Proton at HERA*. DESY 06-048, submitted to *Eur. Phys. J.*, hep-ex/0606003.

[38] Abt, I. et al. *Nucl. Instrum. Meth.* **A386**, 310–347 (1997).

[39] Abt, I. et al. *Nucl. Instrum. Meth.* **A386**, 348–396 (1997).

[40] Appuhn, R. D. et al. *Nucl. Instrum. Meth.* **A386**, 397–408 (1997).

[41] Bethe, H. and Heitler, W. *Proc. Roy. Soc. Lond.* **A146**, 83–112 (1934).

[42] H1 Collaboration. In *28th International Conference on High Energy Physics ICHEP'96*, (1996).

[43] Jung, H. *Comp. Phys. Commun.* **86**, 147–161 (1995).

[44] Kwiatkowski, A., Spiesberger, H., and Mohring, H. J. *Comp. Phys. Commun.* **69**, 155–172 (1992).

[45] Schuler, G. A. and Sjostrand, T. *Phys. Lett.* **B376**, 193–200 (1996).

[46] Sedlák, K. *Measurement of Dijet Production at Low Q^2 at HERA*. PhD thesis, Charles University, Prague, (2004).

[47] Lai, H. L. et al. *Eur. Phys. J.* **C12**, 375–392 (2000).

[48] List, B. and Mastroberardino, A. . Prepared for Workshop on Monte Carlo Generators for HERA Physics (Plenary Starting Meeting), Hamburg, Germany, 27-30 Apr 1998.

[49] List, B. *Diffraktive J/ψ Produktion in Elektron - Proton Stößen am Speicherring HERA*. Diplom thesis, Techn. Univ. Berlin, (1993).

[50] Nagy, Z. and Trocsanyi, Z. *Phys. Rev. Lett.* **87**, 082001 (2001).

[51] Vinokurova, S. and Wolf, R. *personal communications* .

[52] Adloff, C. et al. *Z. Phys.* **C74**, 221–236 (1997).

[53] Werner, C. *Untersuchung der Partondynamik bei kleinen Bjørken-x mit Drei-Jet-Ereignissen in tief-unelastischer $e^+ - p$-Streuung*. PhD thesis, Univ. Heidelberg, (2006).

[54] Ellis, S. D. and Soper, D. E. *Phys. Rev.* **D48**, 3160–3166 (1993).

[55] Catani, S., Dokshitzer, Y. L., Seymour, M. H., and Webber, B. R. *Nucl. Phys.* **B406**, 187–224 (1993).

[56] Huth, J. E. et al. . Presented at Summer Study on High Energy Physics, Research Directions for the Decade, Snowmass, CO, Jun 25 - Jul 13, 1990.

[57] Charchula, K., Schuler, G. A., and Spiesberger, H. *Comput. Phys. Commun.* **81**, 381–402 (1994).

[58] Schenk, S. *Energy Flow in Hard Diffractive Deep-Inelastic Scattering and Photoproduction with a Leading Proton*. Diplom thesis, Univ. Heidelberg, (2003).

[59] Thompson, P. *Open Charm Production in Inclusive and Diffractive Deep-Inelastic Scattering at HERA*. PhD thesis, Univ.Birmingham, (1999).

[60] Janssen, X. *Electroproduction diffractive de mesons Rho a HERA*. PhD thesis, Universite Libre de Bruxelles, (2003).

[61] Levonian, S. *personal communications* .

[62] Schätzel, S. *personal communications* .

[63] Botje, M., Klein, M., and Pascaud, C. *Future precision measurements of F2(x,Q**2), alpha(s)(Q**2) and xg(x,Q**2) at HERA*, (1996).

[64] James, F. and Roos, M. *Comput. Phys. Commun.* **10**, 343–367 (1975).

[65] Martin, A. D., Roberts, R. G., Stirling, W. J., and Thorne, R. S. *Eur. Phys. J.* **C28**, 455–473 (2003).

[66] Chekanov, S. et al. *Eur. Phys. J.* **C42**, 1–16 (2005).

[67] Adloff, C. et al. *Eur. Phys. J.* **C30**, 1–32 (2003).

[68] Schafer, A., Nachtmann, O., and Schopf, R. *Phys. Lett.* **B249**, 331–335 (1990).

[69] Peschanski, R. *Remarks on diffractive production of the Higgs boson*, (2005). hep-ph/0511095.

[70] Khoze, V. A., Martin, A. D., and Ryskin, M. G. *On the role of hard rescattering in exclusive diffractive Higgs production*, (2006). hep-ph/0602247.

Acknowledgments

I would like to express my gratitude to all those who supported me directly or indirectly during the past three and a half years. I enjoyed the friendly and professional atmosphere in the H1 collaboration in Hamburg as well as in the HE group in Heidelberg. First I would like to thank my advisor Franz Eisele for his guidance and support, in particular for convincing me that the combined fit would be worthwhile. My sincere gratitude also to Otto Nachtmann for acting as the second referee of this thesis. Colleagues at Hamburg I would like to mention are Frank Peter Schilling, Paul Richard Newman and Sebastian Schätzel, with whom I had many fruitful discussions. Their never ending patience in teaching me the subtleties of diffractive physics is much appreciated. I received assistance also from Olaf Behnke, who helped me greatly in improving my presentation skills. I would also like to thank Christian Pascaud for introducing me to the arcane craft of parton density fits. Last but not least, it was a pleasure to share my office at Heidelberg with Stefan, Juri, Roger, Christoph and Jens, who never failed to cheer me up with their bad jokes. I made them read this thesis in revenge.